BIOPHYSICAL BASIS OF FMRI:
INSIGHTS FROM HIGH SPATIAL RESOLUTION STUDIES OF PRIMATES

By

Na Zhang

Dissertation

Submitted to the Faculty of the

Graduate School of Vanderbilt University

in partial fulfillment of the requirements

for the degree of

DOCTOR OF PHILOSOPHY

in

Physics

December, 2007

Nashville, Tennessee

Approved:

Professor John C. Gore

Professor Malcolm J. Avison

Professor Mark D. Does

Professor Todd E. Peterson

Professor David J. Ernst

To my husband and parents

ACKNOWLEDGEMENT

This work could not have been completed without the help from various people. I thank all my committee members for their guidance and suggestion from beginning to end. Especially, to my advisors and mentors, Dr. John C. Gore and Calum Avison, I am very grateful for your support, advice and encouragement throughout my stay at Vanderbilt. I truly appreciate Limin Chen for her kind help and valuable discussions. I also want to thank Greg Turner, Anna Wang Roe, Robert Friedman, Vanessa Fitsanakis and Michael Aschner for their help and advice during the completion of this work. Thanks to all of the VUIIS people for their encouragement and friendship. I also want to acknowledge the helpful discussions and technical help from Richard Baheza, Jeffrey James Luci, Jarrod M. True, Ken Wilkens, Tuhin K. Sinha, Kevin Wilson, and Bruce W. Martin.

The research reported in this dissertation was supported by funds from the National Institutes of Health. Their support is gratefully acknowledged.

Finally, thanks are owned to my husband, my sister and my parents for their constant support and unwavering love. Enormous support also comes from my friends: Xing Zhou, Ying Hu, Yang Fu, Guozhen Luo et al. Without their support and love, I could never have succeeded.

TABLE OF CONTENTS

Page

LIST OF TABLES

Table Page

LIST OF FIGURES

CHAPTER I

INTRODUCTION

1.1 Overview

Functional magnetic resonance imaging (fMRI) has been widely used to study both human and animal brain functions (Cohen et al., 2002; Duong et al., 2000b; Kim and Ugurbil, 2003; Kwong et al., 1992; Ogawa et al., 1990). The most popular fMRI approach is Blood Oxygenation Level Dependent (BOLD) imaging as introduced in 1990 (Ogawa et al., 1990). BOLD fMRI employs hemoglobin as a convenient endogenous contrast agent. The BOLD functional map is generated based on the regional alterations to transverse relaxation rates due to regional changes in deoxy-hemoglobin that accompany changes in neuronal activity (Pauling and Coryell, 1936; Thulborn et al., 1982). This technique has been widely used to study function in a range of brain areas including visual, somatosensory and auditory cortical areas. (Kayser et al., 2004; Kim and Ugurbil, 2003; Krause et al., 2001; Kwong et al., 1992; Van Camp et al., 2006; Vanduffel et al., 2001).

To better understand brain function, one critical factor is to achieve anatomical structural and functional activation maps at millimeter and submillimeter scales. A goal of functional mapping is to resolve activity at the level of the cortical column (200-800 μm), the basic functional module. To do so requires structural and functional imaging at submillimeter scales. Such spatial resolution is commonly achieved using optical imaging methods, particularly imaging of the optical intrinsic signal (OIS), and using invasive

electrophysiology. Electrophysiological mapping, though extremely time consuming, can map receptive fields, and also directly measure the properties of a single neuron or group activities of a neuronal population, providing useful information about the underlying neuronal activity. OIS imaging has been widely used for the study of cortical function in animals including rodents, carnivores, and non-human primates (Chen et al., 2001; Chen et al., 2003; Frostig et al., 1990; Grinvald et al., 1986; Malonek and Grinvald, 1997) and, to some extent humans (Cannestra et al., 2001; Pouratian et al., 2002b; Sato et al., 2002; Schwartz, 2005). Optical imaging of intrinsic signal has high spatial resolution (50 μm) which is highly significant when imaging brain cortex (Frostig et al., 1990). However optical and electrophysiological mapping are both invasive, and are limited in their coverage by the need to expose the brain, and in the case of optical imaging, have the cortical area of interest on the exposed brain surface. These constraints limit the brain coverage, and also make longitudinal studies in the same animal considerably more complex. While based on the same hemodynamic response as OIS, fMRI techniques have the advantages that they are noninvasive, making them suitable for longitudinal studies in animals and humans and also provide whole brain coverage, allowing studies of deep cortical and subcortical areas that are inaccessible with optical methods. For these reasons, fMRI, particularly Blood Oxygenation Level Dependent (BOLD) fMRI, now plays a dominant role in both human and animal studies of brain activity and functional organization.

However, BOLD fMRI maps are based on changes in local deoxyhemoglobin concentration that arise from metabolic and hemodynamic changes that are coupled to local neural activity (Arthurs and Boniface, 2002). While the broader aspects of this

coupling have been characterized, the ultimate functional spatial specificity of the positive BOLD signal as a mapping tool is not well established. Also the extent to which the amplitude of BOLD signal changes in these activation maps correlate with changes in underlying neuronal activities, as well as their equivalence to maps obtained by optical imaging and electrophysiology, are still open questions.

To address these issues, we developed a BOLD fMRI mapping methodology to achieve high-spatial resolution in a non-human primate model, and performed parallel optical imaging and electrophysiology studies in the same animal to investigate the specificity of BOLD mapping with respect to the underlying neuronal activities.

Three factors were considered when planning these studies. First, we performed the BOLD fMRI studies at very high field (9.4T) to increase the sensitivity of the BOLD fMRI signal, allowing higher spatial resolution. Second, we used vibrotactile stimulation which is mild compared to more commonly used electrical stimulation (Ferretti et al., 2006; Krause et al., 2001; Silva et al., 1999; Suh et al., 2006; Weber et al., 2006; Yang et al., 1997), reasoning that vibrotactile stimulation will not induce muscle contraction and will generate more focal primary sensory stimuli without secondary sensory stimuli related to limb and digit movements. More importantly, vibrotactile stimuli are behaviorally relevant stimuli that activate specific, well-characterized anatomical and functional pathways in the somatosensory pathway; the representation of such stimulus parameters in primate SI, and in particular in areas 3b and 1 are relatively well understood (Chen et al., 2007). Third, we chose the non-human primate model. This model, by virtue of allowing correlated measurements of BOLD signal change and neurophysiological responses to the same stimulus, offers a unique opportunity to study

the nature of the BOLD activity and its dependence on the neuronal activity in a species whose cerebral anatomy, cortical organization and cytoarchitecture closely resemble those of humans, bridging the gap between human neuroimaging studies and the enormous body of data available from animal studies (Leite et al., 2002; Orban et al., 2003; Tsao et al., 2006). Overall this approach has proven of considerable value, and fMRI studies in non-human primates are already beginning to link local electrophysiological and broader system and cognitive neuroscience data, as well as contributing to our understanding of the biophysical basis of the fMRI signal (Denys et al., 2004; Gamlin et al., 2006; Gretton et al., 2006; Shmuel et al., 2006).

The final component of this part of the thesis research applied the fMRI methods developed to characterize the brain activities in different cortical and subcortical areas of the somatosensory cortex. We first studied the influence of the stimulus intensity on the BOLD fMRI signals in different brain regions. We also used BOLD fMRI to perform the first high resolution functional imaging studies of non-human primate secondary somatosensory cortical areas.

A second area of research described in this thesis pertains to the influence of the paramagnetic ion Mn^{2+} on the relaxation properties (T_1, T_2) of tissue water in different brain regions. This research was motivated on the one hand by recent reports that in vivo measurements of brain T_1 and/or T_2 can be used to measure regional levels of tissue Mn^{2+}, and on the other by the increasing use of so-called manganese enhanced MRI (MEMRI) as a tool for mapping neural activation based on activity dependent uptake of Mn^{2+} through Ca^{2+} uptake pathways. Both of these areas of research make untested assumptions about the quantitative dependence of T_1 and T_2 on local Mn^{2+} concentration,

and particularly that the dependence is the same in all brain regions. The goal of this component of the research was to test the validity of these assumptions.

1.2 Research objectives

In light of the introduction above, we now summarize the specific objectives of the research below:

1. Develop a general methodology for high-spatial resolution fMRI with submillimeter spatial resolution.
2. Investigate the stability and reproducibility of the developed fMRI technique.
3. Combine high-resolution fMRI with electrophysiology and optical imaging measurements in the same animal to investigate the consistency of activation maps acquired with the three techniques.
4. Investigate the influence of stimulus intensity on positive BOLD fMRI signals in the primary somatosensory cortex.
5. Characterize local negative BOLD responses and their dependence on the stimulus intensity.
6. Apply validated high resolution BOLD fMRI to probe the brain activity in previously unstudied cortical areas such as SII.
7. Probe the behavior of paramagnetic tracers in vivo and evaluate factors affecting their application in the investigation of the connectivity between different brain regions.

1.3 Organization of the dissertation

This dissertation is organized as follows: In Chapter 2, we developed a high field (9.4T) BOLD fMRI methodology and applied it to a non-human primate model with vibrotactile stimulation. We first demonstrated that positive BOLD signals mapped using this experimental protocol reveal fine fingerpad topographic maps which match/agree with maps obtained using OIS imaging in the same animal. We also show that BOLD fMRI can reliably resolve sub-millimeter spatial shifts in activations in area 3b of somatosensory cortex previously identified with OIS (Chen et al., 2007) as neural correlates of the "funneling illusion". The BOLD signals found in area 3b are robust and highly reproducible across runs, sessions and animals. These data demonstrate that at high field, high spatial resolution topographic maps can be achieved using the positive BOLD signal.

In Chapter 3, we examine the dependence of the BOLD signal response in squirrel monkey primary somatosensory cortex on stimulus intensity. We first investigate the dependence of the positive BOLD response on the intensity of vibrotactile stimulation in two subregions of SI (areas 3b and 1) previously studied using OIS and electrophysiology. These studies reveal significant differences in BOLD response between these neighboring subregions, suggesting divergent roles for these subregions in vibrotactile intensity encoding. These findings are consistent with the theory that area 3b plays a role in the earliest steps of cortical encoding of vibrotactile sensory stimuli. In the later part of this chapter, we report consistent negative BOLD responses in areas adjacent to but distinct (~3mm distant) from the areas of positive BOLD signals in area 3b. The areas of negative

BOLD signal lay in higher order sensory or sensorimotor areas, and differ from area 3b in their temporal responses and dependence on stimulus intensity.

In Chapter 4, we investigated the somatotopic organization of digits in higher order somatosensory areas. Our data reveal distinct anterior and posterior subregions adjacent to the lateral sulcus, possibly corresponding to the SII and PV regions reported in other nonhuman primate studies. We also report preliminary observations of a sensory funneling effect in both anterior and posterior SII regions. These represent the first imaging studies of SII organization, and suggest that while there is somatotopic organization in SII, it may not be as fine-grained as in SI.

In Chapters 2-4, we focused on developments and applications of BOLD fMRI methodology that can achieve high spatial resolution at submillimeter scales. In Chapter 5, we shift our focus to examine the influence of iron and manganese ion concentrations on MR signals and particularly water relaxation rates in the rat brain *in vivo*. We demonstrate that, when Mn and Fe concentrations are manipulated in a biological system, their combined influence on MRI signals, particularly T_1 and T_2, is poorly explained by the simple linear models commonly used in the MRI literature, and also make the important observation that the relaxivity of Mn^{2+} is different in different brain regions. We develop a model that predicts the interacting relationship of two paramagnetic ions and their combined influence on the tissue water relaxation. This model may be useful for interpreting MR results when more than one paramagnetic species is involved. This is the first study to report the regional variations that are apparent in the experimental data and provide an explanatory model. These studies provide a quantitative foundation for

applications of Mn that enhance contrast between adjacent brain structures and distinct cortical layers, map patterns of neural activation, and trans-synaptic tract tracing.

Finally, in Chapter 6 we draw conclusions and discuss possible future directions.

CHAPTER II

HIGH SPATIAL RESOLUTION FMRI WITH PRIMATE MODEL USING FINGER DIGITS TACTILE STIMULATION

2.1 Overview

Since its discovery in early the 90s, BOLD fMRI has become one of the most powerful mapping techniques for localizing brain function and has revolutionized cognitive neuroscience. As cortical columns are believed to be the building blocks of cerebral cortical function, revealing functional structures at the millimeter and submillimeter scale is critical to understanding brain function. Activation mapping at this millimeter- and submillimeter-scale is largely the domain of other high spatial resolution techniques such as optical imaging of intrinsic signals (OIS) and single unit electrophysiology. As higher magnetic field (B0) strengths improve the sensitivity of the fMRI signal, higher spatial and temporal resolutions can be achieved. However, the ultimate functional spatial specificity of the positive BOLD signal as a mapping tool, the extent to which these activation maps correlate with underlying neuronal activities, as well as their equivalence to maps obtained by optical imaging and electrophysiology, are still open questions.

In contrast to BOLD fMRI, OIS offers higher spatial (~50μm) and temporal resolution (~100 ms), and has been widely used for the study of cortical function in animals including rodents, carnivores, and non-human primates (Chen et al., 2001; Chen et al., 2003; Frostig et al., 1990; Grinvald et al., 1986; Malonek and Grinvald, 1997; Ts'o et al., 1990) and, to some extent in humans (Cannestra et al., 2001; Pouratian et al., 2002a;

Sato et al., 2002; Schwartz, 2005). Many studies suggest that the optical intrinsic signal corresponds to the early negative BOLD signal (the so-called 'initial dip') (Cannestra et al., 2001; Malonek and Grinvald, 1997; Pouratian et al., 2002b; Sheth et al., 2003; Thompson et al., 2003; Toth et al., 1996). This early negative BOLD signal is quite small however, and not reliably detected (Cannestra et al., 2001; Duong et al., 2000a). Although alternative fMRI approaches, such as cerebral blood flow (CBF) and volume (CBV) methods, can reveal sub-millimeter size columnar and laminar organizations of cortex (Duong et al., 2000a, , 2001; Harel et al., 2006a; Lu et al., 2004; Pouratian et al., 2002b; Sheth et al., 2003; Vanzetta et al., 2004) and retina (Cheng et al., 2006), whether such spatial resolution can be obtained with positive BOLD signal is unknown.

To address these issues, we compared the positive BOLD and OIS maps of fingerpad representation in SI in the same anesthetized squirrel monkey. In addition to validating the BOLD maps, such intra-individual comparisons can provide direct linkage between OIS and electrophysiological signals studied in animals and BOLD signals studied in humans. Chen et al. have previously used OIS to map the somatotopy of millimeter-sized fingerpad representations in areas 3b and 1 of SI in this species (Chen et al., 2001), and identified a sub-millimeter spatial shift in activation location corresponding to the neural correlate of the tactile funneling illusion (Chen et al., 2003). Here, we test whether BOLD fMRI can also achieve sub-millimeter spatial resolution. The stability of the positive BOLD signal has also been investigated.

2.2 Experimental protocol

2.2.1 Animal preparation

Squirrel monkeys were anesthetized with ketamine hydrochloride (10mg/kg)/atropine (0.05mg/kg) and maintained with isoflurane anesthesia (0.8-1.1%) delivered in a 70:30 O_2:NO_2 mixture. Animals were intubated and artificially ventilated. After intubation, the animal was placed in a custom-designed MR cradle and its head secured with ear bars and an eye bar. Lactated ringers solution was infused intravenously (2-3ml/hr/kg) to prevent dehydration during the course of the study. SpO2 and heart rate (Nonin, Plymouth, MN), ECG, ET-CO2 (22-26 mmHg; Surgivet, Waukesha, WI), and respiration rate (SA instruments, Stony Brook, NY) were externally monitored and maintained. Temperature (37.5 - 38.5 ˚C) was monitored (SA instruments) and maintained via a combination of a circulating water blanket (Gaymar Industries, Orchard Park, NY) and a flow of warm air (SA instruments). Real time monitoring was maintained from the time of induction of anesthesia until full recovery. All procedures were in compliance with and approved by the Institutional Animal Care and Use Committee of Vanderbilt University.

2.2.2 Stimulus protocol

The fingers were secured by gluing small pegs to the fingernails and fixing these pegs firmly in plasticine, leaving the glabrous surfaces available for vibrotactile stimulation by a rounded plastic probe (2mm diameter) connected to a piezoelectric device (Noliac, Kvistgaard, Denmark). Piezos were driven by Grass S48 square wave stimulators (Grass-Telefactor, West Warwick, RI) at a rate of 8 Hz with 30 ms pulse

duration. Stimulation was applied in blocks of 30s on then 30s off. The timing of the presentation of stimuli was externally controlled by the MR scanner.

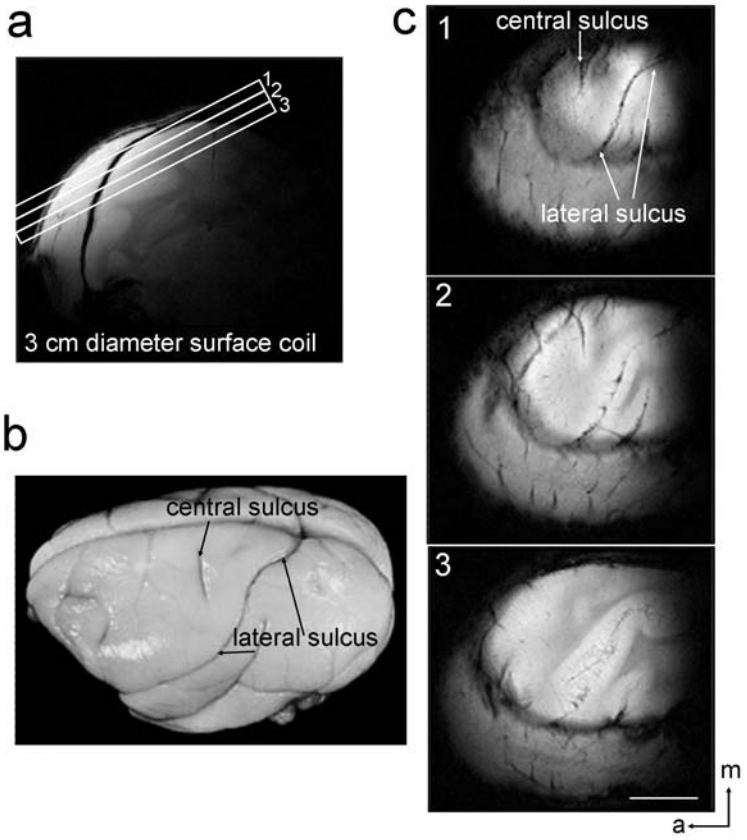

Figure 1 Anatomic images for studying SI. a: A high resolution coronal image is collected to locate somatosensory cortices, and to guide placement of 3 oblique slices parallel to SI cortex (locations indicated by red rectangles, overlaid on coronal scout image). This oblique orientation was used for both high-resolution anatomical and functional imaging. b: Major landmarks (such as central and lateral sulci) used to identify SI are visible on squirrel monkey brain tissue. c: In three images acquired with T2* weighting, sulci and vascular structures appear dark. Both central sulcus and lateral sulcus are indicated in the most superficial slice. Scale bar: 10 mm.

2.2.3 MR methods

All scans were performed on a 9.4T 21-cm narrow-bore Varian Inova magnet (Varian Medical Systems, Palo Alto, CA), using a high-performance 3–cm surface transmit-receive coil secured over the sensory cortex. Scout images using a fast gradient-echo sequence were used to define a volume covering primary somatosensory cortex in which static magnetic field homogeneity was optimized, and to plan oblique slices, for structural and functional imaging (Figure 1). T_2*-weighted gradient–echo structural images (TR=200 ms, TE=14 ms, 3 slices, 512X512 matrix, 78X78X2000 μm resolution, NEX=4) were acquired to identify venous structure on the cortical surface used to help locate SI cortex, and as structural features for coregistration of fMRI and optical somatotopic maps. fMRI data were acquired from the same slice using a Gradient Echo Planar (GE-EPI) sequence (TR=1.5s, TE=16, 64X64 matrix, 625X625X2000 μm resolution).

2.2.4 FMRI data analysis

Images were reconstructed on the MR console (Varian Vnmrj) and imported into Matlab (Mathworks, Natick, MA) for analysis. EPI data were collected as a 64x64 matrix for an in-plane voxel dimension of 625 μm. These raw EPI images were interpolated to a 512x512 matrix for overlay on anatomic images. Time-courses were drift corrected using a linear model fitted to each time course and temporally smoothed with a low-pass filter whose cut-off frequency was set above the sixth harmonic of the task function. The correlation of each functional time-course to a reference waveform was calculated and functional maps were generated. Prior to choice of this threshold, the influence of the

threshold on the area, amplitude and center of activation were examined and compared with the results from optical imaging and electrophysiology in the same animals. Activations were overlaid on corresponding anatomic images and then compared to known topography.

2.2.5 Calculations of merging index (MI)

The merging index reflects the normalized distance of the merged activation observed during simultaneous stimulation of two digits from the center of the two single-digit activations. To calculate the MI, the digit locations are set to 0 (center of one digit), 0.5 (central point between two digits) and 1 (center of adjacent digit), allowing the center of activation for the two-digit stimulation to be normalized to the same scale across cases (Chen et al., 2003).

2.2.6 Optical imaging and data analysis

Three fMRI monkeys were subsequently imaged with optical imaging. For the optical imaging experiments, procedures identical to those used in the fMRI studies in anesthesia and vital sign monitoring were followed except monkeys were anesthetized with slightly higher isoflurane (0.9-1.3%) delivered by pure oxygen (to be consistent with previous optical studies). Importantly, ET-CO2 was maintained at the same level for all optical imaging and fMRI experiments. After craniotomy/durotomy, primary somatosenory cortex (areas 3b and 1 in SI) was exposed and identified by blood vessel landmarks revealed by fMRI studies. Images were collected using the Imager 3001 systems (Optical Imaging Inc., Germantown, NY) with 630 nm illumination. A blood

vessel map, used for landmark purposes, was collected with 570 nm illumination. In blocks of trials, stimuli (4 seconds duration) were presented in a randomly interleaved manner. 30 trials were collected per stimulus condition. Intrinsic signal maps were collected at 5 image frames per sec for 3 sec starting 200 ms prior to stimulus onset. Inter-stimulus intervals were 8 sec. Detailed optical imaging procedures have been described previously (Chen et al., 2001; Chen et al., 2003)

For each stimulus condition, all trials were summed to maximize signal-to-noise ratio. Single condition activation maps were obtained by subtracting individual frames from either the first frame image (baseline image prior to stimulus onset) obtained from each given vibrotactile stimulus or frames collected during the no stimulus condition. For each image, regions of strongest activation were delineated by using a thresholding procedure or using statistical measurement (t-test). In the thresholding procedure, the strongest activation in each single condition map was identified by clipping pixels whose gray-scale pixel values (0-255 range) were above 85% of the total pixel distribution within each image. In the statistical t-test procedure, signal amplitude (average 1.5 - 3 sec after stimulus onset) was compared to the signal 200 ms before stimulus onset.

2.2.7 Alignment of BOLD and OIS activation maps

For image registration, we identified corresponding anatomical and blood vessel landmarks in each image; these coordinates were then put into a point-based registration algorithm (implemented in MATLAB). These landmarks were selected without *a priori* knowledge of the location of functional activations. For each pair of OIS/fMRI images, the registration transformation between these two sets of coordinates was then applied to

one activation image, thereby co-registering the OIS image to the fMRI image (Chen et al., 2002; Hill et al., 1991). The resulting overlaps of activation zones in the image pairs were then examined.

To quantitatively compare the locations of BOLD and OIS activations, we generated, for each digit, 3D mesh graphs of fMRI and OIS activations. We then determined the X-Y coordinate of the activation center and calculated the distance between center locations in BOLD and OIS maps.

2.2.8 Electrophysiology

A brief electrophysiological mapping procedure, guided by the previously acquired fMRI map, was used to locate the fingerpad region of areas 3b and 1 prior to optical imaging. Tungsten microelectrodes were inserted into superficial cortical layers. The responsive skin area of the unit activity was identified by initially palpating areas on the contralateral arm and hand while listening to the audio amplifier for spike activity. Then if the unit activity was located on the hand, the skin was lightly tapped with a 2 mm diameter probe or stroked with a cotton wisp. Area 3b units were discriminated on the basis of small receptive field size (restricted to a single fingerpad), brisk responsiveness to light tapping, and a lateral to medial topography of digits D1-D5. Area 1 units typically have larger receptive fields covering more than 1 finger (Sur et al., 1982). Area 3b was found anterior to the central sulcus. Cortical representations of the distal fingerpads in area 3b and area 1 were segregated by the representations of the middle phalanges and palm (Sur et al., 1982). The receptive fields of multiple or single

units were outlined through a series of indentations with a 2 mm diameter hand-held probe.

2.3 Experimental Results

2.3.1 Spatial specificity of the positive BOLD signals in SI of primate cortex

These studies used a total of 8 hemispheres in 8 squirrel monkeys. Although we have imaged 8 squirrel monkeys using fMRI, maps from one monkey contained blood vessel noise contamination that limited our ability to perform quantitative analysis on that case; we have therefore excluded that case from subsequent quantification.

2.3.1.1 Fine fingerpad topography revealed by positive BOLD in areas 3b and 1

Eight squirrel monkeys were studied with fMRI. In each hemisphere of each squirrel monkey, we first obtained three oblique anatomical slices using a 3 cm transmit-receive surface coil positioned over somatosensory cortex (Figure 1a). This arrangement provided relatively uniform sensitivity (or higher signal/noise ratio) in a mapping plane similar to that obtained with OIS, permitting direct coregistration of fMRI and OIS maps. Clear landmarks that are available in the squirrel monkey brain, such as the central sulcus and lateral sulcus (Figure 1b), can be seen in the top slice (Figure 1c, Slice 1). Deeper slices (Figure 1c, Slice 2 and 3) can be used to study areas that are buried within sulci such as SII.

Figure 2 shows single condition activation maps collected from SI during individual 8 Hz vibrotactile stimulation of digit D2, D3 and D4 in monkey 1(Figure 2a-c) and D1 and D2 in monkey 2 (Figure 2f-g). We typically observed activation in area 3b

(Figure 2d and h) with weaker activation in area 1. In monkey 1, the stimulus elicited distinct focal activations in area 3b for each of the digits (Figure 2a-c). Consistent with previous optical imaging and electrophysiological studies, the centers of the adjacent digit activations were separated by ~1 mm. For digit D4 (Figure 2a), a smaller activation was observed at a more posterior location corresponding to area 1 (Figure 2d). In monkey 2, individual stimulation of D1 and D2 produced robust, focal, and somatotopically organized activations in area 3b (Figure 2f-g and see composite in Figure 2h). Consistent with previous maps in the squirrel monkey revealed by electrophysiology (Sur et al., 1982), and by optical imaging (Chen et al., 2001), these somatotopic organizations are similar across 7 monkeys. Interdigit activation distances support this similarity: the average peak distances between digits 2 and 3 (n = 4), digits 3 and 4 (n = 8), and digits 2 and 4 (n = 5) are 1.25, 1.07 and 2.04 mm, respectively. Thus, the average adjacent inter-digit distance between non-adjacent digits is roughly 2 times the average distance between adjacent digits.

A concern with fMRI image analysis is that the choice of statistical threshold may influence which voxels are considered activated and the subsequent interpretation of activation patterns. To address this issue, we compared the spatial extent of significant BOLD signal change for activation maps generated at three different statistical threshold levels: $p<10^{-5}$, $p<5x10^{-5}$, and $p< 10^{-4}$ (not corrected for multiple comparisons). As shown in Figure 3, lower thresholds resulted in slightly larger activation regions (compare Figure 3a-c and Figure 3e-g). In the two examples shown, activation areas increased up to ~2.5 times over these three threshold levels (Figure 3i). Importantly however, these activations remained centered at the same topographic locations, did not recruit additional

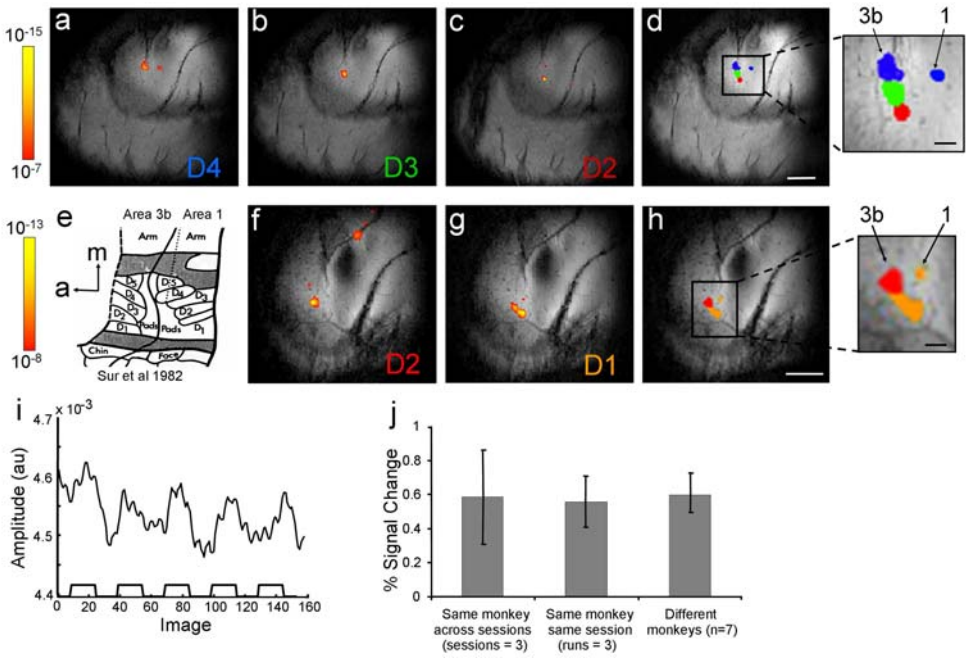

Figure 2 fMRI of digit topography in two monkeys. Single condition activation maps of vibrotactile stimulation of D4 (a), D3 (b) and D2 (c) in monkey 1, and D2 (f) and D1 (g) in monkey 2. The significance levels of the activation-associated changes in BOLD signal in a-c and f-g are indicated by their respective color bars and corresponding P value ranges. Focal activation is observed in area 3b in all 5 images, and area 1 activation is also apparent in a and g. Composite maps of a-c in monkey 1 and f-g in monkey 2 are shown in d and h (different colors represent different digit activations: D4-blue; D3-green; D2-red; D1-orange. Scale bar: 5mm). Two inserts show the enlarged view of the composite fingerpad maps (scale bar: 1 mm). Fingerpad topography in area 3b closely matches the known somatotopic map of squirrel monkey area 3b and area 1(e, from (Sur et al., 1982). The raw signal timecourse (signal amplitude in scanner arbitrary units) for a single run using block design (five cycles of 20 frames stimulus / 20 frames baseline, corresponding to five 30 sec blocks of stimulus and baseline) from D4 activation in area 3b (a) is shown in i. The mean percentage signal changes (± standard deviation) (j) were highly reproducible and stable across 3 different sessions (days) in the same monkey (left), across 3 runs within the same session (same day) in one monkey (middle), and across 7 different monkeys (right). a: anterior. m: medial.

regions, and retained topographic organization (see overlays in Figure 3d and h). This demonstrates that, for the p values examined the findings we report here are not dependent on the specific activation thresholds chosen. These findings, taken together

with the consistency of the signal timecourse and topographic organization, strongly support the conclusion that these fMRI signals are stimulus related and not artifactual.

2.3.1.2 BOLD reveals the representation of funneling illusory stimuli in area 3b

To further investigate the limits of spatial resolution, we next investigated whether high field BOLD fMRI could resolve the sub-millimeter activation shifts in area 3b previously identified as neural correlates of the tactile funneling illusion (Chen et al., 2003). In the funneling illusion, simultaneous vibrotactile stimulation of two points on the skin produces the tactile illusory sensation of a central stimulated point (at a location where no actual stimulus is delivered); psychophysically, this "funneled" sensation is stronger in magnitude than the sensation produced by either single point stimulus alone (Gardner and Spencer, 1972; Gardner and Tast, 1981; Hashimoto et al., 1999). A neural correlate of this spatially mis-localized illusory percept was identified by optical imaging in area 3b in response to simultaneous stimulation of adjacent pairs of digit tips. Specifically, this stimulus condition elicited a sub-millimeter shift in activation to a central merged (funneled) location between adjacent digit tips (Chen et al., 2003). The next series of fMRI experiments examined whether this sub-millimeter activation shift could be mapped by high field BOLD fMRI.

Figure 4 summarizes the results of fMRI mapping of SI under conditions of single and paired digit stimulation. Two cases are shown (Case 1 and Case 2). Individual stimulation of D3 and D4 generated distinct activations (Figure 4a and e, respectively). Zooming in on area 3b (bounded by turquoise rectangle in (Figure 4b, d and f) revealed well resolved activation foci separated by ~1mm. Simultaneous stimulation of D3 and D4 produced a single, focal activation, midway between the activation centers generated by

stimulation of D3 and D4 alone (Figure 4d, for comparison centers of activation locations are indicated by dotted red vertical lines). Similar results were obtained in all 5 hemispheres tested with funneling stimuli (a third funneling example with D1 and D2 stimulation is shown in Figure 5a). Consistent with optical imaging studies and with psychophysics (Chen et al., 2003; Gardner and Tast, 1981; Hashimoto et al., 1999), stimulation of non-adjacent digits showed no merging (e.g. in D2+D4 stimulus condition, Figure 5d; cf. Fig. 1 in (Chen et al., 2003)).

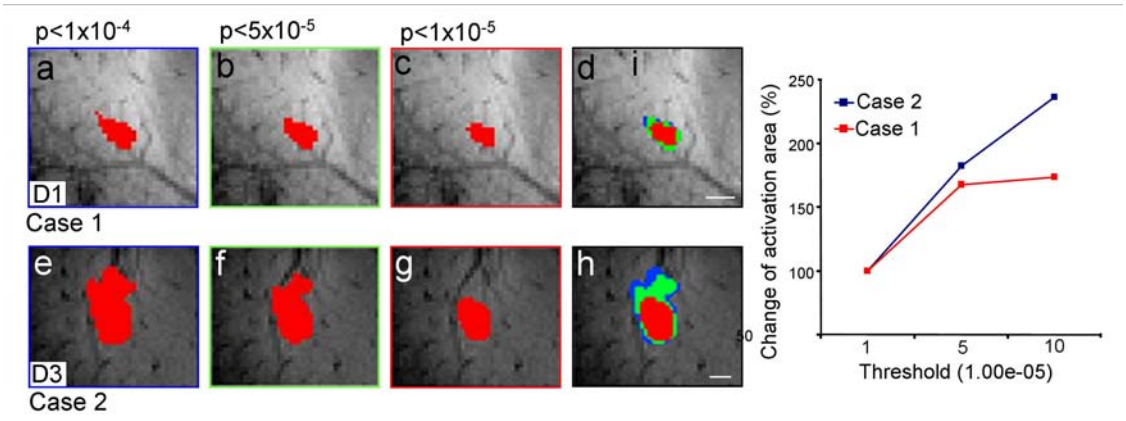

Figure 3 Effect of different image thresholds on the location and size of BOLD fMRI activation. Area of D1 activation in Case 1 (a-c) and D3 activation in Case 2 (e-g) decrease with increasing stringency of thresholding ($p<10^{-4}$, $p<5x10^{-5}$, and $p<10^{-5}$), but composite overlays (d, h) confirm that essential topography and the centroid of activation are unchanged. Activation area increases with increasing p value threshold for D1 in Case 1, and D3 in Case 2 (panel i - area relative to area at $p<10^{-5}$, defined as 100%). Compared with the activation areas at $p<10^{-5}$, areas measured at $p< 5x10^{-5}$ increased 67.5% for D1 and 81.7% for D3; areas measured at $p<10^{-4}$ sizes increased 73.5% for D1 and 135.9% for D3. Scale bars: 1mm.

To quantify the spatial shift in activation, we used a Merging Index (MI) ranging from 0 (center of one digit location) to 1 (center of second digit location) (see methods).

The MI for the case shown in Figure 4a-f is 0.53; indicating activation was located between D3 and D4. The average MI for all cases of adjacent digits was 0.55 ± 0.1(mean ± s.e.m.), in excellent agreement with the MI of 0.54±0.13 measured in previous optical imaging studies (Chen et al., 2003). This demonstrates that, without additional contrast agents, high field fMRI can resolve sub-millimeter shifts in activation.

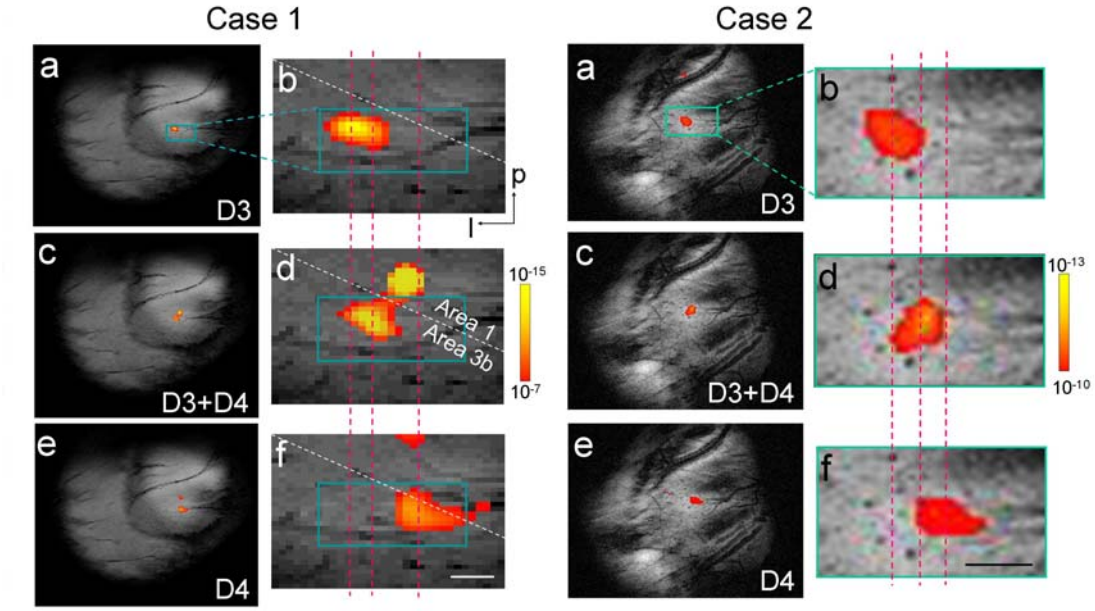

Figure 4 fMRI reveals the representation of funneling illusory stimuli in area 3b. Two cases are shown (Case 1: left, Case 2: right). For each case, stimulation of single digits D3 (a and b) and D4 (e and f) generated single focal activations organized somatotopically in area 3b (a, e within blue outline in a, shown expanded in b, f). Stimulation of paired adjacent digits (D3+D4) generated a single focal activation in area 3b (c and d), located between the sites of activation during stimulation of D3 (b) and D4 alone (f) with MI=0.53 (corresponding activation centers indicated by red dashed lines). Activation is also evident in area 1 (c and d) during simultaneous stimulation of D3+D4 in this case. Color scale from red to yellow ($p<10^{-7}$ to $p<10^{-15}$ for Case 1, $p<10^{-10}$ to 10^{-13} for Case 2; see respective color bar scales) in each activation map indicates the significance level. Scale bar: 1mm. p: posterior. l: lateral.

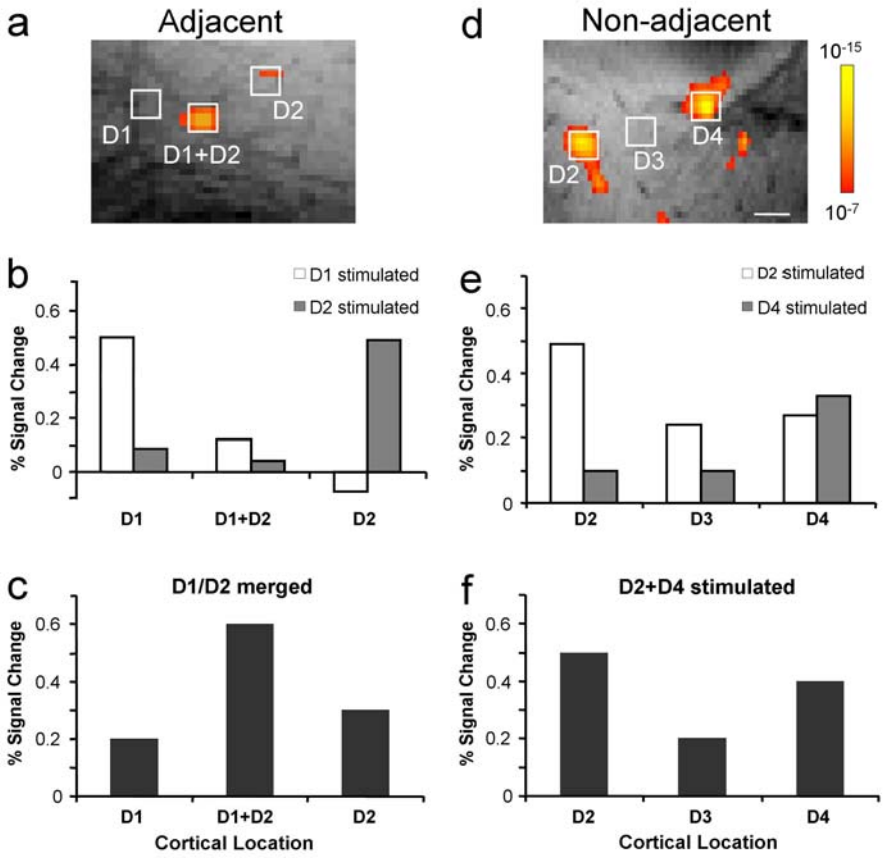

Figure 5 Comparison of amplitudes of regional fMRI signal change during single and simultaneous stimulation of adjacent (a-c) and non-adjacent (d-f) digits. Spatially shifted (centered) activation was observed in area 3b (a) during simultaneous stimulation of adjacent digits (D1+D2) while two separate activations are obtained at each site (D2 and D4) during simultaneous stimulation of non-adjacent digits (D2+D4) (d). Quantitative analysis of the percentage signal change at sites corresponding to individual activation of D1 alone, D2 alone, and D1+D2 (a), or D2 alone, D4 alone, and D2 + D4 (d) are shown in b and c (adjacent digit pair) and e and f (non-adjacent pair), respectively. The strongest % BOLD signal changes were obtained at D1 or D2 activation sites during individual stimulation of adjacent D1 (b, white columns) or D2 (b, dark columns), and at D2 or D4 activation sites during individual stimulation of nonadjacent D2 (e, white columns) or D4 (e, dark columns). In contrast, the strongest % BOLD signal change (middle black column in c) is observed at the midway location (regions analyzed shown as white boxes in a and d) during simultaneous stimulation of adjacent digits D1+D2 while comparable % signal changes (e and f) were obtained at D2 and D4 locations (d) during simultaneous stimulation of non-adjacent digits D2+D4. Color scale from red to yellow in each activation map indicates the significance level from $p=10^{-7}$ to 10^{-15} in both a and d. Scale bar: 1mm.

2.3.2 Correlation of fMRI, OIS and electrophysiology

Three monkeys were imaged with OIS.

2.3.2.1 Intra-individual optical imaging of fine fingerpad topography

In three of the animals (three hemispheres) studied by fMRI, we also examined digit topography with optical imaging. We first mapped the region near the central sulcus electrophysiologically to determine the locations of digit representation within areas 3b and 1 (color dots in Figure 6d and g). Optical images were then acquired from this region during stimulation of distal fingerpads with stimuli identical to those used for the fMRI sessions (for details see methods). Optical images obtained in response to D4, D3, and D2 stimulation revealed activations in both areas 3b and 1 (Figure 6a-c and e-f, respectively). Consistent with previous optical imaging studies, digit activations are ~ 1 mm^2 in size in area 3b and somewhat smaller in area 1. D2 to D4 topography progresses in the lateral-to-medial direction in both areas 3b and 1, consistent with the electrophysiology maps (Figure 6d and g).

Similar to the approach we took on the fMRI data, to ensure the activation maps obtained with optical imaging were not dependent on the specific thresholding procedure, we analyzed the optical imaging data at multiple threshold levels. For each stimulus condition, we performed t-tests between stimulus and no stimulus periods and thresholded the resulting maps at $p<10^{-3}$, $p<10^{-4}$, and $p<10^{-5}$. As shown in Figure 7 (raw maps shown in Figure 7a and d; threshold overlays shown in Figure 7b and e, respectively), there was virtually no shift in the location of activation with changing threshold (Figure 7c and f). Furthermore, the activations remained focal and exhibited minimal recruitment of additional activation zones (one small spot seen in area 1 in

Figure 7d). In parallel with our results with fMRI (Figure 3), there was up to a 2.5 -fold increase in activation size with decreasing threshold (Figure 7g): Lower thresholds resulted in slightly larger activation areas, with an ~30% increase from $p<10^{-5}$ to $p<10^{-4}$ and ~100% increase from $p<10^{-4}$ to $p<10^{-3}$ (increase for $p<10^{-5}$ to $p<10^{-4}$: 27% in d3 and 37% in D4; increase for $p<10^{-4}$ to $p<10^{-3}$: 61% in d3 and 134% in D4). Despite these increases in area with decreasing threshold, topographic organization was still maintained. Thus our conclusions in this report regarding topographic specificity are consistent across BOLD and OIS methodologies and are not dependent on the precise threshold level used.

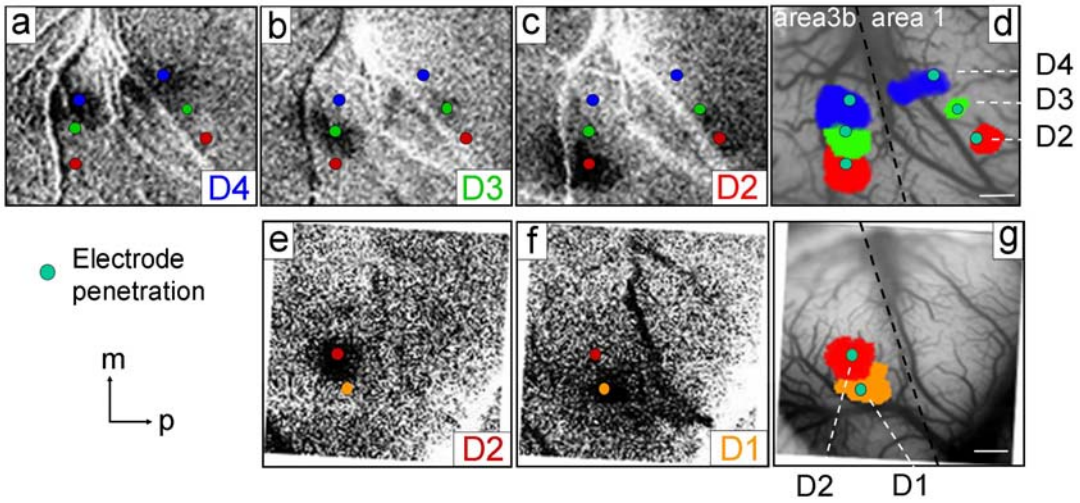

Figure 6 Optical imaging of area 3b and area 1 in response to digit stimulation in the same squirrel monkeys imaged with fMRI. Focal activations were obtained in single condition optical images in response to D4 (a), D3 (b) and D2 (c) stimulation in monkey 1, and to D2 (e) and D1 (f) stimulation in monkey 2. Stronger activations in area 3b and weaker ones in area 1 are seen in monkey 1 (a-c). The approximate border between areas 3b and 1 is indicated by the dotted line in d and g. Small color dots (a-g) indicate the electrode penetration locations for electrophysiological recording. Digits recorded are indicated by color code: D4-blue; D3-green; D2-red; D1-orange. Summary overlays of a-c in monkey 1 and e-f in monkey 2 are shown in d and g respectively. Scale bars: 1mm. m: medial. p: posterior.

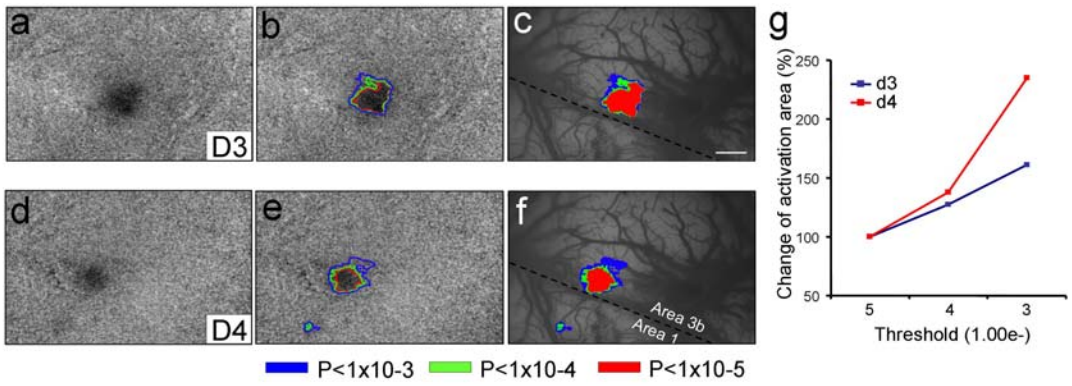

Figure 7 Effect of thresholding level on the location and size of activation revealed by optical imaging. Raw single condition images of activations in response to D3 (a) and D4 (d) stimulation (sum of 53 trials) are clipped at two standard deviations and displayed. Activation areas are defined by outlining pixels for which the signal change was significant at $p < 10^{-5}$(red), $p < 10^{-4}$(green), and $p < 10^{-3}$(blue) for D3 (b) and D4 (e), respectively. Activations derived at various thresholds are overlaid for comparison of activation size (c and f). Activation area as a function of threshold p values (normalized to the activation area at $p < 10^{-5}$ = 100%) is shown in g. Scale bar: 1mm.

2.3.2.2 Similar maps with BOLD and OIS

Somatotopic maps of area 3b obtained by fMRI were compared with those collected in the same animal using optical imaging and electrophysiology. BOLD and OIS images were co-registered using a semi-automatic point-based registration algorithm (details see methods). Corresponding landmarks, such as matching vascular and structural features (lateral and central sulci) visible on the cortical surface, were selected in the structural MRI and optical maps (compare Figure 8b and c). In some cases, even some of the smaller vessels are visible in the fMRI and were used as additional alignment landmarks (see arrows in Figure 8d and e). Figure 8 illustrates the alignment of the somatotopic maps in area 3b mapped by fMRI and by optical imaging for digits D2, D3

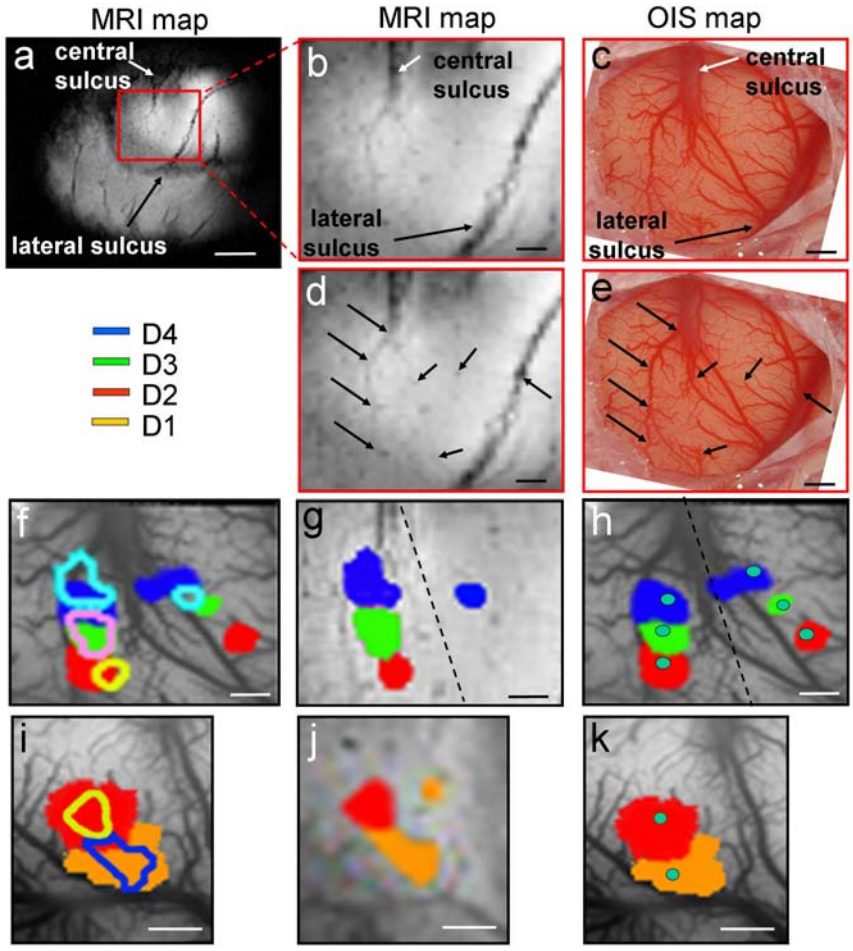

Figure 8 Comparison of somatotopic maps of fingerpads generated by fMRI, intrinsic optical imaging and electrophysiology in the same animal. fMRI and optical maps were co- registered using landmarks (e.g. central and lateral sulci) visible on the cortical surface and identifiable vascular markers (black arrows) in both the T2*-weighted structural MR (b and d) and optical blood vessel images (c and e). Comparison of the composite activation maps obtained from fMRI (g and j) and optical imaging (h and k) for digits D2 (red), D3 (green) and D4 (blue) in monkey 1, and for D2 (red) and D1 (orange) in monkey 2, respectively. Panels b-e are generated from monkey 1. Somatotopic maps of digits obtained from fMRI and optical imaging were overlaid in f (monkey 1) and i (monkey 2) for comparison. Green dots (g and i) indicate the electrode penetration locations where corresponding digit representation were identified. Scale bars: a, 5mm; b-k, 1 mm. In monkey 1 (g), activations of D4 (blue) and D3 (green) are thresholded at $p<10^{-7}$ and D2 (red) at $p<10^{-8}$. In monkey 2 (j), activations of D1 (orange) and D2 (red) are thresholded at $p<10^{-8}$.

and D4 in one animal (compare Figure 8g and h), and for D1 and D2 in a second animal (compare Figure 8j and k) under the same conditions of anesthesia and stimulation. In most cases (e.g. D3 in animal one and D1, D2 in animal 2) the locations and relative spacing of digit activations were closely matched. For D4 in animal 1, more spatial offset between the fMRI and OIS maps is apparent. This offset may be due to proximity to large blood vessels (see Figure 8f), where activations are more vulnerable to blood circulation related noise contamination. In general, with both methods, single digit activations were spaced ~ 1 mm apart.

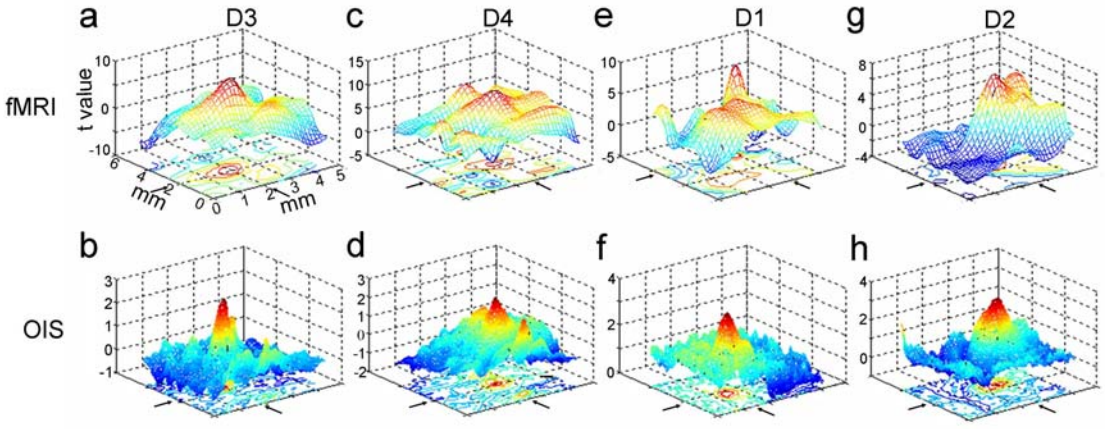

Figure 9 3D plots of fMRI and OIS activations. Four pairs of statistical activation maps of fMRI (top) and OIS (bottom) runs are shown; D3 and D4, from animal 1 (a-d) and D1 and D2, from animal 2 (e-h). Each pair of fMRI and OIS maps are aligned and displayed with the same field of view. The x- and y- axes indicate the aligned imaging plane in mm scale and the z-axis indicates the t value associated with the mean difference between stimulus and baseline conditions in both fMRI and OIS maps. Mesh is color coded to reflect t- value (blue: $t<0$; yellow/red: $t>0$). For fMRI maps, corresponding p values were: $t=5$, $p=5\times10^{-7}$; $t=8$, $p=10^{-14}$; $t=10$, $p=10^{-20}$; $t=15$, $p=10^{-35}$. For optical images, corresponding p values were: $t=2$, $p=0.02$; $t=3$, $p=10^{-3}$; $t=4$, $p=10^{-4}$. Arrows indicate activation center locations. Coordinates corresponding to t-value peaks were used to calculate offsets between locations of fMRI and OIS activations.

To further examine the similarity between the fMRI and OIS maps, we plotted the activation distribution (as measured by statistical significance, t values), and measured the activation peak locations of fMRI and OIS maps. Activation shape and peak locations between fMRI and OIS activation maps in four digits from two animals (a-d for animal 1, and e-h for animal 2) are illustrated in Figure 9. Out of the 4 pairs of fMRI and OIS maps examined, the average activation location difference was 0.14 mm (range 0.06 - 0.22 mm). We also examined the variability in trial-to-trial peak location within single fMRI sessions (average 0.21±0.07mm, 4 sessions in 4 animals). Thus, the difference in location of OIS and fMRI activaton is within the variability of fMRI localization for any given digit, indicating that the locations of the OIS and fMRI activations are not significantly different. Given the differences in methodology, the likelihood of residual anatomic coregistration errors arising from slight differences in plane of imaging, and the different signal to noise ratios, this degree of alignment is quite remarkable, and suggests the equivalence of somatotopic maps generated by high field BOLD fMRI and optical imaging.

2.3.2.3 Agreement of BOLD signal amplitude with optical imaging signal in representing funneling illusory stimuli

Previous optical imaging studies showed that the funneling illusion results in a change in activation profile: simultaneous stimulation of two adjacent digits results in an increase in activation at the central merged sites and suppression of activation at the stimulated sites (Chen et al., 2003). This change in activation profile at the central merged site does not result from a simple linear combination of maps derived from single digit activations. The present fMRI data confirm this earlier observation (Figure 5). In Figure 5a, digits D1 and D2 were simultaneously stimulated, resulting in a single

activation spot at a location between the D1 and D2 representations. Figure 5b and c quantify the activation amplitudes at each of 3 locations: the area activated by D1 (left), D2 (right), and simultaneous D1+D2 (middle) stimulation (white boxes in Figure 5a indicate sampled locations). Stimulation of D1 alone produced strong activation at the D1 site and little activation elsewhere (while columns in Figure 5b). Similarly, stimulation of D2 alone produced strong activation at the D2 site and little activation elsewhere (gray columns in (Figure 5b). In contrast, stimulation of D1+D2 (shown in Figure 5c) resulted in little activation at either the D1 (left column) or D2 (right column) sites, but strong activation at the central site (middle column); the amplitude at this central site is much greater than the sum of individual D1 and D2 stimulations at this site (compare with Figure 5b, middle column).

This non-linear summation effect was not seen with non-adjacent digit stimulation (D2+D4, Figure 5d-f). Simultaneous stimulation of non-adjacent digits D2 and D4 resulted in two activations: one at the D2 site, one at the D4 site, and none in between these sites (Figure 5d). Comparison of activation magnitudes revealed three things. First, individual stimulation of D2 or D4 alone evoked strongest activations at D2 (white columns in Figure 5e) and D4 (gray columns in Figure 5e) sites, respectively. Second, paired D2+D4 stimulation (Figure 5f) resulted in lower magnitude at each of the D2 and the D4 sites than the sums of single digit activations (compare sum of D2 activations, left columns in Figure 5e, with D2 column in Figure 5f; compare sum of D4 activations, right columns in Figure 5e, with D4 column in Figure 5f), indicative of suppressive influences with paired stimulation. And third, and in important contrast to adjacent digit activation, the location in between D2 and D4 exhibited little activation during simultaneous D2+D4

stimulation (D3 column in Figure 5f). These results were all in excellent agreement with previous optical imaging experiments (Chen et al., 2003) and confirm the ability of high field BOLD fMRI to appropriately resolve both spatial and amplitude differences at the submillimeter scale.

2.3.3 Stability of the positive BOLD signals in SI of primate cortex

Six monkeys used in this study were imaged repeatedly over a period of up to 4 months. On each animal, usually more than one digit representation was mapped. Within each imaging session, we usually map the activation of individual digits multiple times across runs.

2.3.3.1 Consistency of activation maps of individual digit across imaging runs in a single session

We examined the activation locations and amplitude of the BOLD signals across runs within a single day for experiments in three monkeys. Consistent with our previous reports (Chen et al., 2007), focal activations (Figure 10, b and c in monkey 1, g and h in monkey 2, l and m in monkey 3) were observed with BOLD fMRI during single digit vibrotactile stimulation in each run. Locations of the activation obtained from separate runs (Run1 and Run 2: Fig 10, columns 2, 3 images, with blue and green activation maps, respectively) are very consistent. For the three cases shown in Figure 10, digit activation centers completely overlapped in monkeys 2 and 3 (comparing blue and green outlines in Figure 10j and o), while there was a slight offset of activation centers in monkey 1 (Figure 10e). To increase the signal-noise ratio of BOLD response to reliably map the digit representation in area 3b cortex, we generally averaged the activation maps obtained from multiple runs for statistical analysis (Figure 10, d, i, and n). The validity of this

approach is confirmed by Fig. 10e, j, o, which shows that when the activation obtained from different runs (blue and green outlines) were overlaid on the activation maps averaged across runs (red-yellow patches), it is clear that the centers of the combined activations either co-localize with the activation from individual runs (monkeys 1) or overlap significantly with the activation centers from the different runs (monkey 2 and 3). Quantitatively, the averaged spatial offset between runs is around 0.268 mm with a range from 0.078 mm to 0.550 mm. Given the averaged 1 mm distance between two digit centers in area 3b, the 0.268 mm spatial shift counts only about 26.8 %.

2.3.3.2 Inter-session comparison

We next examined the stability of the BOLD signal across sessions on different days. Examples from 4 animals are shown in Figure 11. Single condition activation maps of each individual monkey with single digit stimulation were acquired on separate days (blue for activations acquired on the first day, green for activations acquired on the second day, b and c-monkey1, f and g-monkey 2, j and k-monkey 3, n and o-monkey 4). The activation maps acquired across sessions were co-registered and overlaid together. For all animals, focal activations at area 3b induced by single digit stimulation were clearly seen for each day (b and c, f and g, j and k, n and o). The composite maps with outlines of the activations on day 2 overlaid on the activations of day1 demonstrated the consistency of the focal activations across days as the center shifts across runs were less than 0.5 mm for all animals (d, h, i and p).

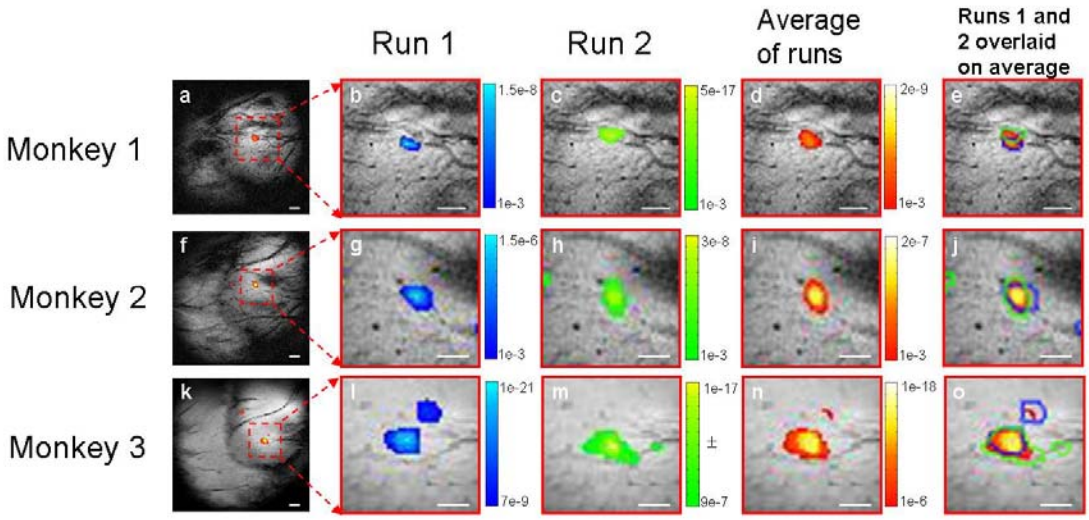

Figure 10 Inter-session stability of the BOLD activations in three monkeys (a-e for monkey 1 with D4 stimulated, f-j for monkey 2 with D4 stimulated, k-o for monkey 3 with D3 stimulated) . Within a single day experiment, two single condition activation maps of each individual monkey with single digit stimulation were compared (blue activations for run 1, green activations for run 2, b and c-monkey1, g and h-monkey 2, l and m-monkey 3). The averaged activation maps (see method) across two runs are shown in d, i and n for monkeys 1, 2 and 3 respectively. And the outlines of the single run activations wereoverlaid on the averaged activation map (blue line for run 1, green line for run 2, e-monkey 1, j-monkey 2, o-monkey3). The significance levels of the BOLD signal in b-d, g-i and l-n are indicated by their respective color bars and corresponding p value ranges. White scale bar correspond to 1mm.

2.3.3.3 Inter-subject comparison

Six animals received the same 8Hz vibrotactile single digit stimulation of digits D2, D3 and D4. The corresponding composite activation maps were shown in Figure 12. The stimulus elicited distinct focal activations in area 3b for each of the digits. Consistent with our earlier findings, the adjacent digit activations were separated by ~1 mm. The composite somatotopic organization was similar across 6 monkeys. Inter-digit activation distances support this similarity (Figure 12g): the average peak distance between digits 2

and 3 (n = 6), digits 3 and 4 (n = 10), and digits 2 and 4 (n = 6) were 1.48±0.35 mm, 1.12±0.30 mm and 1.94±0.51 mm, respectively. The average distance between non-adjacent digits was roughly 2 times the average distance between adjacent digits.

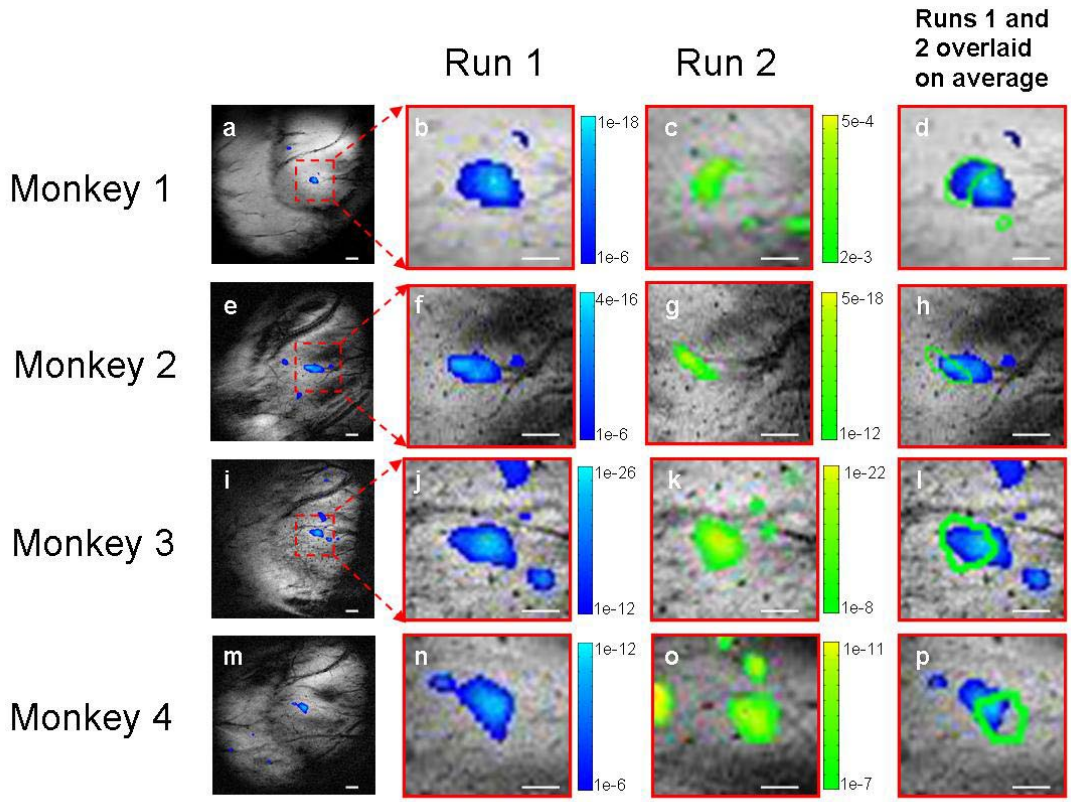

Figure 11 Intra-session stability of the BOLD activations in four monkeys ((a-d): monkey 1, D3 stimulated; (e-h): monkey 2, D3 stimulated; (i-l): monkey 3, D3 stimulated; (m-p): monkey 4, D3 stimulated). Single condition single digit activation maps for each monkey acquired from two separate days (blue: Day 1; green: Day 2; b, c: monkey1; f, g: monkey 2; j, k: monkey 3; n, o: monkey 4). Images acquired across sessions were co-registered (see methods), overlaid and shown in d, h, i, p for monkey 1-4 respectively (blue solid signal: Day 1, green outline: Day 2). The significance levels of the BOLD signal are indicated by color bars and corresponding p value ranges. White scale bar: 1mm.

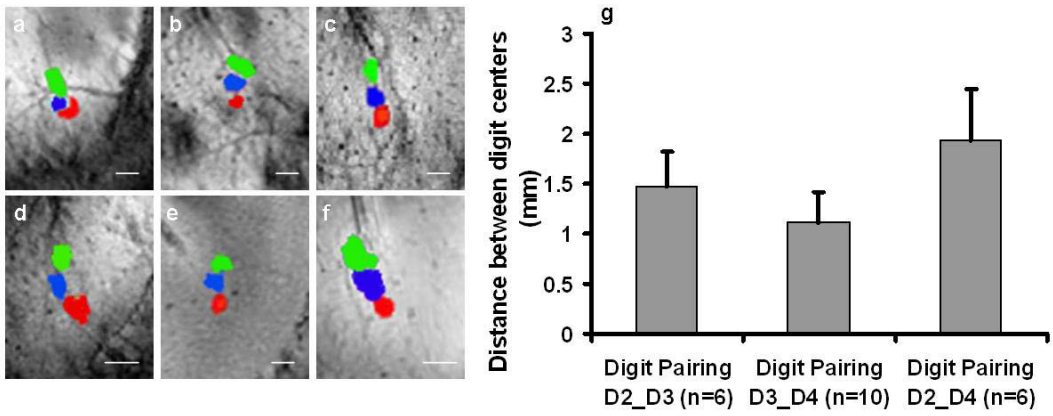

Figure 12 fMRI revealed finger topography maps in multiple monkeys. (a-f): Composite activation maps obtained for digit D2 (red), D3 (blue) and D4 (green) in six monkeys. (g): distances between the activation centers of adjacent or non-adjacent digits (calculated across animals, sessions and runs; mean ± standard deviation; n=6 for distance between activation sites at D2 and D3; n=10 for distance between activation sites at D3 and D4; n=6 for distance between activation sites at D2 and D4). White scale bar: 1mm.

2.3.3.4 Stability of BOLD signals at temporal scale

Finally, we assessed the amplitude and temporal stability of the BOLD signal. We first examined the response and consistency of signal amplitude over time within the same animal and across animals. We have already shown that in area 3b the BOLD signal time course was well correlated with the periods of stimulus presentation and interstimulus intervals (Figure 2i). The mean amplitude of the BOLD signal change in the same animal across runs within one imaging session (0.58 ± 0.27%, Figure 2j middle), across sessions (0.56 ± 0.15%, Figure 2j left), and across animals (0.60±12%, Figure 2j right) were not significantly different.

The timecourse of BOLD signal changes on two separate days for two animals are shown in Figure 13i, j. We previously demonstrated the spatial (area and location) stability of the BOLD signal change for these two cases (Fig 11a-d, e-h, repeated in Fig 13a-d, e-h). This was also the case for the reproducibility of the BOLD signal timecourse. These two cases were chosen because they represent the two cases with longest time interval between Day 1 and Day 2 (Monkey 1, 5 months; Monkey 2, 1 month). For each animal, the time courses of the BOLD signals were consistent and stable over long period of time.

2.4 Discussion

In this study, we used positive BOLD fMRI (without contrast agents), OIS, and electrophysiology to map the somatotopic representations of the distal fingerpads in the primary somatosensory cortex of the same squirrel monkeys during vibrotactile fingerpad stimulation under isoflurane anesthesia. Consistent with our previous optical imaging and electrophysiological studies, positive BOLD signal revealed distinct focal activations of individual fingerpads in area 3b, organized in a medial to lateral order from D4 to D1. The obtained BOLD responses are proved to be highly reproducible across runs within a single session, across sessions and across animals. Further alignment of fMRI and OIS maps based on cortical landmarks revealed that the locations and areas of individual digit receptive fields were in close agreement.

Furthermore, BOLD activation resolved the ~500μm spatial shift in single condition cortical activation maps accompanying the 'tactile funneling illusion'. FMRI data obtained with the funneling illusion yielded similar results to those obtained with

OIS (merging index, spatial activation profiles of paired adjacent and non-adjacent digits). Thus, as assessed by topographic mapping methods and by mapping of tactile perceptual phenomena, the positive BOLD signal can be used to achieve submillimeter spatial resolution. These observations weaken previous notions regarding poorer spatial specificity of positive BOLD signal relative to OIS and strengthen the correlation between the initial dip and the late positive BOLD.

2.4.1 Methodology

2.4.1.1 Stable and reproducible maps

Several factors contribute to the stability and reproducibility of these high resolution fMRI maps. First, the relatively subtle and focal nature of the stimuli generate very small changes in deoxyhemoglobin in draining veins leading to a notable absence of contaminating extravascular BOLD signals from draining veins and venules. Second, at high magnetic field, the short T2 of the intravascular signal (~9 ms vs. ~40 ms for tissue) (Lee et al., 1999) greatly reduces its contribution from large and small vessels. Thus, the increased spatial resolution available with high field BOLD fMRI can be attributed in part to the increased signal to noise ratio, allowing reduced voxel volumes, and in part to decreased artifact from draining vessels. Furthermore, even though the theoretical spatial resolution of the EPI data (625 x 625 μm in plane resolution) is determined by the matrix size, under high signal/noise conditions, the centroid of each activation can be localized to within the spatial resolution limit so that submillimeter shifts can be detected. From our experiments, the areas activated by our stimuli do not extend over large diffuse regions but at high field they are highly localized. As such we are able to detect shifts on

this scale. The third factor is our attention to fine tuned anesthesia levels and stable physiological conditions of the animal: expired CO_2 and blood oxygenation and TR in the fMRI sequence were constantly monitored and adjusted to provide a stable BOLD signal baseline. Under these conditions, the BOLD activation maps remained stable across runs within single sessions, across multiple sessions, and across subjects (Figs 10-13)**.**

It is noteworthy that changing the statistical threshold in the fMRI and optical activation maps led to relatively small changes in the area of activation and did not alter their locations. Over the range of thresholds explored, no spurious or unanticipated activations appeared. This robustness across threshold levels suggests that these focal activations were not artifactual byproducts of inappropriate threshholding.

2.4.1.2 Differences between OIS/fMRI stimulation paradigms

In both fMRI and OIS experiments, we used the same tactile probes, stimulation rates and amplitudes, and anesthesia methods. However, there were differences between these paradigms. The stimuli were delivered in 30 and 4 sec blocks for the fMRI and the OIS studies, respectively. Other OIS paradigms which have used longer periods of image acquisition (Kalatsky and Stryker, 2003; Nelken et al., 2004) reveal strong similarity of maps obtained with long acquisition and the traditional interleaved method. Despite these differences, the topographies obtained are remarkably similar. Thus, differences in stimulation paradigm do not qualitatively change the imaged topography or the alignment of the maps. These results confirm the equivalence of the maps irrespective of the particular stimulation paradigm.

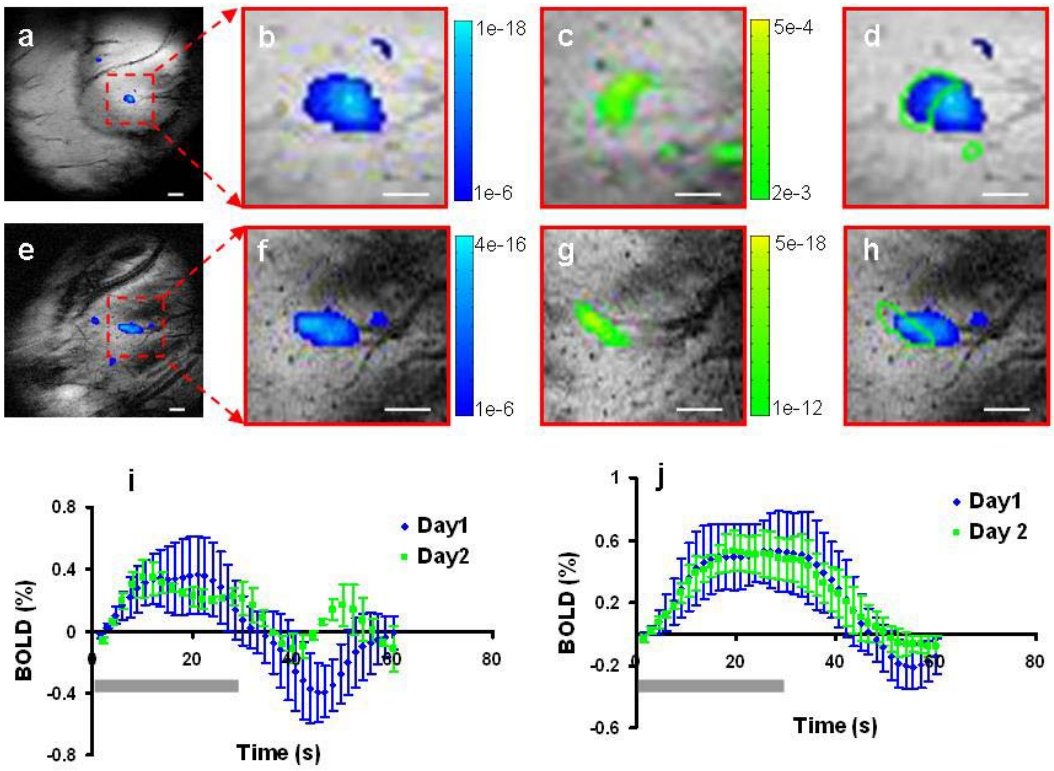

Figure 13 Stability of the BOLD signal change in area 3b over long time periods. Activation maps for monkey 1 with D3 stimulated on two different days 5 month apart are co-registered (b-activation in day1, c-activation in day 2) and overlaid (d with blue solid signal for activation in day 1 and green outline for activation in day 2). Time courses of the BOLD signals for the activated region for the two sessions are shown in i (blue-day1, green-day 2). Activation maps for monkey 2 with D4 stimulated on two different days 1 month apart are co-registered (f-activation in day1, g-activation in day 2) and overlaid (h with blue solid signal for activation in day 1 and green outline for activation in day 2). Time courses of the BOLD signals for the activated region are shown in j (blue-day1, green-day 2).

2.4.1.3 Precision of alignment

Alignment precision depends heavily on the precision of map co-registration and variability in signal/noise. Possible contributors to signal variability include variability in

physiological baseline and proximity to large blood vessels. As a result, alignment may be better in some cases than others (e.g. in Figure 9, D2 & D3 exhibit better alignment than D4, which is near two large vessels). In summary, in spite of the limitations impaired by signal variability, co-registration errors, and differences in stimulation paradigms, there was robust agreement of the OIS and fMRI topographies.

2.4.2 Previous studies showing high spatial resolution of BOLD signal

As cortical columns are believed to be the building blocks of cerebral cortical function, revealing functional structures at the millimeter and submillimeter scale is critical to understanding brain function. Higher field strength fMRI allows higher spatial and temporal resolution mapping in both animals and humans (Cheng et al., 2006; Duong et al., 2000a), for review see (Harel et al., 2006b). At the submillimeter level, for example, previous studies have shown that the initial negative BOLD (the 'initial dip') (Duong et al., 2000a, , 2001), CBF signal (Duong et al., 2001; Kim and Duong, 2002), and CBV-based fMRI (Zhao et al., 2005) can resolve columnar and laminar organization in sensory cortices and retina (Cheng et al., 2006; Fukuda et al., 2006; Harel et al., 2006a; Logothetis et al., 2002; Lu et al., 2004; Sheth et al., 2004; Silva and Koretsky, 2002; Zhao et al., 2005). Although our BOLD images were acquired at the same field strength (9.4T) as reported by Duong et al 2000, we did not detect any initial negative BOLD signal. This may be due to our lower temporal sampling rate (TR 1.5 sec versus 500ms in Duong et al), differences in baseline vascular and hemodynamic status, and differences in stimulus characteristics (low intensity focal vs. high intensity large visual field stimulation). In humans, resolution of millimeter-scale ocular dominance and orientation

domains in V1 was achieved at 4T in subjects with optimal cortical geometries using optimized surface coils and extreme head stabilization efforts (Cheng et al., 2001). Further refinement of these approaches (Harel et al., 2006b; Norris, 2006; Yacoub et al., 2005) promises to provide answers to many functional organizational and evolutionary questions on cortical organization (e.g. whether submillimeter functional units exist in human cerebral cortex).

2.4.3 Correlation of BOLD, OIS, and electrophysiology: linkage between human and animal studies

In human studies, OIS maps showed better correlation with electrophysiological maps than did BOLD maps, although better correlation with the initial negative BOLD component has been suggested (Cannestra et al., 2001). In line with this observation, BOLD activation maps exhibited considerable spatial variation compared to electrophysiologically defined maps in monkeys (Disbrow et al., 2000). These findings focused attention on whether differences in maps obtained with different techniques are due to technical limitations, to the specific cortical area studied, or to inherent differences in the different mapping signals (Cannestra et al., 2001; Cannestra et al., 2004; Kim et al., 2000). The current study suggests parallels between the BOLD and OIS, at least for our mapping paradigm in SI of the anesthetized monkey. The possibility remains that such parallels may not always be obtained. It is worth noting that, although in general the fMRI and OIS maps appear very similar, the degree of similarity must be interpreted with caution, as quantitative comparison is dependent on the precision of map co-registration methods.

The relationships between the BOLD signal and local electrophysiology remain poorly understood, but fMRI studies in non-human primates have contributed dramatically to system and cognitive neuroscience as well as our understanding of the biophysical basis of the fMRI signal (Denys et al., 2004; Gamlin et al., 2006; Gretton et al., 2006; Shmuel et al., 2006). Furthermore, fMRI studies on non-human primates can provide a link between decades of studies with single/multiple unit and/or local field potential recordings conducted in behaving monkeys and fMRI studies in humans (Orban et al., 2003; Tsao et al., 2006; Vanduffel et al., 2002). The positive BOLD signal has been shown to correlate more strongly with local field potentials than with single unit recordings (Kayser et al., 2004; Logothetis et al., 2001), and negative BOLD signal changes are associated with reduced neuronal activity (Shmuel et al., 2006). Interestingly however, apparent mismatches between electrophysiological and BOLD (or OIS) responses have been reported in the prefrontal cortex of awake monkeys (Disbrow et al., 2000; Sawamura et al., 2006). Thus, whether other possible contributions to the BOLD become more prominent under certain contexts remain to be further established.

2.5 Summary

This study reports the first direct comparison of somatotopic maps in the same animal obtained using high field BOLD fMRI and optical imaging, and also demonstrates sub-submillimeter spatial resolution mapping of cortical activity using high field positive BOLD fMRI (without contrast agents). The finger topography obtained with BOLD fMRI is proved to be highly reproducible across runs within a single session, across sessions and across subjects. These results confirm the topographic equivalence of these

methods, and suggest that fMRI is an effective and appropriate tool for mapping the functional topography of brain areas not easily accessible using other methods. Moreover, these results suggest a significant correlation between the intrinsic optical signal, believed to correspond to the negative 'initial dip', and the late positive BOLD.

CHAPTER III

CHARACTERISTICS OF BOLD SIGNAL IN SI OF PRIMATE CORTEX

3.1 Overview

BOLD-fMRI is an increasingly widely used non-invasive tool for functional brain mapping in humans and animals (Duong et al., 2000a; Hamzei et al., 2002; Li Hegner et al., 2007; Logothetis et al., 1999; Masamoto et al., 2007; Nagaoka et al., 2006; Stippich et al., 1998; Van Camp et al., 2006; Vanduffel et al., 2001; Yacoub and Hu, 2001; Zhu et al., 1998). The BOLD signal change associated with changing regional brain activity results from a complicated interaction of changes in cerebral blood flow (CBF), blood volume (CBV) and oxygen consumption ($CMRO_2$) following neuronal activation (Buxton et al., 2004; Hyder et al., 2001; Ogawa et al., 1993a; Ogawa et al., 1993b; Wu et al., 2002). The continued development of BOLD fMRI as a quantitative probe of neuronal activity in humans requires a detailed understanding of the quantitative dependence of the BOLD signal on neural activity, and particularly how accurately changes in underlying neural activity can be inferred from changes in the BOLD signal. The non-human primate, by virtue of allowing correlated measurements of BOLD signal change and neurophysiological responses to the same stimulus, offers a unique opportunity to study the nature of these dependences in a species whose cerebral anatomy, cortical organization and cytoarchitecture closely resemble those of humans.

By combining BOLD fMRI, optical imaging and electrophysiology studies in the same animals, we have demonstrated, in chapter 2, a close correspondence of the fine

somatotopy delineated by the three different mapping methods, and have demonstrated that high field BOLD fMRI is capable of resolving the somatotopic organization of individual digits in single condition activation maps in area 3b of SI with sub-millimeter spatial resolution (Chen et al., 2007). In earlier studies, Chen and colleagues used a combination of optical imaging and electrophysiology to study the response properties of the optical intrinsic signal and their relationship and dependence on the response properties of neurons in the activated regions across a range of sensory stimuli (Chen et al., 2001; Chen et al., 2003). These studies demonstrated a complex dependence of the amplitude and spatial extent of OIS response on the detailed nature of the tactile stimulus that reflected the recruitment of different and often overlapping populations of slow and rapidly adapting neurons depending on the specific properties of the sensory stimulus. Nonetheless, they observed that for a specific vibrotactile stimulus, increasing stimulus intensity (by increasing amplitude of mechanical indentation of glabrous fingerpad) evoked an increasingly strong and more spatially extensive OIS response in area 3b, and more variable responses in area 1. The increased amplitude of the optical signal correlated with an increased single unit activity (unpublished data). This leads to the hypothesis that stimulus intensity is encoded in the primary somatosensory cortex by both increased neuronal firing rate and recruitment of more neurons, which are reflected in increased OIS intensity and area of activations. In this section we explore the dependence of the BOLD signal change on stimulus intensity.

Currently, most animal and human fMRI studies focus on the positive BOLD signals which have generally been shown to be coupled to increases in neuronal activity (Devor et al., 2003; Kayser et al., 2004; Logothetis et al., 2001; Mathiesen et al., 1998;

Mukamel et al., 2005; Niessing et al., 2005; Sheth et al., 2003; Smith et al., 2002; Thompson et al., 2003). A few investigators have also reported sustained negative BOLD responses in fMRI (Allison et al., 2000; Fransson et al., 1999; Huang et al., 1996; Rauch et al., 1998; Smith et al., 2000). Those negative BOLD signal changes represent prolonged decrease in BOLD signal below baseline that are correlated with the stimulation period, and are distinct from the 'initial dip' sometimes seen immediately prior to the positive BOLD responses. This sustained negative BOLD signal changes is poorly understood. Using the same high resolution techniques described in chapter 2, we observed focal negative BOLD responses in somatosensory and sensorimotor areas adjacent to but distinct from the positive BOLD signals in the primary somatosensory cortex (Chen et al., 2007). In this chapter, we also explore the characteristics of these negative BOLD signals, including their temporal characteristics and dependence on stimulus intensity.

3.2 Experimental protocol

3.2.1 Animal Preparation

The animal preparation procedure was similar to that described previously in Chapter 2 (Chen et al., 2007).

3.2.2 Stimulus Protocol

The basic stimulation protocol was also similar to that described previously in Chapter 2, with the added feature that for these studies we varied stimulus intensity by

varying the maximum displacement amplitude of the plastic probe tip at a fixed 8Hz vibratory frequency. The probe displacement is proportional to the piezo driving voltage. For most studies, three stimulus intensities (corresponding to displacements of 0.34mm, 0.38mm and 0.42mm) were delivered to a single digit in a study session. For a subset of studies, a larger range of stimulus intensities was explored (0.22-0.46 mm displacement). Stimuli were delivered using a block-design (30s on/ 30s off), and stimulus intensities were randomly assigned within a single day experiment. The timing of stimulus presentation was externally controlled by the MR scanner and was synchronized to image acquisition.

3.2.3 MR Methods

The acquisition (structural and functional) was the same as previously described in Chapter 2.

3.2.4 fMRI Data Analysis

Basic fMRI data analysis was the same as that described in Chapter 2, with the following additional procedures specific to this study. To compare the area of positive BOLD activation under different stimulus conditions, an ROI was placed over SI (including both area 3b and area 1) and the number of voxels within the ROI contained in clusters greater than 2 voxels was counted. Within study sessions, the areas of cortical activation at a given stimulus intensity were normalized to the area measured at the highest stimulus intensity (0.42 or 0.46 mm) acquired during that session. Finally, the mean and standard deviation of the normalized voxel numbers at each stimulus intensity

were calculated across animals. A similar procedure was used to determine the dependence of the extent of area 3b activation alone on stimulus intensity.

We also used 3 dimensional mesh graphs of the t-map surface within a 4x4 mm^2 or 6x6 mm^2 FOV covering the SI activation areas to visualize and further analyze the boundaries of areas 3b and 1 under stimulus conditions where both were activated.

To investigate the locations and stability of the negative BOLD signals, we registered images across imaging sessions. First, corresponding anatomical and blood vessel landmarks in each image were identified; these coordinates were then put into a point-based registration algorithm (implemented in MATLAB). These landmarks were selected without *a priori* knowledge of the location of functional activations. For each pair of fMRI images, the registration transformation between these two sets of coordinates was then applied to one activation image, thereby co-registering the fMRI images across sessions.

To investigate the dependence of the amplitude of the BOLD (both positive and negative) response on stimulus intensity, two monkeys were scanned during single digit stimulation of the same digit over a range of 7 randomly ordered stimulus intensities (0.22 – 0.46 mm probe displacement) interleaved with baseline periods in a block design (5 epochs/stimulus intensity/run) in a single run. An activation map was first generated with all 35 epochs in each run, based on which separate ROIs covering positive BOLD areas in SI (area 3b and area 1) as well as the negative BOLD regions in sensory and sensorimotor areas were defined. The averaged BOLD signals within the chosen ROIs were then calculated separately for each stimulus intensity within a run. Finally, the

BOLD signals for every stimulus intensity were averaged across two animals (4 sessions total).

The double gamma-variate function

$$y = C_1 t^{C_3 - 1} e^{-t/C_2} - C_4 t^{C_6 - 1} e^{-t/C_5} \quad (1)$$

was used to fit the averaged positive (area 3b and area 1) and negative BOLD (sensory and sensorimotor) responses with different stimulus intensities, and these fitting curves were used to derive several parameters including area under the curve, peak BOLD response, time to peak (TTP), and full width at half maximum (FWHM), whose dependence on stimulus intensity were then tested for linearity of response.

3.3 Results

3.3.1 Positive BOLD

3.3.1.1 Dependence of Activation Area on Stimulus Intensity

Consistent with previous optical imaging and fMRI studies (Chen et al., 2003; Chen et al., 2007), single digit vibratory stimulation elicited focal activations in SI (Figure 14). The area of activation was measured at three stimulus intensities (0.34, 0.38, 0.42 mm displacement) in four animals (Figure 14b-e) and areas within sessions were normalized to the area at the highest stimulus intensity (Figure 14f-i). There was no significant difference in activation area between 0.34 and 0.38 mm stimuli (One-way ANOVA and Dunnett T3 test, p=0.99).

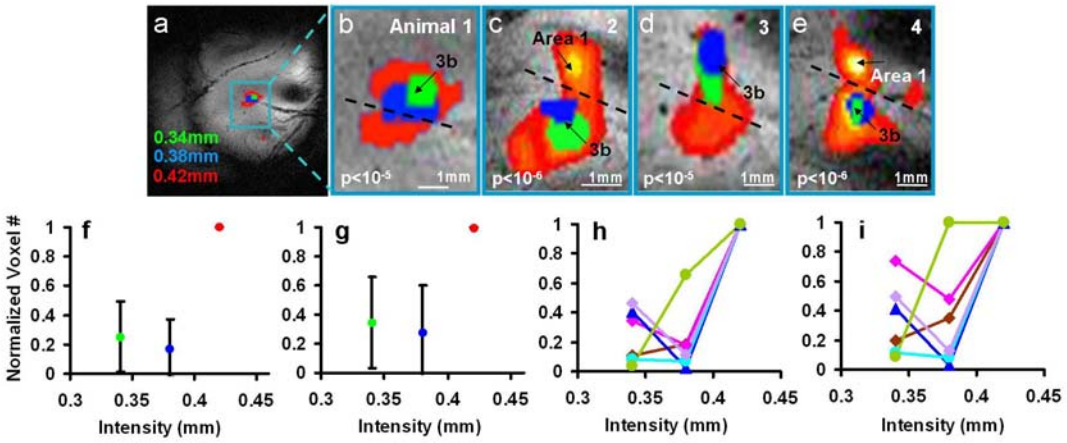

Figure 14 Effect of stimulus intensity on the size of the BOLD fMRI activation area. Vibrotactile stimulus with three different intensities (displacement values: green-0.34mm, blue-0.38mm and red-0.42mm) were applied on a single digit. Focal activations were observed in SI area which is located at the end of central sulcus (SS, marked with white arrow in a). A common threshold ($p \leq 10\text{-}5$) was applied to all three activation maps within a session. b-e are enlarged composite overlay maps for four animals with the threshold marked at the left bottom corner; scale bar represents 1mm. As shown in b-e, the activation areas stimulated with 0.42mm stimulus (red) involve multiple areas including areas 1 and 3b, while the other two stimuli mainly activate area 3b. Within a single session, for a given threshold ($p<10\text{-}5$), the voxel numbers in both area 3b and area 1 (f) or area 3b only (g) were calculated for each stimulus and then normalized to the voxel number activated by maximal stimulus intensity. Mean and standard deviation of the normalized voxel numbers for all three stimuli were calculated across 4 animals (6 sessions), and plotted against stimulus intensity (f, g). Data from individual cases are shown in (h) and (i), respectively.

In contrast, the normalized activation area in SI with 0.42mm stimulus intensity was significantly greater than with 0.34 and 0.38mm stimulus intensities (One-way ANOVA and Dunnett T3 test, $p<0.0005$ and $p<0.001$ respectively). As the local topography of the activation maps shown in Figure 14b-e illustrates, this increase reflects, to some extent, an expansion of area 3b activation at the highest stimulus intensity, but is also a result of the recruitment of area 1 at the highest stimulus. This pattern of

expansion of area 3b activation and recruitment of area 1 with stronger stimuli is illustrated in Figure 15, which compares the topography of the activation t-map surface in SI as a function of stimulus intensity in two of the four monkeys shown in Figure 14. The area 3b peak was consistently identifiable at all stimulus intensities, and its amplitude, and indeed the surrounding local topography was similar for 0.34 and 0.38 mm stimuli. In contrast, a local maximum in the t-map surface in area 1 was not observed consistently at these lower stimulus intensities (present in Figure 15b and f, not present in Figure 15c and g) and when present was generally sub-threshold (i.e. $t \leq 4.33$, $p \leq 10^{-5}$ uncorrected). The activation surface at high intensity (0.42 mm) was qualitatively and quantitatively different from the two lower intensity t-surface, and consistently revealed dual peaks, centered on areas 3b and 1 (Figure 15d and h). Furthermore, the area 1 local maximum t-value matched or exceeded that of the adjacent area 3b local maximum. To assess the global effects of stimuli and stimulus intensity on cortical BOLD signals, we also generated comparison t-map surfaces of cortical areas anatomically close to, but functionally distinct from SI. As Figure 15i-l clearly demonstrate, there is no response to the stimuli nor to increasing stimulus amplitude in this area, and the t-values are significantly lower (and sub-threshold), confirming that the increased activation area at SI (including 3b and area 1) with 0.42mm stimulus intensity were not an effect of baseline change, but a real activation that closely correlated with the increased stimulus intensity.

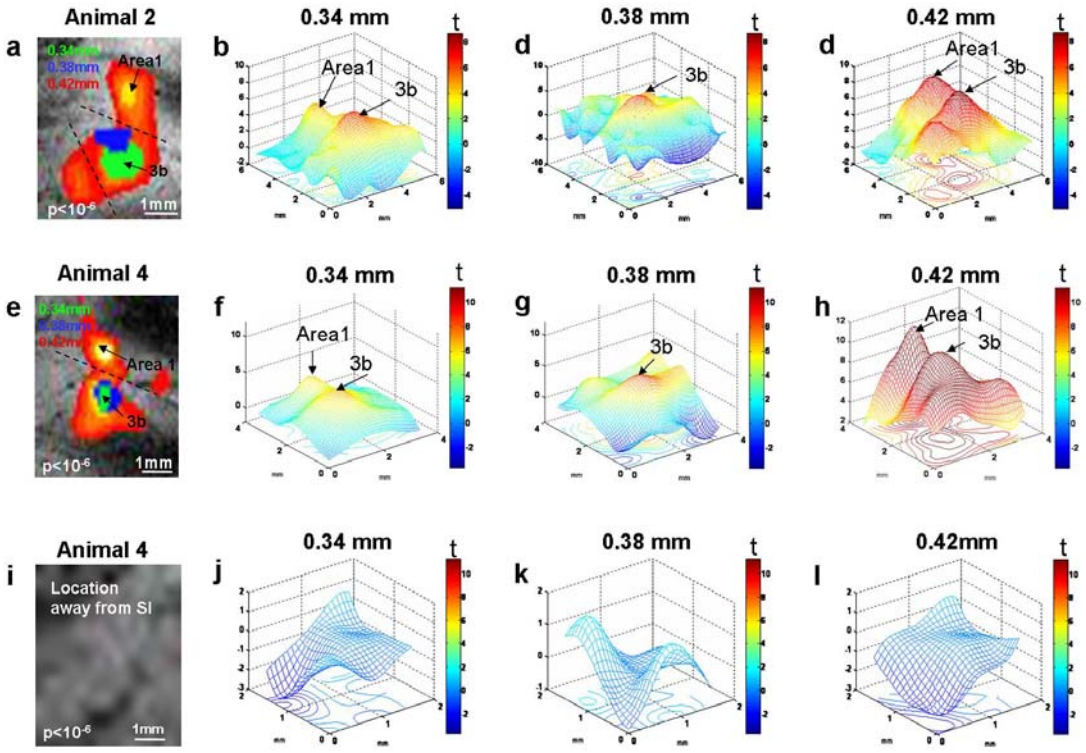

Figure 15 3D mesh representation of the fMRI activation areas in two monkeys stimulated with 3 different stimuli. Figures a and e are enlarged composite maps with activation areas stimulated by 0.34mm, 0.38mm and 0.42mm stimuli overlaid. Activation area stimulated by 0.34mm, 0.38mm, and 0.42mm displacements are indicated in green, blue and red, respectively. b-d, f-h are activation mesh maps, with x and y axis representing location of the voxel (mm) and z-axis representing t values (see colorbars). b-d are activation areas for monkey #2 (same case as shown in Fig. 14c); f-h are activation areas for monkey #4 (same case as shown in Fig. 14e). I represents a non-activated area located away from activated regions in SI. j-l are the corresponding mesh maps of this area.

Using these t-surfaces to define boundaries between SI sub-regions (e.g. area 3b, area 1), we examined further the relative contributions of expansion of area 3b and recruitment of additional areas (e.g. area 1) to the increase of activation area at the highest stimulus intensity number. By defining a smaller ROI that only involved area 3b

and normalizing the area of activation for all conditions at a given stimulus intensity within a session to that of the strongest (0.42 mm) stimulus as before for inter-animal and inter-session comparisons, we again observed (Figure 14g and i) no significant difference in area of area 3b activation between the 0.34 and 0.38 mm stimuli (One-way ANOVA and Dunnett T3 test, p=1.0), and a significant increase in area at the highest stimulus intensity (One-way ANOVA and Dunnett T3 test, p=0.004 and p=0.018 respectively).

3.3.1.2 Dependence of Activation Location on Stimulus Intensity

We next examined how stable/fixed the center of area 3b activation was with increasing stimulus intensity. To do so, we determined the location of the peak of activation in the t-surface mesh plots for all stimulus intensities in all study sessions, and calculated the mean and variance of the inter-pair distance across study sessions, for all pairs of stimulus conditions within a study session. For area 3b the mean inter-pair distance across 4 animals and 37 pairs was 0.37 ± 0.26 mm which is less than the distance between activation centers for two adjacent digits (around 1mm), confirming the stability and consistency of the functional topography in area 3b mapped by BOLD fMRI.

3.3.1.3 Dependence of positive BOLD Signal Amplitude on Stimulus Intensity

To further investigate the relationship between BOLD signal amplitude and stimulus intensity and the difference of BOLD signal at different cortical areas (3b vs. area 1), we expanded the range of stimulus intensities from 3 intensities to 7 intensities with piezo displacements ranging from 0.22 to 0.46 mm. The 7 stimulus intensities were applied in two animals (two sessions per animal, see method for more details). Fixed ROIs were defined in area 3b and area 1 separately within each session as described earlier, and the BOLD signal change within each ROI was calculated and then averaged

across animals and sessions. These averaged time courses were modeled using a double gamma variate fitting routine to extract estimates of the response amplitude.

Area 3b

In area 3b, the BOLD timecourse responses averaged across animals and sessions were strongly dependent on stimulus intensity (Figure 16a and b). This dependence was reflected in several parameters derived by modeling the BOLD signal response using a double gamma variate (Figure 17, Table 1). As Figure 17a demonstrates, the BOLD response is very well modeled by this gamma variate function. Figure 17b shows the modeled response curves generated by fitting for the 7 stimulus intensities, and their associated fitting parameters (C_1-C_6) are summarized in Table 1. To better investigate the characteristics of the BOLD signal, several characteristics including area under the curve and peak BOLD response were calculated from the model parameters and their dependences on stimulus intensity were plotted (Figure 17c-f). The results of linear regression analyses of their dependence on stimulus intensity are shown in regression plots (Figure 17c-f) and summarized in Table 2. Both the area under the curve (Figure 17c) and the peak BOLD response (Figure 17e) showed very strong linear correlations with the stimulus intensity in area 3b (Area under curve, r^2=0.97; max BOLD, r^2=0.87). Despite the very strong linear correlation, close inspection of the averaged BOLD timecourses and the dependence of the maximum BOLD signal derived from the response modeling both suggest that these parameters did not differ significantly across the three lowest stimulus intensities (0.22, 0.26, 0.30 mm), that they increased with increasing stimulus intensity between 0.30 and 0.42 mm, and began to saturate at the strongest stimuli (0.42, 0.46 mm). Thus, while the BOLD response was well modeled by

a linear dependence on the displacement amplitude, the possibility of non-linearities in the response of these parameters at very low and high stimulus intensities cannot be excluded.

Table 1 Fitting results at area 3b using Double Gamma-Variate function for BOLD signals stimulated with 7 stimulus intensities

	C1	C2	C3	C4	C5	C6
0.22mm	0.0172	13.2519	2.5346	1.60E-29	2.1944	23.4522
0.26mm	0.012	14.1223	2.627	4.07E-24	2.7267	19.112
0.3mm	0.0103	13.1457	2.7143	4.44E-37	1.7439	29.3992
0.34mm	0.0244	12.8835	2.4905	2.78E-31	2.0833	24.7852
0.38mm	0.0212	12.4869	2.5813	5.68E-38	1.7436	29.9478
0.42mm	0.0267	13.8745	2.4833	3.58E-21	3.0401	16.9125
0.46mm	0.028	12.3764	2.5024	3.38E-51	1.206	40.8968

Table 2 Results at area 3b for linear fitting between 4 characteristics of BOLD signals (Area under the curve, Full Width at Half Maximum, Maximum of BOLD, Time To Peak) and the stimulus intensity

	Slope	Intercept	r^2
Area Under Curve	27.41	2.38	0.97
FWHM	8.05	27.01	0.54
Max BOLD	0.70	0.21	0.87
TTP	-10.29	23.79	0.40

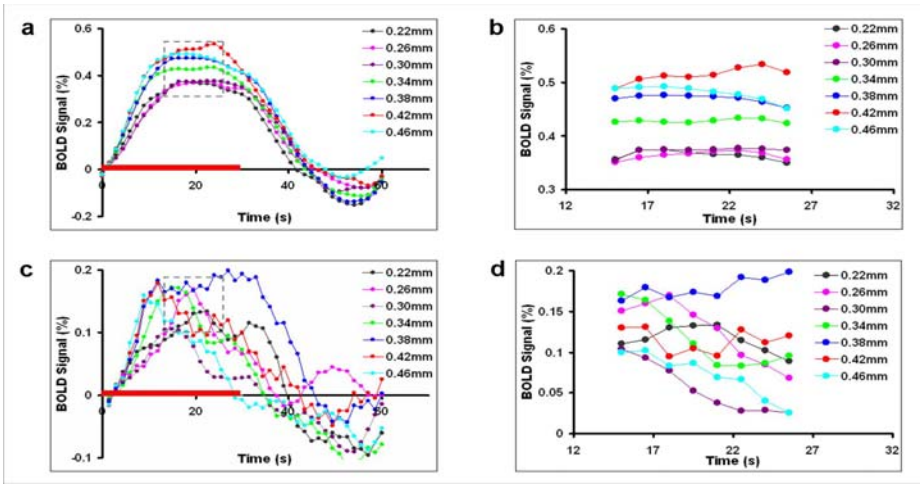

Figure 16 Time course of the fMRI BOLD signal for different stimulus intensities in area 3b and area 1. Common ROIs were chosen in area 3b (a) and area 1 (c). The mean percent signal change (StErr) for 7 stimulus intensities (ranging from 0.22mm to 0.46mm displacement) across 2 animals and 4 sessions are shown. The expanded views of BOLD signals between times points of 15s and 25.5s is shown in b and d.

Area 1

The stimulus intensity dependence of the BOLD response in area 1 was qualitatively and quantitatively different from that in area 3b. For a given stimulus amplitude, the peak BOLD signal response in area 1 was significantly less (0.1-0.2%) than in area 3b (0.35-0.55%), and did not appear to be sustained for the duration of the 30 s stimulus block (Figure 16c and e). Also, the AUC and peak BOLD signal derived from the modeled BOLD responses in area 1 (Figure 18, Table 3 and Table 4) showed no dependence on the stimulus intensity.

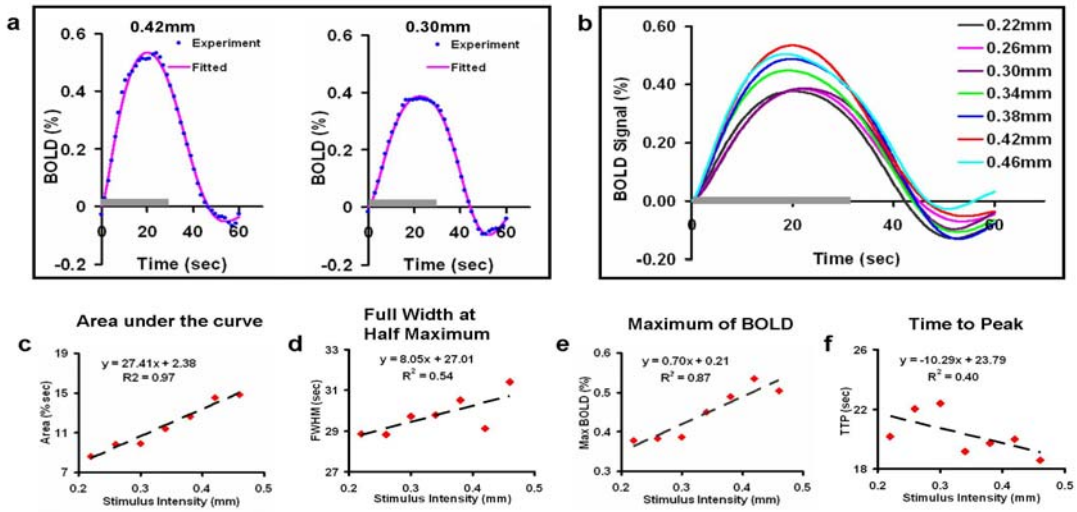

Figure 17 Fitting results of fMRI BOLD signal and its characteristics in area 3b. BOLD signals for 7 stimuli were fitted using a double gamma variate model [see methods]. a) Fitting of original data for two stimuli (0.42mm, left, and 0.30mm, right); b) Best fit curves for 7 different stimulus intensities. To examine linearity of the BOLD signal, the relationship of several parameters of the BOLD response with stimulus intensity were examined. These included: c) Area under the curve; d) Full width at half maximum (FWHM); e) Maximum BOLD signal change; f) Time to peak (TTP).

Table 3 Fitting results at area 1 using Double Gamma-Variate function for BOLD signals stimulated with 7 stimulus intensities

	C1	C2	C3	C4	C5	C6
0.22mm	0.0007	10.5266	3.6641	6.91E-05	12.7362	4.1085
0.26mm	4.78E-05	6.7185	4.9828	7.03E-08	4.7108	7.4283
0.3mm	0.0035	14.678	2.8234	5.24E-05	11.4949	4.2165
0.34mm	0.0046	11.782	2.9665	1.52E-04	12.8159	3.8682
0.38mm	0.0169	20.2441	2.1385	3.63E-41	1.5409	32.6302
0.42mm	0.0181	36.6105	2.0683	1.24E-05	12.6371	4.6022
0.46mm	0.0213	13.0865	2.425	2.50E-03	13.2743	3.0494

Table 4 Results at area 1 for linear fitting between 4 characteristics of BOLD signals (Area under the curve, Full Width at Half Maximum, Maximum of BOLD, Time To Peak) and the stimulus intensity

	Slope	Intercept	r^2
Area Under Curve	3.49	1.18	0.03
FWHM	11.66	17.66	0.04
Max BOLD	0.09	0.11	0.07
TTP	-20.82	23.08	0.19

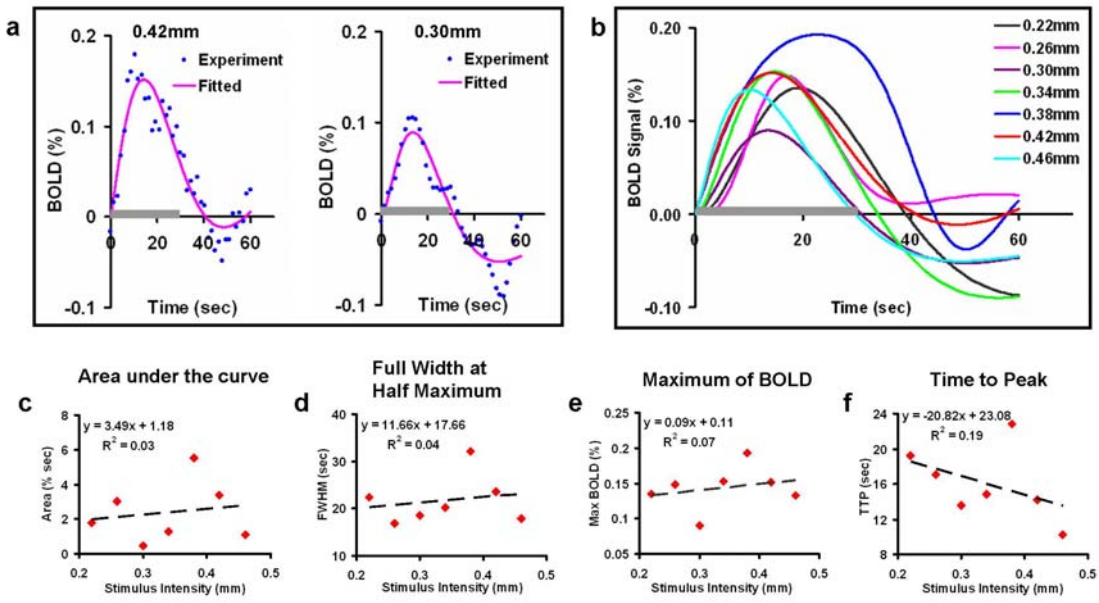

Figure 18 Fitting results of fMRI BOLD signal and its characteristics in area 1. BOLD signals for 7 stimuli were fitted using a double gamma variate model [see methods]. a) Fitting of original data for two stimuli (0.42mm, left, and 0.30mm, right); b) Best fit curves for 7 different stimulus intensities. To examine linearity of the BOLD signal, the relationship of several parameters of the BOLD response with stimulus intensity were examined. These included: c) Area under the curve; d) Full width at half maximum (FWHM); e) Maximum BOLD signal change; f) Time to peak (TTP).

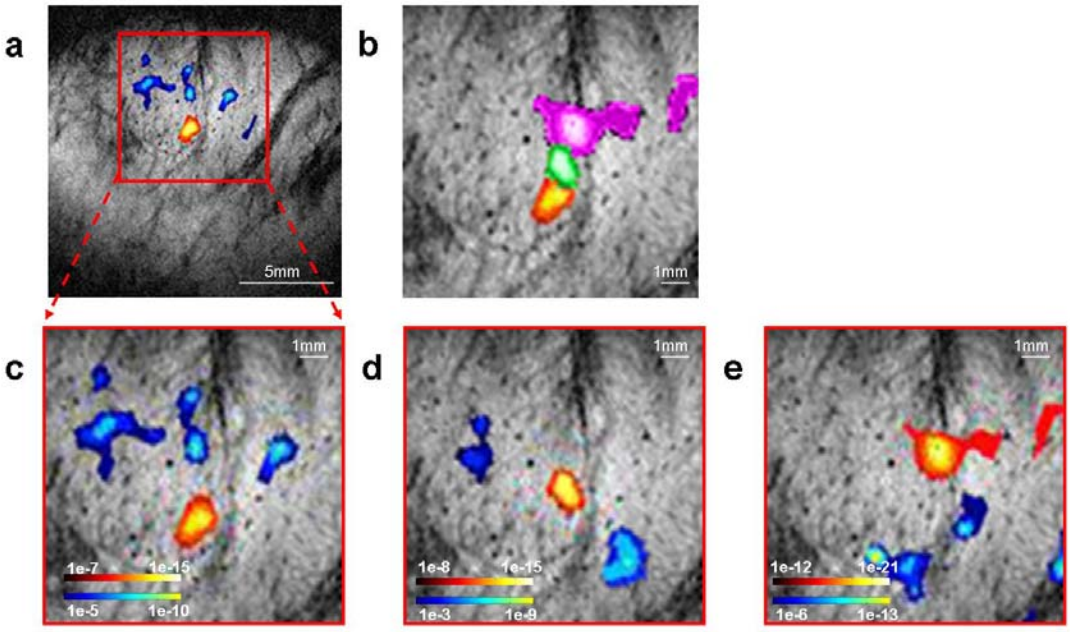

Figure 19 Focal negative BOLD signal adjacent to the positive BOLD responses. Single digit vibratory stimulation elicited focal positive BOLD activation in SI (c-D2, d-D3, e-D4, zoomed image at SI, red signals for positive BOLD). The composite map of the positive BOLD activation revealed fine topography of individual fingerpads (b, zoomed image at SI, red-D2, green-D3, pink-D4). Adjacent to the positive BOLD responses, focal negative BOLD signals were observed with each digit stimulated (c-D2, d-D3, e-D4, zoomed image at SI, blue signals for negative BOLD).

3.3.2 Negative BOLD

3.3.2.1 Consistent focal negative BOLD signals found around positive BOLD

As shown in Figure 19c-e, single digit vibratory stimulation elicited focal positive BOLD activations in SI. The composite map of these positive BOLD activations reveals the fine topography of individual fingerpads (Figure 19b) which is consistent with our previous optical and imaging studies (Chen et al., 2007), as well as what has been reported in the literature (Sur et al., 1982). However, it is evident that there are focal

negative BOLD signals near to the positive ones (Figure 19c-e). For all cases, the p values of the negative BOLD signals are less than those for positive signals, demonstrating the negative BOLD signals are smaller or more variable than the positive BOLD effects.

Figure 20b and c shows two activation maps for D2 that were acquired from two separate runs within a single fMRI session. The positive BOLD signals seen in area 3b (hot signals within red dotted square in Figure 20b and c, red and pink signals within red dotted square in the composite map in Figure 20d), as well as the negative BOLD signals in the sensorimotor area (blue signals within blue dotted square in Figure 20b and c, blue and green signals in the composite map in Figure 20d) were all highly reproducible. For the positive BOLD signals (red and pink signals in the composite map in Figure 20d), the difference in the centers of the activations between runs 1 and 2 was 0.625mm. The center shifts between runs for the negative BOLD responses (blue and green signals in the composite map in Figure 20d) in these two cases was 1.25 mm. The timecourses of the positive and negative BOLD responses (within red/blue dotted squares) for these two cases were also similar to each other (Figure 20e and f). The maximum amplitude of the positive BOLD signals for these two cases were 0.71 ± 0.29 % and 0.45 ± 0.16 % respectively which were similar to what we have reported before (Chen et al., 2007). The maximum amplitudes (absolute value of the negative peak) of the negative BOLD responses (0.49 ± 0.25 % and 0.25 ± 0.076 % respectively) were also similar, and less than those of the positive BOLD changes. Also the negative BOLD response returned to baseline faster than the positive BOLD response when stimulation stopped (Figure 20e and f). The negative BOLD responses also showed an overshoot after returning to

baseline which was approximately in phase with the undershoot observed in the adjacent positive BOLD response (Figure 20e and f).

We have demonstrated above that the negative BOLD responses are consistent within a single fMRI study. We also investigated if the negative BOLD signals are reproducible across days. In one animal, D3 was stimulated and scanned on two different days. The images across days were co-registered together using landmarks such as matching vascular and structure features (lateral and central sulci, other smaller vessels that were marked with white arrows in Figure 21b and c) that are visible on the cortical surface. The co-registered zoomed activation maps of the cortex around SI are shown in Figure 21b and c, and the overlaid image of the two is shown in Figure 21d. Consistent negative BOLD responses were observed in two locations: sensory (Figure 21d, pink square) and sensorimotor area (Figure 21d, blue square). For the example shown here, the positive BOLD in the area 3b (Figure 21d, red and yellow signals) and the negative BOLD signal at the sensory area (Figure 21d, blue and green signals within pink square) were highly reproducible across the different days, while there was a small spatial shift between the negative BOLD responses at the sensorimotor area (Figure 21d, blue and green signals within blue square). The distance between the positive BOLD and the negative BOLD responses at the two distinct areas were 2.96 ± 0.23 mm for sensory and 3.27 ± 0.67 mm for sensorimotor area (Figure 21e).

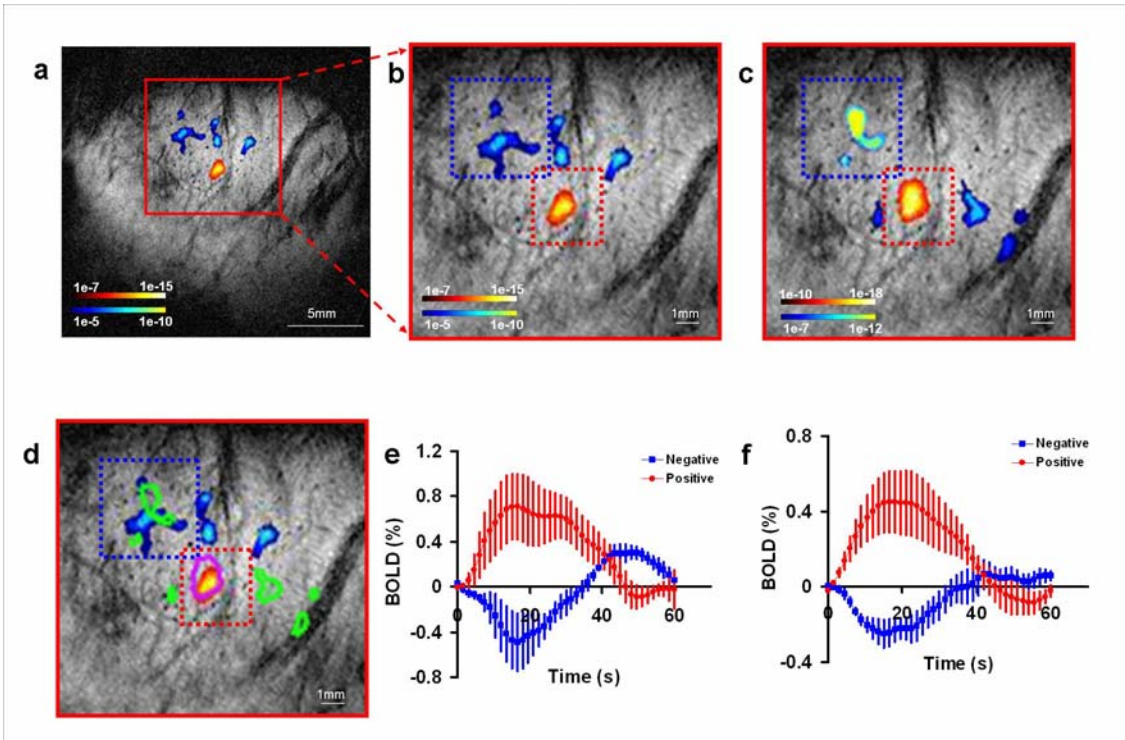

Figure 20 Reproducibility of the negative BOLD response across runs. Two activation maps with D2 stimulated were acquired from two different runs within a single fMRI session (b-run1 and c-run2, zoomed image at SI, red-positive BOLD, blue-negative BOLD). They were overlay together and the composite map were shown in d (outlines of the BOLD signals in C were overlaid on B with green outline and blue solid signals for negative BOLD signals of run 2 and run 1 respectively, pink outline and red solid signals for positive BOLD of run 2 and run 1 respectively). The positive (red) and negative (blue) BOLD responses (Mean STDEV) within red and blue squares were calculate and shown in e (run1) and f (run2).

3.3.2.2 Dependence of the BOLD signals on the stimulus intensities

To further investigate the relationship between BOLD signal amplitude and stimulus intensity as well as differences in the behaviors of BOLD signals from different cortical areas (positive BOLD in area 3b vs. negative BOLD at sensory and sensorimotor areas), we applied 7 stimulus intensities with piezo displacement ranging from 0.22 to 0.46 mm. The 7 stimulus intensities were applied in two animals. Fixed ROIs were

defined in the negative BOLD areas separately within each session as described earlier, and the BOLD signal change within each ROI was calculated and then averaged across animals and sessions. These averaged time courses were modeled using a double gamma variate fitting routine to extract estimates of the response characteristics (see above).

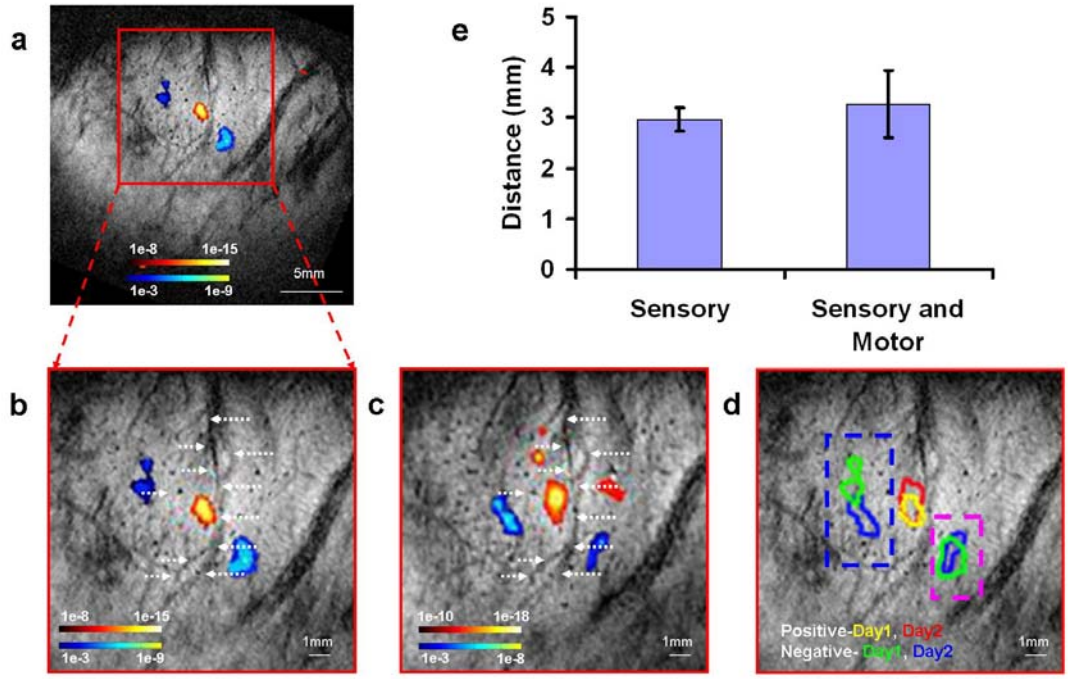

Figure 21 Reproducibility of the negative BOLD signal across days. One animal with D3 stimulated was scanned on two different days. The activation maps from the two days were coregistered using landmarks (e.g., central and lateral sulci) visible on the cortical surface and identifiable vascular markers (white arrows). The coregistered maps are shown in b (day1, red-positive BOLD, blue-negative BOLD) and c (day2, red-positive BOLD, blue-negative BOLD), as well as the composite maps shown in d (yellow and red for positive BOLD signals in day1 and day2 respectively, green and blue for negative BOLD signals in day 1 and day2 respectively). Two categories were found for the locations of the negative BOLD signals—sensorimotor area (d, blue dotted square) and sensory area (d, pink dotted square). The distances of the negative BOLD responses in the sensory and sensorimotor areas from the adjacent positive BOLD signal in area 3b are plotted in e (mean ± std, mm).

Table 5 Fitting results using Double Gamma-Variate function for negative BOLD signals at sensory area stimulated with 7 stimulus intensities

	0.22mm	**0.26mm**	**0.3mm**	**0.34mm**	**0.38mm**	**0.42mm**	**0.46mm**
C1	5.32E-05	2.87E-02	1.36E-30	1.53E-14	1.37E-39	1.33E-13	5.62E-03
C2	7.66	14.90	1.24	2.37	1.64	16.84	13.88
C3	4.71	2.18	27.56	13.74	31.27	8.56	2.43
C4	2.25E-04	1.77E-02	5.86E-04	6.33E-14	1.47E-02	4.40E-03	1.65E-03
C5	6.83	8.50	12.09	2.18	10.86	8.68	9.86
C6	4.46	2.80	3.36	13.74	2.13	3.09	3.46

Negative BOLD at sensory area

For a given stimulus amplitude, the amplitude of the negative BOLD signal response in the sensory area was significantly less (-0.07 to -0.30%, negative peaks, Figure 22a and b) than the positive BOLD in area 3b (0.35 to 0.55%, Figure 16a and b). The two-gamma variate function was used to model the response curves (Figure 23a and b) and the associated fitting parameters are summarized in Table 5. The characteristics of the negative BOLD response in the sensory area, including area under the curve, full width at half maximum, negative peak, and time to negative peak were calculated from the modeled responses and their dependence on the stimulus intensities are plotted in Figure 23c-f. Full width at half maximum showed strong positive correlation with stimulus intensity (r^2=0.68), while both area under the curve (r^2=0.33) and negative peak decrease (r^2=0.43) both showed significant negative correlations with stimulus intensity. The time to negative peak derived from the modeled negative BOLD responses at the sensory area showed weak positive correlation with the stimulus intensities (r^2=0.12). The results of the linear regression analyses of these characteristics' dependence on stimulus intensity are summarized in Table 6.

Table 6 Results for linear fitting between 4 characteristics of negative BOLD signals at sensory area (Area under the curve, Full Width at Half Maximum, Negative Peak, Time to Negative Peak) and the stimulus intensity

	Slope	Intercept	r^2
Area Under Curve	-23.92	4.69	0.33
FWHM	69.61	-0.49	0.68
Negative Peak	-0.50	0.00	0.43
TTNP	20.47	12.06	0.12

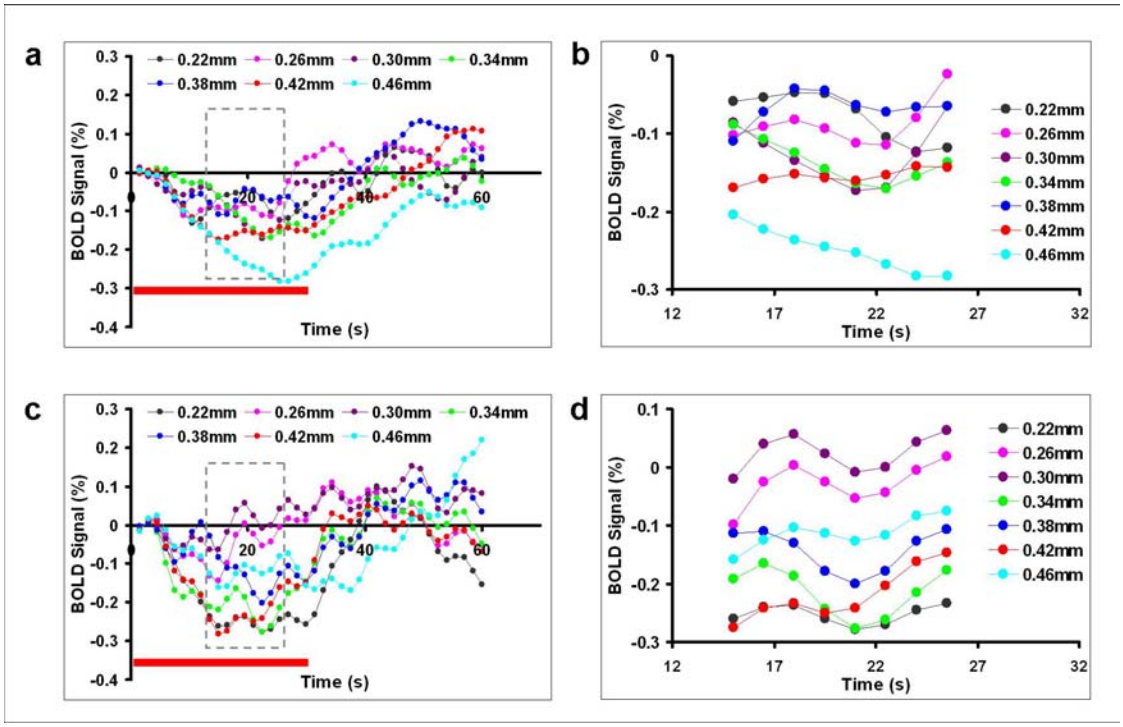

Figure 22 Time course of the negative BOLD signals for different stimulus intensities at sensory and sensorimotor area. Common ROIs were chosen for negative BOLD signals at sensory and sensorimotor areas individually. The mean percent signal change for 7 stimulus intensities (ranging from 0.22mm to 0.46mm displacement) across 2 animals and 4 sessions are shown in a and c. The expanded views of BOLD signals between times points of 15s and 25.5s are shown in b and d.

Negative BOLD at sensorimotor area

Similar to the negative responses in sensory area, the amplitude of the negative BOLD signals in sensorimotor area (-0.05 to -0.3%, negative peaks, Figure 22a and b) are much smaller than the positive BOLD in area 3b (Figure 16a and b). The corresponding fitting parameters derived from the two-gamma variate model are summarized in Table 7. The dependence of the BOLD signal parameters in this area are shown in Figure 24c-f. Among the four characteristics we studied, the full width at half maximum (r^2=0.19) and the time to negative peak (r^2=0.13) showed weak positive correlations with stimulus intensity, while the area under the curve and the negative peak did not show any significant dependence on stimulus intensity. The properties of the linear correlation between the characteristics of the negative BOLD signal in this area and the stimulus intensities are summarized in Table 8.

3.4 Discussion

A range of studies examining the dependence of BOLD signal change on sensory stimulus intensity in visual (Mohamed et al., 2002; Rainer et al., 2001; Tang et al., 2006; Vazquez and Noll, 1998), auditory (Robson et al., 1998) and somatosensory cortices (Krause et al., 2001; Van Camp et al., 2006) in rats, non-human primates and humans have generally concluded that this relationship is non-linear, with a relative insensitivity of the BOLD signal change to small changes in low stimulus intensities, and a saturation of the BOLD signal change with relatively large changes at high intensities (Wandell, 1999). Significant non-linearities are also evident in the temporal dynamics of the BOLD signal as a function of stimulus duration (Buxton et al., 2004; Robson et al., 1998; Tang

et al., 2006) and "duty cycle" (Birn and Bandettini, 2005). These non-linearities in the neurovascular response complicate the quantitative interpretation of BOLD fMRI signal changes in terms of changing neural activity (Logothetis and Wandell, 2004). Nonetheless, there are certain experimental conditions, under which a linear model of neurovascular coupling appears to be reasonable (Brinker et al., 1999; Mathiesen et al., 1998; Nemoto et al., 2004; Ogawa et al., 2000; Rees et al., 2000; Sheth et al., 2003; Van Camp et al., 2006). The vast majority of these studies have employed sensory stimuli designed to engage relatively large areas of sensory cortex (flashing checkerboard, tone bursts, electrical stimulation of rodent paw), and have then averaged the BOLD signal changes over the activated regions, with the implicit and sometimes explicit assumption that these averaged responses reflect the neurovascular coupling properties of anatomically and functionally homogeneous primary sensory areas. There is, however, extensive neuroanatomical, cytoarchitectural and electrophysiological evidence that such an assumption is overly simplistic. In the specific case of SI in non-human primates, four distinct somatotopically organized subregions of SI have been identified (Kaas, 1983; Sur et al., 1985; Sur et al., 1982). In the present study, we have taken advantage of the high sensitivity and high spatial resolution available in high field BOLD fMRI to examine the response properties of the BOLD signal within SI in the non-human primate, and have demonstrated significant differences in the BOLD signal response properties of two subregions of SI, areas 3b and 1, previously shown to respond to sensory stimuli in the anesthetized squirrel monkey (Chen et al., 2003; Chen et al., 2007). In addition to the positive BOLD responses, we also found consistent negative BOLD signals locating in two distinct areas (sensori and sensorimotor areas) that are only ~3mm away from the

area 3b in SI. The characteristics (signal amplitude and dependence on stimulus intensity) of these negative BOLD responses are very different from the positive BOLD signals in area 3b.

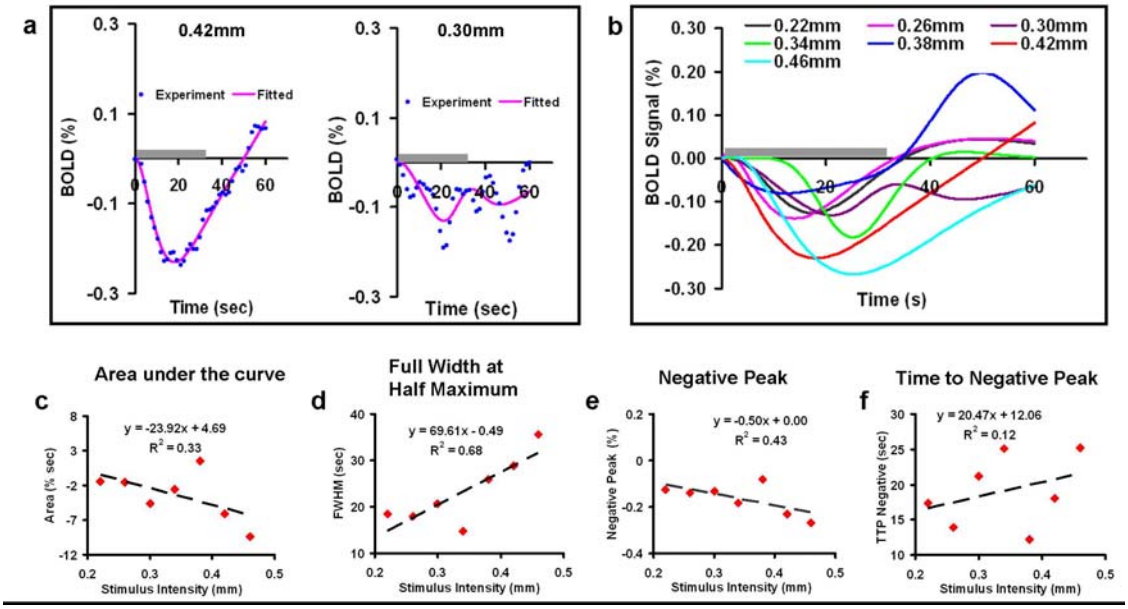

Figure 23 Fitting results of negative BOLD signal at the sensory area and its characteristics. BOLD signals for 7 stimuli were fitted using a double gamma variate model [see methods]. a) Fitting of original data for two stimuli (0.42mm, left, and 0.30mm, right); b) Best fit curves for 7 different stimulus intensities. To examine linearity of the BOLD signal, the relationship of several parameters of the BOLD response with stimulus intensity were examined. These included: c) Area under the curve; d) Full width at half maximum (FWHM); e) Negative Peak; f) Time to Negative peak (TTNP).

3.4.1 Experimental considerations

3.4.1.1 Vibrotactile vs. electrical stimulation

Many studies of the quantitative coupling of BOLD fMRI and optical imaging signals to sensory stimuli have used electrical stimulation (Ferretti et al., 2006; Krause et

al., 2001; Silva et al., 1999; Suh et al., 2006; Weber et al., 2006; Yang et al., 1997). We have chosen to use milder physiologically relevant stimuli for several reasons. Electrical stimulation, particularly at higher intensities, is relatively non-selective and may induce muscle contractions and secondary sensory stimuli related to limb and digit movements. Thus contamination of sensory with proprioceptive stimuli may be significant (Van Camp et al., 2006). Also, vibrotactile stimulation is mild compared to even relatively low-level electrical stimuli, and optical imaging and fMRI data (not shown) demonstrate a much more focal area and somatotopically organized pattern of activation, probably due in part to the more focal primary sensory stimulus without the secondary contaminations noted above, and in part because the smaller more focal physiological activations in SI lead to much smaller changes in deoxyhemoglobin concentration in distal draining venules and veins. Indeed, we have demonstrated, in chapter 2, a tight correspondence between the location and extent of activation in areas 3b and 1 during single digit vibrotactile stimulation measured in the same anesthetized squirrel monkey using optical imaging and high resolution BOLD fMRI at 9.4T, and have further demonstrated a correspondence between these maps and that obtained using single unit electrophysiology (Chen et al., 2007). Importantly, vibrotactile stimuli are behaviorally relevant stimuli that activate specific, well-characterized anatomical and functional pathways in the somatosensory pathway; the representation of such stimulus parameters in primate SI, and in particular in areas 3b and 1 are relatively well understood.

Table 7 Fitting results using Double Gamma-Variate function for negative BOLD signals at sensorimotor area stimulated with 7 stimulus intensities

	0.22mm	0.26mm	0.3mm	0.34mm	0.38mm	0.42mm	0.46mm
C1	1.87E-40	1.86E-04	5.52E-03	2.27E-15	4.98E-07	3.12E-05	1.51E-17
C2	1.26	4.75	16.71	3.55	6.37	4.98	9.34
C3	33.73	5.10	2.68	12.86	6.33	5.36	11.82
C4	1.14E-02	4.06E-04	1.37E-02	2.23E-02	1.20E-06	2.82E-04	5.46E-03
C5	18.97	4.36	13.95	23.53	5.01	4.50	20.86
C6	2.41	4.96	2.44	2.10	6.52	4.98	2.39

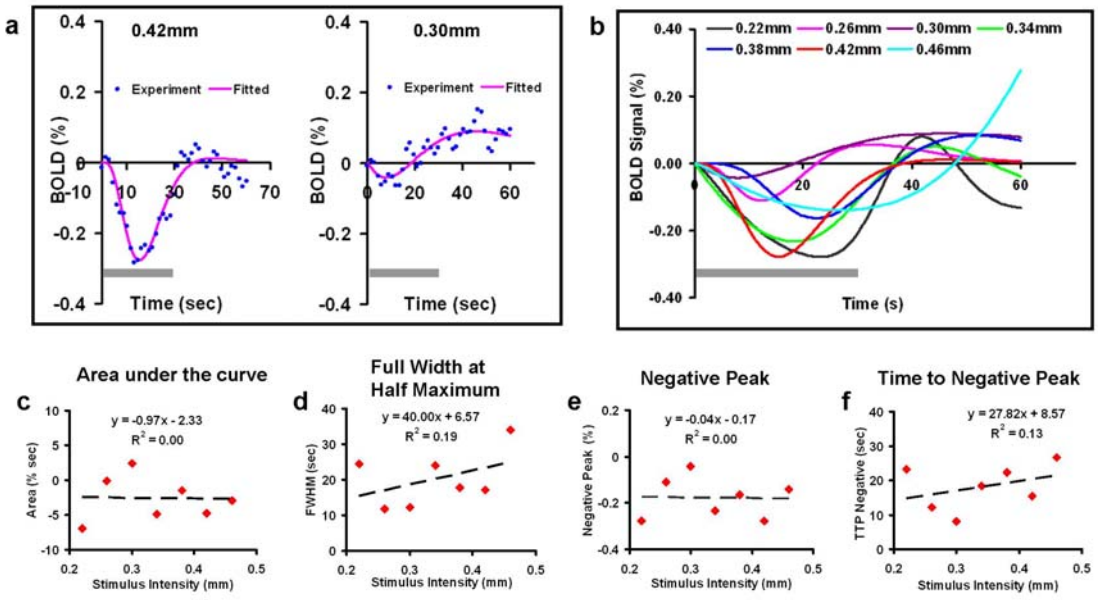

Figure 24 Fitting results of negative BOLD signal at the sensorimotor area and its characteristics. BOLD signals for 7 stimuli were fitted using a double gamma variate model [see methods]. a) Fitting of original data for two stimuli (0.42mm, left, and 0.30mm, right); b) Best fit curves for 7 different stimulus intensities. To examine linearity of the BOLD signal, the relationship of several parameters of the BOLD response with stimulus intensity were examined. These included: c) Area under the curve; d) Full width at half maximum (FWHM); e) Negative Peak; f) Time to Negative peak (TTNP).

Table 8 Results for linear fitting between 4 characteristics of negative BOLD signals at sensorimotor area (Area under the curve, Full Width at Half Maximum, Negative Peak, Time to Negative Peak) and the stimulus intensity

	Slope	Intercept	r^2
Area Under Curve	-0.97	-2.33	0.00
FWHM	40.00	6.57	0.19
Negative Peak	-0.04	-0.17	0.00
TTNP	27.82	8.57	0.13

3.4.1.2 Modulation of stimulation intensity

In this study we presented different tactile intensities to the glabrous surface of a single digit by using different displacement amplitudes of an 8Hz vibrotactile stimulus. The perceptual encoding of this stimulus as vibratory is maintained, while the perceived intensity varies across a wide range of amplitudes (unpublished observation). Furthermore, single unit and optical recordings (Chen et al., 2001) suggest that with this approach, modulation of the displacement amplitude leads to only a small increase in size of activation. Consistent with this idea, we found comparable small changes in the area of the cortex activated in area 3b with increasing stimulus intensity. The overall area of SI activation increased at higher intensities as area 1 activation achieved statistical significance. In these studies we also maintained a fixed stimulus duration that was sufficiently long to minimize the effects of non-linearities in the temporal dynamics of the BOLD hemodynamic response (Logothetis and Wandell, 2004). In these regards this study differs in its design from many previous studies which have examined the dependence of BOLD responses on stimulus frequencies (Anderson et al., 2001; Kastrup et al., 2002; Singh et al., 2003; Thomas and Menon, 1998; Van Camp et al., 2006), stimulation duration (Birn et al., 2001; Glover, 1999; Miller et al., 2001; Shmuel et al.,

2002; Vazquez and Noll, 1998), pulse widths within electrical trains (Van Camp et al., 2006), inter-stimulus intervals (Inan et al., 2004et.al.) or stimulus duty cycle (Birn and Bandettini, 2005).

3.4.2 Influence of stimulus intensity on positive BOLD activation in area 3b and 1

Electrophysiological (Sur et al., 1982), optical (Chen et al., 2001; Chen et al., 2003), and fMRI (Chen et al., 2007) studies all identify parallel somatotopically organized representations of finger tips, separated by 1-2 mm, corresponding to areas 3b and 1. Our observation that positive BOLD activation is more robust in area 3b than in area 1 in the anesthetized monkey is consistent with previous optical and high resolution fMRI studies (Chen et al., 2005; Chen et al., 2007). Indeed previous reports also suggest that the activation of area 1 in the anesthetized monkey is weak and somewhat intermittent (Chen et al., 2003, , 2005; Chen et al., 2007). Our own data (Figure 16, Figure 17, Table 1 and Table 2) indicate that area 3b shows a strong stimulus intensity dependence of the BOLD signal amplitude that is sustained for the duration of the 30 sec stimulus over a wide range of stimulus intensities. This dependence is well fit by a linear model (Figure 17, Table 2), although we cannot exclude the possibility that at very low and high intensities there may be some non-linearity.

In contrast to area 3b, area 1 showed weaker BOLD signal changes that were not sustained for the full stimulus duration (Figure 16b) and whose amplitude showed no dependence on stimulus intensity (Figure 18, Table 4), although statistically significant area 1 activation was more commonly observed at high stimulus intensities. Peak BOLD signal amplitudes were at most ~0.2%, so it is possible that in the anesthetized animal

there was insufficient sensitivity to identify any intensity coding of the BOLD signal in area 1. Preliminary optical studies in the anesthetized squirrel monkey are similarly ambiguous (Chen et al., data not shown). The weaker BOLD signal changes in area 1 must make our conclusions and interpretations somewhat more tentative. Nonetheless, it is striking that despite the very close physical proximity of areas 3b and 1, they do exhibit quite different temporal and amplitude dependences to sustained vibratory stimuli of varying intensity. Optical imaging studies comparing SI subregion responses in anesthetized and awake animals indicate not only that signals in both areas show stronger responses in the awake animal, but that the response in area 1 is stronger than in area 3b (Chen et al., 2005) Thus anesthesia may have blunted the area 1 response to a greater degree than area 3b. These studies did not examine the later temporal properties of the optical response as a function of stimulus intensity, and since they use the initial negative response in the optical mapping signal, rather than the later sustained positive response corresponding to the positive BOLD signal measured in the present experiments, they provide no information on any differences in the temporal responses of areas 3b and 1 to sustained stimulation. These optical imaging results nonetheless suggest that future studies in awake animals, combined with direct fMRI-guided electrophysiological recordings, will provide additional insights into the differing functional roles of these somatosensory areas.

In summary, this study reveals very different dependences of two subregions of SI on stimulus intensity in the anesthetized squirrel monkey. These differences are consistent with the idea that these subregions serve different functional roles, and that anesthesia differentially suppresses activation of higher order areas of somatosensory

processing in SI (e.g. areas 1 and 2) while sparing area 3b, which sub-serves the earliest stages of cortical somatosensory processing (Chen et al., 2005). Thus, while the functional relationships of SI subregions, and the way that sensory inputs to these areas are integrated remains unclear (Friston, 1998). Our data are consistent with previous suggestions of a hierarchical relationship between areas 3b and 1 (Garraghty et al., 1990), and are also consistent with a recent report that spatial-temporal receptive field responses in area 1 are less linear than those in area 3b, again suggesting that area 1 may be further along the pathway leading to an invariant tactile representation (Sripati et al., 2006).

3.4.3 Influence of stimulus intensity on negative BOLD activations in sensory and sensorimotor areas

Besides the consistent positive BOLD signals observed in area 3b, we found reproducible negative BOLD responses in adjacent non-stimulated areas in this study. The location of the negative BOLD responses can be categorized into sensory or sensorimotor areas which are only ~3 mm distant from area 3b in SI. Further investigation of the dependence of the BOLD signals on the stimulus intensity demonstrates that the influences of stimulus intensity on the area of positive and negative BOLD activations are quantitatively and qualitatively different. The amplitudes of the negative BOLD signals are much smaller than the ones of the positive BOLD. Moreover, negative BOLD at both sensory area and sensorimotor area showed weaker or no correlation with stimulus intensity in contrast to the positive BOLD responses at area 3b which showed very strong linear correlation with stimulus intensity. In different areas, the negative BOLD responses also showed different characteristics with respect to the stimulus intensity change. The negative BOLD signals in the sensory area showed

stronger linear response to the stimulus intensity than the ones in the sensorimotor area. The fact that the negative and positive BOLD responses are separated by only a few millimeters yet have very different temporal and linearity properties emphasizes the importance of high resolution fMRI acquisition, not only for mapping, but also for accurate studies of neurovascular coupling.

3.4.4 Relation of BOLD signal to neural activity

There are still relatively few studies that have directly correlated BOLD signal responses with the underlying neuronal response (Chen et al., 2007; Logothetis et al., 2001; Pouratian et al., 2002b; Shmuel et al., 2006). In this study we have not directly measured the neural response properties, and thus are unable to directly correlate the BOLD response with underlying activity in and around SI. Non-linearities in the dependence of both BOLD and optical intrinsic signals on neural electrophysiology have been reported (Disbrow et al., 2000; Sawamura et al., 2006). Several factors argue for a linear dependence of the BOLD signal amplitude change on neural activity in area 3b, however. First, experiments using similar stimulation paradigms have demonstrated a linear dependence of firing rates on stimulus intensity in early sensory areas (Arthurs and Boniface, 2003; Hyder et al., 2002; Van Camp et al., 2006). Second, while it is possible that the linear response of the BOLD signal to vibrotactile stimulus intensity emerges from offsetting non-linearities in the dependence of the cortical neural activity on stimulus intensity and BOLD signal change on change in neural activity, the more parsimonious explanation of the observed linear dependence in area 3b is that both steps are reasonably linear over the range of stimulus intensities used in this study. The same

cannot be said for the positive BOLD signal response properties in area 1 and the negative BOLD signal response properties in the adjacent areas, however, and experiments that directly compare the neural electrophysiological and BOLD responses in these areas are necessary. Such direct comparisons, as have been demonstrated previously by Logothetis and colleagues in the macaque visual system (Logothetis et al., 2001), represent the next step.

3.5 Summary

In this study, we investigated the dependence of the positive BOLD response in areas 3b and 1 of primary somatosensory cortex and negative BOLD signals in adjacent sensory and sensorimotor areas on the intensity of single digit vibrotactile stimulation. These studies revealed significant differences in BOLD response between these neighboring cortical regions and subregions of SI. The positive BOLD response in area 3b was linearly correlated with stimulus intensity over a wide range, but in area 1 there was little correlation of the positive BOLD response with intensity. Little or no correlation with intensity was found for the negative BOLD responses in sensory and sensorimotor areas. Furthermore, while the BOLD response in area 3b was sustained for the duration of the stimulus, and its amplitude scaled with stimulus intensity, the temporal response for the positive BOLD in area 1 as well as the negative BOLD responses in neighboring regions was transient and the timecourse was essentially the same across a wide range of stimulus intensities. The differences between positive and negative BOLD responses in different cortical areas as well as the differences in positive/negative BOLD responses between different subregions suggest these cortical

areas may have different roles in intensity coding, and are consistent with area 3b playing a role in the earliest steps of cortical encoding of vibrotactile sensory stimuli. Finally, the very different BOLD response properties of cortical regions and subregions of SI that are only a few millimeters apart, suggests the importance of high resolution fMRI acquisition.

CHAPTER IV

APPLICATION OF FMRI AS A NEW MAPPING TECHNIQUE TO INVESTIGATE SECONDARY SOMATOSENSORY CORTEX

4.1 Overview

Primary (SI) and secondary (SII) somatosensory cortices are two important components of the somatosensory cortex (Adrian, 1941; Marshall et al., 1937; Woolsey and Fairman, 1946). Electrophysiological and optical imaging studies in non-human primate have identified four distinct somatotopically organized architectonic fields in SI: areas 3a, 3b, 1 and 2. These four areas locate in the anterior parietal lobe in an anterior to posterior order. Each of them contains a complete map of the contralateral body representations (Carlson et al., 1986; Cusick et al., 1986; Kaas, 1983; Kaas et al., 1979; Manger et al., 1995, , 1996; Merzenich et al., 1978; Nelson et al., 1980; Pons et al., 1985; Sur, 1980; Sur et al., 1980; Sur et al., 1982). Furthermore, electrophysiology and optical imaging studies revealed that the area 3b representation of the hand is topographically organized from digit 1 to digit 5 in a lateromedial sequence (Chen et al., 2001; Coq et al., 2004; Sur et al., 1982).

Despite extensive investigations in area SI, the spatial extent and somatotopic organization of the somatosensory areas in the lateral fissure remain unclear. Until recently, it was believed that the lateral parietal cortex contained only a single region (SII) (Friedman et al., 1980; Jones and Burton, 1976). However, it has now been demonstrated that the lateral sulcus contains multiple fields, including the second somatosensory area (SII) and parietal ventral area (PV), ventral somatosensory area (VS), the retroinsular

area (Ri), and area 7b (Burton et al., 1995; Krubitzer et al., 1995; Krubitzer and Kaas, 1990; Robinson and Burton, 1980a, 1980b, 1980c). Among them, SII and PV were found to have mirror symmetric maps of the body surface and share a common boundary with PV located rostral to SII (Burton et al., 1995). The somatotopic organization in other regions includes VS, Ri and 7b have yet to be mapped.

Using the high-field (9.4T) BOLD fMRI technique, we have observed distinct, focal, and topographically organized activations of individual fingerpads in SI which are closely correlated with optical imaging maps. We have also demonstrated the existence of "funneling effect" in the SI area where simultaneous stimulation of adjacent digits elicited a single merged activation midway between the single digit activation loci, while the map for non-adjacent digits showed activations at locations corresponding to the appropriate single digit activations. This effect agrees precisely with the optical imaging data and illustrates the sub-millimeter spatial resolution of high field BOLD fMRI. As an extension of our former investigation, our goal in this study was to use high field fMRI to investigate the organization of the lateral sulcus, with an emphasis on gaining initial insight into the number of subregions in the second somatosensory area, and the digit somatotopic organization within these subregions.

4.2 Experimental protocol

4.2.1 Animal Preparation

Basic animal preparation procedures were the same as that described in Chapter 2.

4.2.2 Stimulus Protocol

Stimulus protocol was the same as that described in Chapter 2.

4.2.3 MR Methods

MR methods were the same as that described in Chapter 2, with the following additional procedures specific to this study. For 1 monkey, coronal functional and structural images were also acquired to help locate the secondary somatosensory regions (Figure 25).

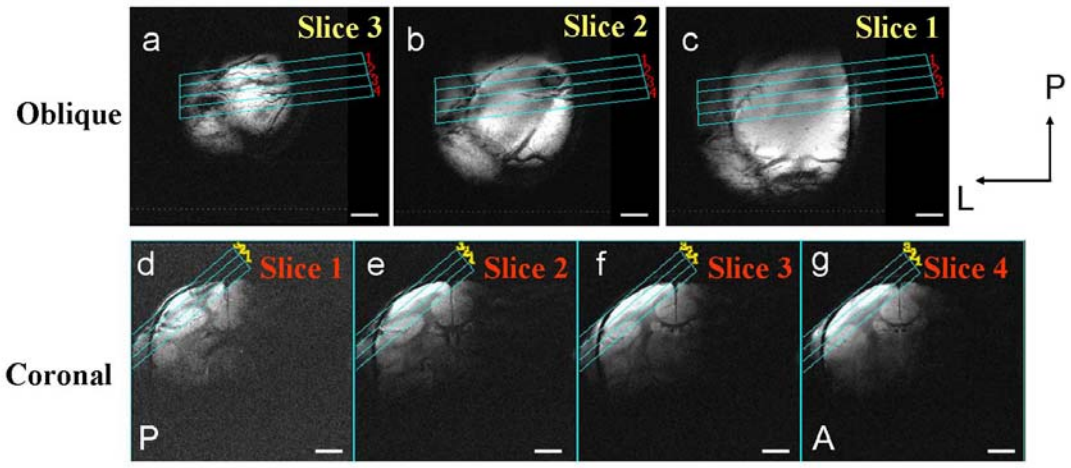

Figure 25 Oblique and coronal images were acquired within a single day experiment. a-c. Three oblique images overlaid with coronal directed images (lines marked with red characters 1-4). d-g. Four coronal images (from posterior to anterior) overlaid with oblique directed images (lines marked with yellow characters 1-3). Scale bar: 5mm.

4.2.4 fMRI Data Analysis

Basic fMRI data analysis was the same as that described in Chapter 2.

4.2.5 Calculations of Merging Index (MI)

The merging index reflects the normalized distance of the merged activation observed during simultaneous stimulation of two digits from the center of the two single-digit activations. To calculate the MI, the digit locations are set to 0 (center of one digit), 0.5 (central point between two digits) and 1 (center of adjacent digit), allowing the center of activation for the two-digit stimulation to be normalized to the same scale across cases (Chen et al., 2003).

4.2.6 Alignment of BOLD activation maps across sessions.

For image registration, we identified corresponding anatomical and blood vessel landmarks in each image; these coordinates were then put into a point-based registration algorithm (implemented in MATLAB). These landmarks were selected without *a priori* knowledge of the location of functional activations. For each pair of fMRI images, the registration transformation between these two sets of coordinates was then applied to one activation image, thereby co-registering the fMRI images across sessions (Chen et al., 2002; Hill et al., 1991). The resulting overlaps of activation zones in the image pairs were then examined.

4.3 Results

4.3.1 fMRI reveals two distinct (anterior and posterior) regions of SII

Six squirrel monkeys were studied with fMRI. Three oblique anatomical slices were planned over somatosensory cortex of the brain (Figure 1a). Clear landmarks that

are available in the squirrel monkey brain, such as the central and lateral sulci (Figure 1b) can be seen in the top slice (Figure 1c, slice3). This top slice was used to study activation in primary somatosensory cortex (Chapter 2, 3). Deeper slices (Figure 1c, slice 2, 1) were used to study lateral cortical areas such as SII which are buried in the lateral sulcus.

Figure 26 shows single condition activation maps collected from a single monkey during individual 8Hz vibrotactile stimulation of digit D1 (a, f, k), D2 (b, g, l) and D4 (c, h, m). The first row in Figure 26 shows the activations in SI, the second and third rows reveal activations in SII. Consistent with our earlier reports, each digit stimulation elicited distinct focal activation in area 3b of SI (a-c). The adjacent digit activations in area 3b were separated by ~1 mm. In this animal, individual stimulation of D1, D2 and D4 produced focal and somatotopically (D1 to D4, lateral to medial) organized fingerpad map in area 3b of SI (d and e), which is consistent with what has been reported in optical imaging, electrophysiology and fMRI studies (Chen et al., 2001; Coq et al., 2004). The individual stimulation of D1, D2 and D4 also produced activations in the two lower slices (f-o). The activations in the middle slice were more posterior than those in the bottom slice. In the middle slice, D1 (f, i, j) → D2 (g, i, j) → D4 (h, i, j) revealed an anterior-medial to posterior-lateral organization, beginning with D1 near the central sulcus. The activation in the bottom slice were more anterior, and had a more different posterior-medial to anterior-lateral D1 (k, n, o) → D2 (l, n, o) → D4 (m, n, o) organization.

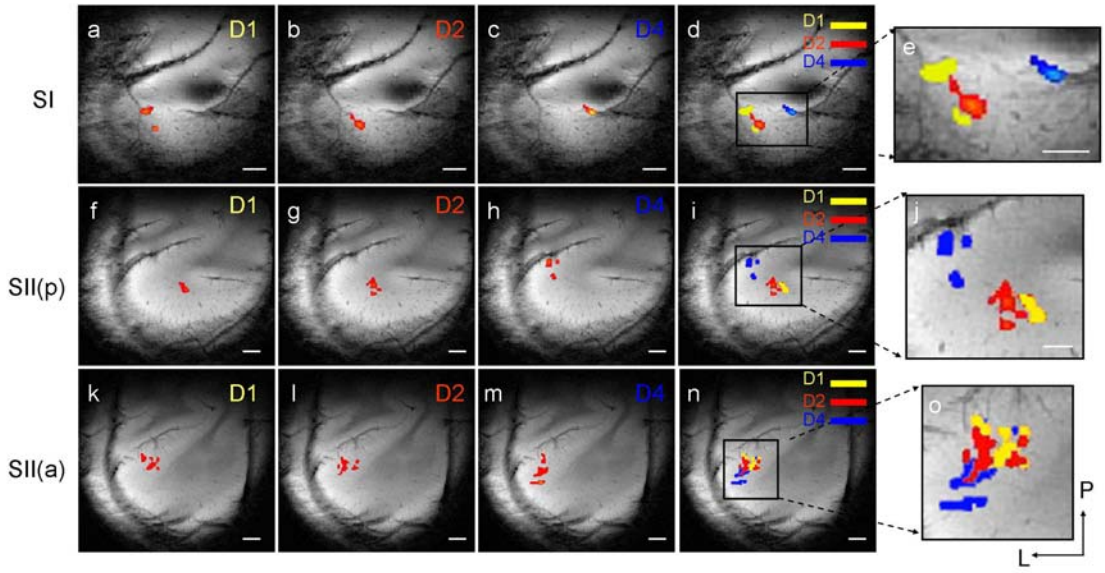

Figure 26 fMRI map of area SI (a-e), SII posterior (f-j) and SII anterior (k-o) during separate simulation of digit D1(a, f and k), digit D2 (b, g, l) and digit D4 (c, h,). Composite topography maps in SI, SII posterior and SII anterior were shown in d, i and n (yellow-D1, red-D2, blue-D4). Zoomed maps (black windows in d, i and n) at SI, SII posterior and anterior were shown in e, j and o (yellow-D1, red-D2, blue-D4). Scale bar: 1mm.

Another example is shown in Figure 27. In this animal, individual stimulation of D3 and D4 elicited focal activation in area 3b of SI (a and b). Similar to the pattern shown in Figure 26, the D3 activation in area 3b was lateral to the activation of D4. In the bottom slice, multiple activations were revealed adjacent to the lateral sulcus (Figure 27, e and f). Among which, there are two activations (within black window) located close to each other (~5.55 and 4.44 mm apart for D3 and D4 stimulation respectively). The locations of these two activations are lateral to the activations at area 3b. These two activations are most likely to be the anterior and posterior SII regions. Similar to what has been shown in Figure 26, the composite map (Figure 27, g and h), the somatotopic organization of D3 (green, g and h) to D4 (red, g and h) in these two regions is from

medial to lateral. Different from the case shown in Figure 26, a third activation was revealed in a further posterior region for digits stimulation (Figure 27, e-g, blue window). With D3 stimulated (blue window, Figure 27 e-h), the activation in this region is ~12.88 and 7.35 mm away from the SII anterior and posterior regions respectively. And it is 15.38 and 11.77 mm away from the SII anterior and posterior regions respectively during D4 stimulation. Compared to SII, the location of this region indicates this area is likely area 7.

To further examine the activation profiles at SII, we individually stimulated digit D3 and D4 of a single monkey. The activation map (statistical significance, t values) for each digit stimulation was weighted by its own maximum values ($t_{max,D3}$ and $t_{max,D4}$), to make sure the contribution of each t map to the new activation map is equal. The two weighted t maps were averaged together and re-scaled by the factor $(t_{max,D3} + t_{max,D4})/2$ to generate a new activation map (Figure 28a, b, d, e, g, h). The activation distributions in SI and SII posterior and anterior regions were plotted in Figure 28c, f, i. The corresponding activation peaks locations of adjacent digits were also calculated across subjects. In SI, distinct peaks were revealed for individual D3 and D4 stimulation (a-c), which followed the somatotopic organization of the fingerpad as mentioned above. The center distance between the adjacent digits in SI was ~1mm. Two distinct activation peaks were revealed in SII posterior and anterior regions (d-i). The distance between the SII anterior and posterior regions was 4.32 ± 1.96mm across six animals. The fingerpad patterns in SII (including both anterior and posterior regions) were medial to lateral for D3 to D4 which were opposite (mirror-imaged when the secondary cortex is unfolded) to the organization of the fingerpad in SI (lateral to medial for D3 to D4).

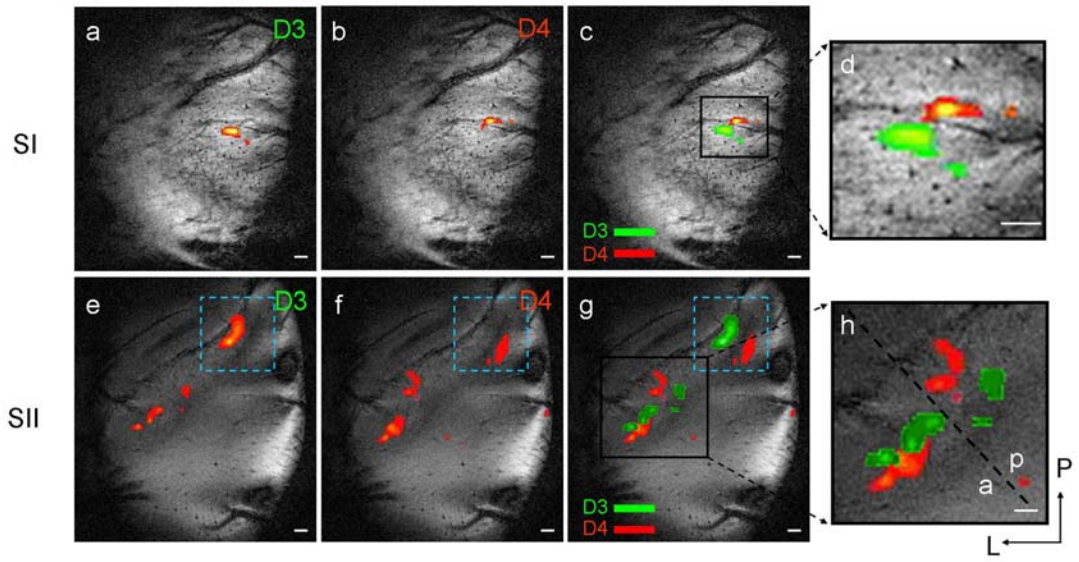

Figure 27 fMRI map of area SI (a-d), SII posterior and SII anterior (e-h, separated by dashed line) during separate simulation of digit D3 (a and e), digit D4 (b and f). Composite topography maps in SI, SII posterior and SII anterior were shown in c and g (green-D3, red-D4). Zoomed maps at SI, SII posterior and anterior regions (black windows in c and g) were shown in d and h (green-D3, red-D4). Scale bar: 1mm.

4.3.2 Reproducibility of the fMRI signal at SII

On one animal, we acquired anatomical and functional images in both coronal and oblique directions to confirm the location of the activations in the lateral sulcus area. Figure 25 showed the relationship between locations and directions of the coronal and oblique images. As shown in Figure 29, D4 stimulation elicited a focal activation in SI in the top oblique slice (Figure 29a), which is consistent with the activation in the coronal slice (Figure 29d). Two activation regions were revealed in SII by both oblique and coronal images (Figure 29c, d, f, g). Combining the activations in the anterior SII (blue color) in the bottom oblique slice (Figure 29c) and the fourth coronal slice (Figure 29d),

it is apparent that the D4 stimulation elicits activation in the upper bank of the lateral sulcus (Figure 29d). A similar effect was observed in posterior SII (green color; Figure 29c, f and g). The activations in this region were also located in the upper bank of the lateral sulcus, but were more posterior and appeared in the first and second coronal slices (Figure 25 and Figure 29). Their activations in the coronal images coincide with those in the oblique images (Figure 29c). The consistency of the activation maps acquired using two different slice orientations helped to confirm the locations of the activations in both anterior and posterior SII regions, and demonstrated the reproducibility of the activations in both regions within a single session.

To test the reproducibility of the activations in SII across sessions, we repeated the imaging of D4 in the same animal on a second day. The activation maps in SI and SII (green, Figure 30) were coregistered and compared with Day 1 maps (Figure 29a-c, blue signals in Figure 30). After coregistration, similar to previously described methods, the outline of the activation on the second day was overlaid on the activation of the first day (Figure 30d), and showed excellent agreement across Days 1 and 2, confirming that the activations in anterior and posterior SII regions are reproducible across different study days.

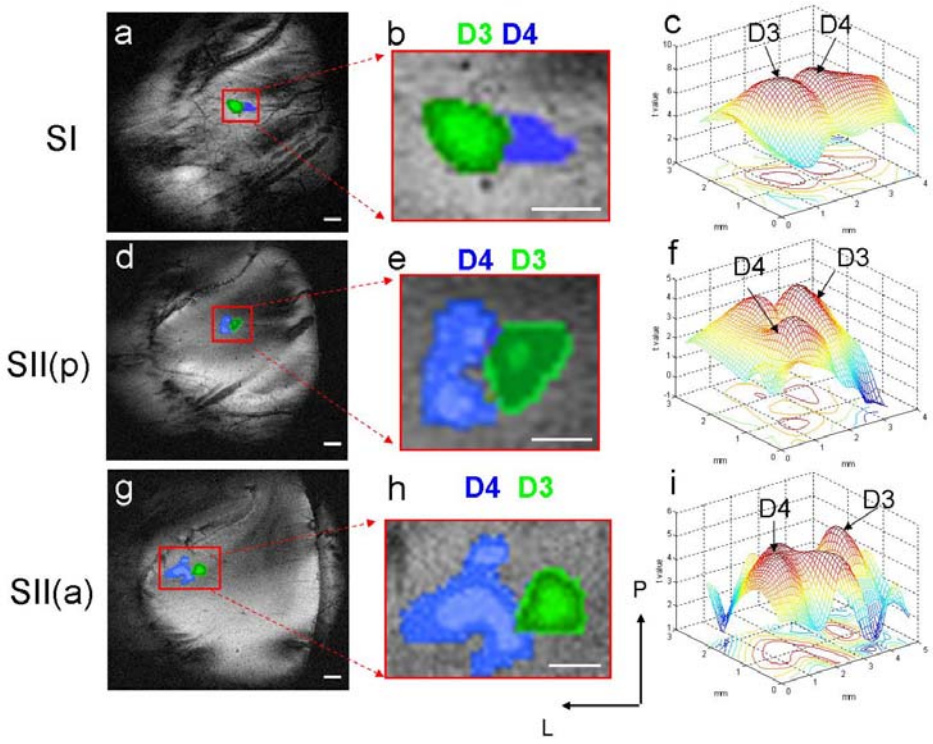

Figure 28 Composite fMRI maps of area SI (a-c), SII posterior (d-f)) and SII anterior (g-i) during separate stimulation of digit D3 (green) and digit D4 (blue). fMRI maps of Figure b, e, f are zoomed views of the activation maps (red square windows chosen in a, d and g). Figure c, f and i are mesh plots of the statistic t values (weighted and combined, see method) within the red square window for the digits stimulations. The x- and y- axes indicate the aligned imaging plane in mm scale and the z-axis indicates the t value. Mesh is color coded to reflect t-value. Arrows indicate activation center locations. Stimulation of individual digits produces single focal activation in SI (a-c), SIIa (d-f) and SIIp (g-i). Scale bar: 1 mm.

4.3.3 Fingerpad topography revealed by positive BOLD in SII

Figure 31 shows composite single digit activation maps in SI and SII for six monkeys. Consistent with our earlier studies, the activations in SI (top slice, a-f) revealed fine topographically organized fingerpad maps (D1 to D4, lateral to medial). Activations in SII were observed in one or both of the lower two oblique slices and were overlaid on

a single slice for clarity (Figure 31g-l). In all six monkeys, distinct anterior and posterior regions of activation were identified in SII. The posterior region demonstrated better somatotopic organization with a mean distances between adjacent digits of 2.56 ± 1.41 mm. The anterior region was less well organized with a mean distance between adjacent digits of 0.97 ± 0.76 mm. Both posterior and anterior SII regions were organized in a medial to lateral pattern for individual stimulation of D1 to D4.

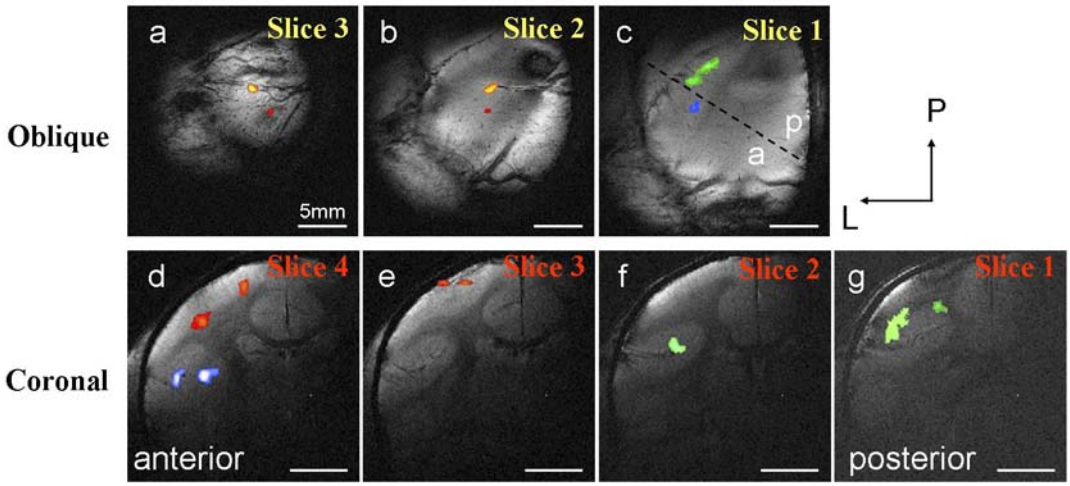

Figure 29 Activations map of SII revealed in both coronal and oblique directions with D4 stimulation. Stimulation of digit D4 produced focal activation in SI (red), SIIa (blue) and SIIp(green) areas as illustrated in oblique (a-c) and coronal (d and g) directed images. Scale bar: 5mm.

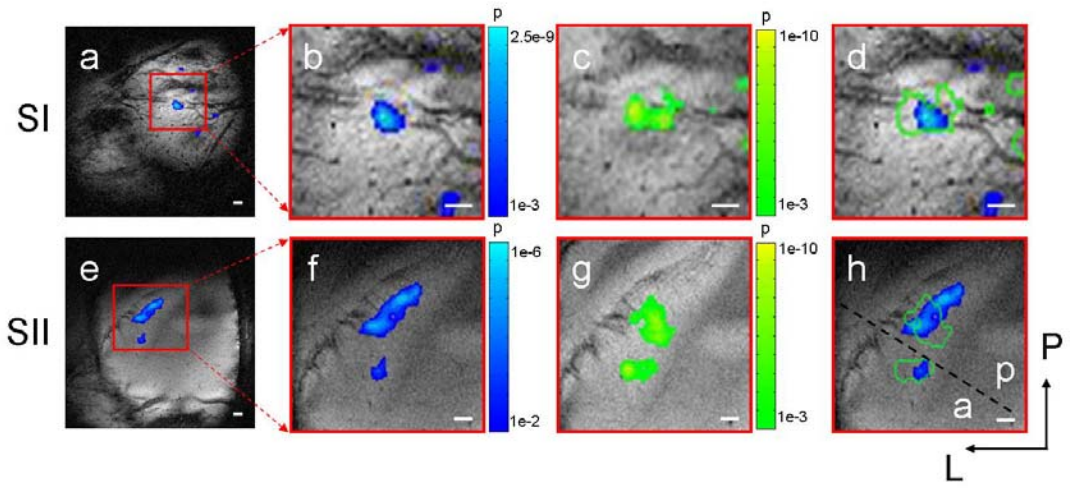

Figure 30 Reproducibility of the activations in area SI (a-d) and SII (e-h). A single animal was scanned on two different days with D4 stimulated. From each day, focal activations were found in both area SI (zoomed view in b and c, blue-Day1, green-Day2) and SII (zoomed view in f, g, Day1-blue, Day2-green). The activations acquired from the second day were overlaid on the ones acquired from the first day as showed in d (SI) and h (SII). Anterior and posterior regions were revealed in SII area (h, separated by dashed line). Scale bar: 1mm.

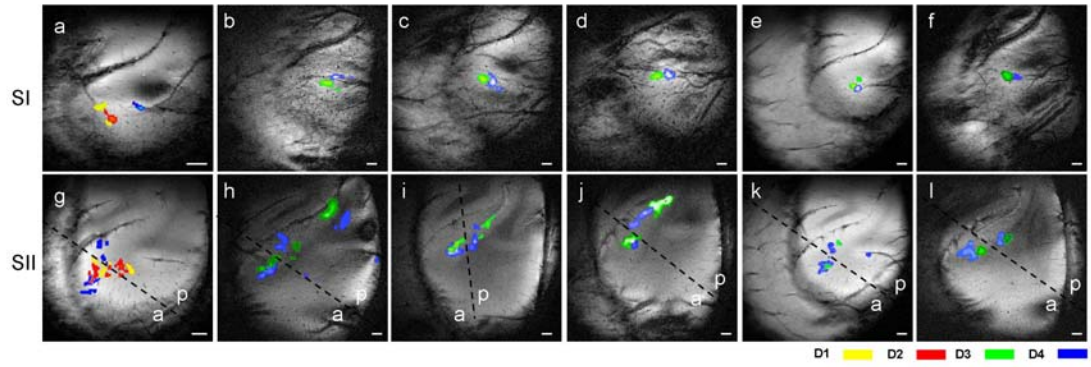

Figure 31 Digit topographic maps revealed at SI (a-f) and SII (g-i) in six monkeys. The first animal has D1 (yellow), D2 (red) and D4 (blue) stimulated separately (a and g), while the other five animals were stimulated with D3 (green) and D4 (blue) individually. Digit activations (D4 to D1) revealed a medial to lateral pattern at area SI (a-f), while a lateral to medial and posterior to anterior pattern was revealed at area SII posterior and anterior regions (g-l, anterior and posterior regions were separated by dashed lines). Scale bar: 1mm.

4.3.4 BOLD reveals the representation of funneling illusory stimuli in SII

In our earlier studies, we demonstrated that high field BOLD fMRI could resolve the sub-millimeter activation shifts in area 3b of SI previously identified as neural correlates of the tactile funneling illusion(Chen et al., 2007). In the funneling illusion, simultaneous vibrotactile stimulation of adjacent pairs of digit tips elicited a sub-millimeter shift in activation to a central merged (funneled) location between adjacent digit tips. In this study, we wished to determine whether similar funneling is present in SII.

Figure 32 shows an example of fMRI mapping of SI and SII under conditions of single and paired digit stimulation. In this case, individual stimulation of D3 and D4 generated distinct activations in SI (Figure 32a, b, m, n). A zoomed map of area 3b (turquoise rectangle in Figure 32b, n) reveals well resolved activation foci with their centers separated by ~ 1mm. Simultaneous stimulation of D3 and D4 produced a single, focal activation, midway between the activation centers generated by stimulation of D3 or D4 alone (Figure 32h, for comparison centers of activation locations are indicated by dotted red vertical lines). The merging index (MI) in SI shown in Figure 32h is 0.42 indicating the activation with D3 and D4 stimulated simultaneously was located roughly midway between the D3 and D4 activation foci.

For each condition, SII activations were revealed in both posterior (caudal) and anterior (rostral) regions adjacent to the lateral sulcus in the middle and bottom oblique slices respectively (Figure 32c-f, o-r). In the posterior region, individual stimulation of D3 and D4 generated distinct activations separated by ~ 0.7mm. Simultaneous stimulation of D3 and D4 modified our observed activations in SII. In posterior SII,

which is better organized, an additional peak located midway between the activation centers generated by stimulation of D3 and D4 alone (green arrow, Figure32j), with a MI of 0.86 suggests some sensory funneling. In anterior SII, which shows poor organization, simultaneous stimulation of D3 and D4 generated an additional activity (blue arrow, Figure 32k), but given the poor somatotopic organization, it is less clear whether this represents higher order sensory funneling.

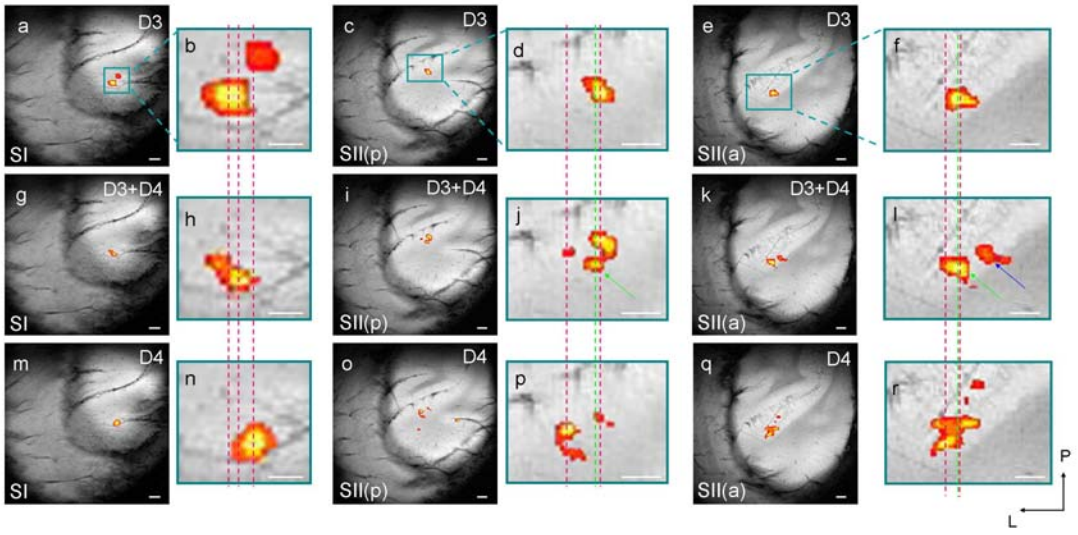

Figure 32 fMRI reveals the representation of funneling illusory stimuli at SI (a, b, g, h, m, n) and SII (c-f, i-l, o-r). Stimulation of single digits D3 (a-f) and D4 (m-r) generated single focal activations organized somatotopically in area 3b of SI. Stimulation of paired adjacent digits (D3+D4) generated a single activation in area 3b of SI (g and h), located between the sites of activation during stimulation of D3 (a and b) and D4 (m and n) alone with MI=0.42 (corresponding activation centers indicated by red dashed lines). For each stimulation condition, posterior (c, d, i, j, o, p) and anterior (e, f, k, l, q, r) activations are revealed at SII regions. Funneling illusory effect is also revealed in these locations. Activation with stimulation of paired adjacent digits (D3+D4) (green arrow) located between the sites of activation during stimulation of D3 or D4 individually with MI=0.80 and 0.93 for SII posterior (j) and anterior (l) respectively. Scale bar: 1mm. P: posterior. L: lateral. Scale bar: 1mm.

4.4 Discussion

In this study, we applied the same high field BOLD fMRI submillimeter mapping, previously validated by studies in SI, to begin high resolution mapping structures in higher order somatosensory areas, beginning with SII. Specifically, we investigated whether somatotopy in SII is also fine-grained as in SI by comparing the representation pattern evoked by the stimulation of fingers in these two regions.

4.4.1 Number of cortical fields in the lateral sulcus

One of the main findings of this study is that there are two distinct subregions in the secondary somatosensory cortex, one rostral to the other with a separation of 4.32 ± 1.96mm, and both subregions are lateral to area 3b. The discovery of these two SII subregions is consistent with recent electrophysiology studies suggesting that the SII region of the macaque monkey contains two somatotopic maps of the body surface (Burton et al., 1995; Krubitzer et al., 1995). These two subregions have been named SII and PV (parietal ventral) (Krubitzer et al., 1995) or anterior and posterior SII (Burton et al., 1995). Thus the rostral and caudal regions we found may correspond to the electrophysiologically defined PV / anterior SII and SII / posterior SII areas respectively.

Other somatosensory cortical areas have also been reported in the deeper brain regions, such as area 7b, ventral somatosensory areas (Vs), rostrolateral parietal cortex (PR) and retroinsular area (Ri) (Coq et al., 2004; Krubitzer and Kaas, 1990; Robinson and Burton, 1980a, 1980b). In one animal, we observed an activation located more medial and posterior to the SII rostral and caudal areas (Figure 27). This region is

possibly the area 7b, but confirmation of this, as well as the identification of other regions of activation must await further fMRI studies.

4.4.2 Organization of digit pattern in lateral sulcus

Several studies have reported the organizations for the body representations in the lateral somatosensory cortex in human, non human primate and several non-primate mammals (Burton et al., 1995; Cusick et al., 1989; Disbrow et al., 2003; Friedman et al., 1980; Krubitzer et al., 1995; Robinson and Burton, 1980c; Ruben et al., 2001). Posterior and anterior SII (or SII and PV) were found to extend from the border of area 3b and the upper lip of the lateral sulcus to the fundus. The body representation in SII proceeded from the face to the hand away from the area 3b border, and from the hand to the forelimb, trunk, and lower limb in a rostrocaudal sequence. The topographic organization of the body representation in PV appeared to roughly mirror that of SII (Burton et al., 1995; Coq et al., 2004; Cusick et al., 1989; Disbrow et al., 2003; Krubitzer et al., 1995; Krubitzer and Kaas, 1990; Qi et al., 2002; Robinson and Burton, 1980c). Although the topographic organizations of the body representations in PV and SII have been investigated, the somatotopic maps for digits in these two regions have not been determined. Some electrophysiological studies using non-human primate models have claimed that there is no precise topographic organization of the digit representation in SII (Burton et al., 1995; Coq et al., 2004; Krubitzer et al., 1995). However, unfortunately high resolution OIS mapping of SII is not possible since SII is buried in the lateral sulcus. The fact that finger representation in SII and PV share a common boundary (Burton et al., 1995; Krubitzer et al., 1995), further complicates the situation.

A recent human study attempted to examine the topography of different finger representations in both SI and SII using fMRI with vibratory stimulus applied on individual digit tips (Gelnar et al., 1998). In this study, multiple digit representations were observed in SI, corresponding to the four anatomic subdivisions (area 3a, 3b, 1 and 2), suggesting that the organization of human somatosensory cortex resembles that described in other primates. However, this study failed to map fine finger-topography in either SI or SII, although the investigators did report that the spatial distance between digit 1 and digit 5 cortical representations was the greatest in both SI and SII. The failure to resolve a fine digit topographic map may be due to the choice of imaging plane direction and/or slice thickness, and an insufficient spatial resolution. They acquired coronal multi-slice images with 6 mm slice thickness and 0.5mm gap between slices. With the fact that the distance between digits in either SI or SII regions is just a couple mm apart, their imaging methodologies can hardly give them the resolution that is needed to reveal the finger topography in the somatosensory cortex.

Our fMRI study has the advantage over electrophysiological methods in that we can study activities in different brain regions simultaneously and non-invasively, allowing us to perform multiple studies in a single animal over a long period of time. Our methodology also has advantages over current human fMRI studies including field strength (9.4T) to get better SNR, and correspondingly higher in-plane resolution (0.78x0.78 mm^2 for anatomical images and 0.625x0.625 mm^2 for functional images). With this experiment protocol, we have successfully mapped the somatotopic organization of fingerpads in SI (Chen et al., 2007; Zhang et al., 2007), which builds a solid base for our current study in SII. The present study provides evidence for a

somatotopic organization of digits in the secondary somatosensory cortex, and reveals distinct two sets of fingerpad topographies in the rostral and caudal SII areas. Within each area, the representations of D1 to D4 are organized in a medial-lateral pattern. The organization of the digits in SII areas is mirror-imaged (with SII unfolded) to those of area 3b and 1. The pattern we found in the lateral sulcus areas is similar to that reported in an early electrophysiology study of SII in M. fascicularis, where an ordered representation of single digits or groups of digits has been reported, with the thumb (D1) represented by a strip anteriomedial to strip representing neurons with receptive fields covering digits 1 or 2 or 3 or combinations of 2 or more of these digits (D1-3). In turn, the D1-3 representation was anteriomedial to a strip representing digits 2 through 5 (D2-5) (Robinson and Burton, 1980c).

Our present study also provided preliminary evidence of sensory funneling in SII. In this single case, with adjacent digits (D3 and D4 in our case) stimulated individually, individual activations between adjacent digits were revealed with ~0.50 and 0.72 mm (Figure 32) center shift between the activation peaks in the SII anterior and posterior regions respectively. When the two digits were stimulated simultaneously, the activations were shown to locate between the individual D3 and D4 representation sites with merging index to be 0.93 and 0.86 in the SII anterior and posterior regions respectively. However, this single case raised our attention to the differences between the activations in SI and SII:

1. The distance between adjacent digits (D3 and D4 in Figure 32) is ~1mm in SI, while ~0.50 and 0.72 mm in SII anterior and posterior regions, making it harder to distinguish between adjacent digits in SII.

2. The merging index in both SII anterior (0.93) and posterior (0.80) regions is larger than the value in SI (0.42) region, suggesting the activation with two digits stimulated simultaneously is more close to D3 activation foci in SII.
3. Multiple activations were observed in SII regions (Figure 32, blue arrow), making SII more difficult to be investigated.

All these factors suggest the somatosensory organization in SII may be less fine-grained than in SI, and they also added uncertainty in answering the question concerned with whether or not the funneling effect exists in the SII areas. More studies are required to draw positive conclusions on the funneling effect in the SII regions.

4.5 Summary

Our study provides evidence for a somatotopic organization of digits in the SII. Two distinct SII subregions (anterior and posterior) were revealed separated by 4.32 ± 1.96mm, with evidence of greater organizational fingerpad topography in posterior SII. Within each area, the somatosensory fingerpad topography (D1 to D4) was organized in a medial to lateral and anterior to posterior pattern. The topography of the fingerpads in SII was the mirror-image of those in areas 3b and 1. Finally, we provide preliminary evidence of sensory funneling in SII as well as SI. The fingerpad topography in SII revealed by monkey fMRI can provide a guide for electrophysiological studies, allowing researchers to pick the brain areas with greatest interest, and target recordings to a small area.

CHAPTER V

RELAXIVITY OF PARAMAGNETIC METALS IN RAT BRAIN

5.1 Overview

In previous chapters, we focused on developments and applications of BOLD fMRI methodology that can achieve high spatial resolution at submillimeter scale without injection of contrast agent. However, in many cases, contrast agents are used in MRI to increase the disparity between different anatomical structures or to investigate a specific biological process. Paramagnetic ions and molecules are often used and may be highly effective contrast agents if they affect the relaxation times of water molecules in the tissues. As MR images are sensitive to the presence of paramagnetic ions, which increase the relaxation rates of tissue water protons, in principle, it can be assumed that measurements of tissue relaxation rates may be used to monitor tissue metal levels quantitatively.

In the following study, we focused on two paramagnetic ions-manganese and iron to study the influence of the co-existence of these two ions on the MR relaxivities. The reasons for us to study manganese and iron together are listed:

First, divalent manganese (Mn) and iron (Fe) ions (Mn^{2+} and Fe^{2+}), and trivalent Fe ion (Fe^{3+}), contain unpaired electrons and are both highly effective as paramagnetic relaxation agents capable of shortening both the T_1 and T_2 relaxation times of water molecules (Bloembergen et al., 1948; Fitsanakis et al., 2006a; Gore and Kennan, 1996; Kang et al., 1984; Silva et al., 2004).

Second, Mn and Fe are both essential metals for metabolism and biochemical functions in the central nervous system. Mn is an essential nutrient found in many foods, and is required for proper growth and development. It is an important component of many key enzymes involved in the detoxication of reactive oxygen species, amino acid synthesis and energy production (Erikson and Aschner, 2003; Fitsanakis and Aschner, 2005). Both deficiency and excess of this metal may result in health problems, although Mn toxicity is more common. Too little dietary Mn can lead to growth retardation, alterations in glucose and high-density lipid (HDL) cholesterol levels, and even reproductive failure (Greger, 1999). On the other hand, excess Mn can lead to the onset of a movement disorder, termed 'manganism', which is similar to Parkinson's disease. Fe is also involved in a variety of critical metabolic processes such as DNA synthesis, oxygen and electron transport, dopamine and serotonin synthesis, and myelin formation (Connor and Menzies, 1996; Lieu et al., 2001; Rouault, 2001). Furthermore, it has been suggested that brain Fe content is critical for normal development and behavior (Felt and Lozoff, 1996; Sipe et al., 2002). Increased total brain Fe content is associated with neurodegenerative disorders such as Alzheimer's and Parkinson's diseases (Sipe et al., 2002), while Fe deficiency can also lead to developmental and intellectual retardation (Pollitt and Leibel, 1976; Sipe et al., 2002).

Third, the precise mechanisms by which Mn and Fe are delivered into the brain, and how Mn and Fe affect each other's disposition, are not clear. Mn and Fe share similar transporter systems that allow the metals to enter cells (e.g. transferrin, divalent metal transporter-1) (Erikson et al., 2002). When the concentrations of the metals are high, there may be competition for the transporter or other targets between the ions so that

changes in one metal may influence the distribution of the other. For example, Zheng et al. found that brain Fe metabolism was changed in rats exposed to high doses of Mn. (Zheng et al., 1999). Fe deficiency leads to increased Mn accumulation in the brain (Chua and Morgan, 1996; Kwik-Uribe et al., 2000), while high Fe in the diet may decrease Mn absorption (Davis et al., 1992; Finley, 1999). There is also evidence that Mn and Fe may enter the brain through independent transport systems (Banks et al., 1988; Crowe and Morgan, 1992; Dickinson et al., 1996; Malecki et al., 1998, , 1999; Morris et al., 1992). It is well known that, in simple solutions, the water NMR relaxation rates (R1 and R2) are directly proportional to the concentration of paramagnetic ion. This simple linear relationship has been widely used to estimate tissue levels of Mn or Fe alone using MRI (Chaki et al., 2000; Dorman et al., 2006; Gallez et al., 2001; House et al., 2007; Kim et al., 1999). However, Mn and Fe are both paramagnetic, and they may compete or affect each other in biological systems. Thus the relationship between water relaxation rates and the concentrations of these paramagnetic ions together may not be as simple as assumed by the linear model. A more complex model may be needed to address the interaction between Mn and Fe binding and storage systems, and their combined effects on water relaxation times.

To address these questions, and to illustrate the need for more sophisticated analyses of imaging data, we studied the variations in MR relaxation rates as a function of metal content in groups of rats subjected to different combinations of dietary Fe and intravenous Mn. Our goal was to induce varying levels of both metals and to use quantitative MRI relaxometry to determine the Mn deposition pattern in different brain regions in rats exposed to this metal. In attempting to relate MR relaxation changes to

tissue metal levels, we have developed a model that incorporates competitive mechanisms between the metal ions. Such a model is essential to explain our relaxation measurements.

5.2 Materials and Methods

5.2.1 Animals

In order to achieve variable levels of Mn and Fe in tissues, adult male Sprague-Dawley rats were randomly separated into 4 groups; control (CN, n=5), Mn treated (MnT, n=6), Fe deficient and Mn treated (FeDMnT, n=6), Fe supplemented and Mn treated (FeSMnT, n=4) groups. MnT , FeDMnT, FeSMnT groups were given weekly intravenous (through tail vein) injections of a sterile isotonic Mn^{2+} solution ($MnCl_2$) equivalent to 3 mg Mn/kg body weight for a total of 14 weeks. This corresponds to doses of Mn comparable to those acquired by humans exhibiting symptoms of Mn intoxication (Mergler et al., 1999). CN and MnT were maintained on a normal diet (30 mg Fe/kg chow, BioServe, Frenchtown, NJ), while the FeDMnT and FeSMnT groups were given Fe deficient (3 mg Fe/kg feed; BioServe, Frenchtown, NJ) or Fe supplemented (300 mg Fe/kg feed; BioServe, Frenchtown, NJ) food, respectively. Food for all groups of rats has 12 mg Mn/kg chow. Fe in the Fe-supplemented diet (FeSMnT) was in the form of ferric citrate. Rats had free access to food and water throughout the study and were weighed weekly to monitor their general health. All procedures were in compliance with and approved by the Institutional Animal Care and Use Committee of Vanderbilt University.

5.2.2 MRI

Animals were scanned at the 14th week (24 hours after the last Mn injection). All experiments were acquired using a 4.7T, 31 cm bore Varian INOVA magnet with actively shielded gradients and a 63 mm transmit/receive quadrature imaging volume coil. Rat brains were scanned from both axial (FOV=40 X 40mm, 30 slices) and coronal (FOV=40 X 50mm, 20 slices) directions with 0.75mm slice thickness.

Before the imaging procedure, animals were first anesthetized with isoflurane (2%) and placed in a stereotaxic support cradle with the head secured. The cradle was then put in the volume coil to make sure the head of the animal was located at the center of the coil. Isoflurane was lowered to 1.5-1.75% and was maintained throughout the imaging experiment. Temperature (36.5-37.5^{o}C) of the animal was monitored (SA Instruments) and maintained via a flow of warm air which is controlled by a rectal temperature probe (SA Instrument). Respiration rate was externally monitored and maintained at 50-70 breaths per minute throughout the imaging session.

T_1 was measured using 2-D Fast Low Angle Shot sequences (FLASH) and different flip angles with parameters as follows: TR/TE=489/6.59 ms; flip angle=10, 30, 55, 70; 2 acquisitions. The image matrix was 256 X 256. T_2 was measured using a multislice fast spin echo (FSE) sequence: TR=5100 ms; Echo train length=8; k-space center=4; echo spacing=5, 6.7, 10, 13, 15 ms; 2 acquisitions; Image matrix=128 X 128;

T_1 and T_2 maps were calculated by fitting the series of T_1 and T_2 dependent images to the appropriate theoretical expressions using 2 parameter least squares fits. The parametric maps were then coregistered to a high resolution rat template and resliced using SPM (http://www.fil.ion.ucl.ac.uk/spm). Based on the rat brain template, multislice

regions of interest (ROIs) were chosen for seven brain regions including cerebellum, brain stem, midbrain, striatum, hippocampus and cortex. Averaged T_1 and T_2 values within each of the ROIs were calculated for each rat and used in further analyses.

Multiple $MnCl_2$ phantoms with similar T_1 and T_2 values as the rat brain tissues were also made (pH =7). Their T_1 and T_2 values were measured at 37^{o}C using an inversion recovery method and by changing TE in a spin echo sequence respectively.

5.2.3 Graphite Furnace Atomic Absorption Spectroscopy (GFAAS)

At the conclusion of the study, the animals were euthanized and their brains were removed, dissected (into cerebellum, brain stem, midbrain, striatum, hippocampus and cortex), weighed and quick frozen. Tissue Mn and Fe were measured in these regions with graphite furnace atomic absorption spectroscopy (Varian AA240, Varian, Inc USA). Brain regions were digested in ultrapure nitric acid (1:10 w/v dilution) for 48-72 hours in a sandbath (60° C). An aliquot of 100 µl of digested tissue was brought to 1 ml total volume with 2% nitric acid and analyzed for Mn and Fe. Both Mn and Fe GFAAS analyses were performed at the same time in the same sample. The standards used to standardize the GFAAS were purchased from Acros Organics, New Jersey: Mn (#19611-1000) and Fe (#19605-1000). Bovine Liver Standard (National Bureau of Standards, Washington, DC) was used as external standard in every analysis.

5.2.4 Statistical Analysis

Levene's homogeneity-of variance test was first applied to test if the variances are equal across groups ($p<0.05$). One-Way ANOVA was used to determine if differences

existed among the group means at an alpha level of 0.05. If significant difference were detected among the means, post-hoc range tests (Tukey HSD if variances are equal across groups, Dunnett T3 if variances are unequal across groups) were then applied to test the difference between each pair of means at an alpha level of 0.05. All statistical analyses were performed with SPSS software (SPSS Inc. Chicago, Illinois).

5.3 Results

5.3.1 Experimental Results

5.3.1.1 Ion Concentrations measured by GFAAS

Averaged metal concentrations at six brain regions which were measured by GFAAS at the 14th week for the four groups of rats are summarized in Table 9a (Mn concentration) and 9b (Fe concentration). For all four groups of rats, the smallest amount of Mn and Fe was found in cortex. In the CN and the MnT groups, the largest amount of Mn was found in hippocampus (0.184 ± 0.024 and 0.272 ± 0.039 mmol Mn/kg wet weight respectively), while in the FeDMnT and the FeSMnT groups, the largest amount of Mn was found in striatum (0.223 ± 0.066 and 0.289 ± 0.107 respectively). In the CN group, only midbrain, and hippocampus showed more than 0.1 mmol/kg wet weight of Mn (0.136 ± 0.054 and 0.184 ± 0.024 mmol Mn/kg wet weight respectively). In the MnT, the FeDMnT and the FeSMnT groups, almost all of the brain regions except cortex have around or over 0.1 mmol Mn/kg wet weight of Mn.

As shown in Table 9b, the largest amount of Fe was found in cerebellum in the CN (3.01 ± 1.33 mmol Fe/kg wet weight) and the MnT (2.65 ± 0.86 mmol Fe/kg wet

weight) groups, while it was found in hippocampus in the FeDMnT (2.22 ± 1.45mmol Fe/kg wet weight) and the FeSMnT (2.88 ± 1.44 mmol Fe/kg wet weight) groups. In the CN and the MnT groups, around or over 1.5 mmol/kg wet weight of Fe was found in all brain regions except cortex, while it was found only in hippocampus and straitum in the FeDMnT (2.22 ± 1.45 and 1.63 ± 0.63 mmol Fe/kg wet weight respectively) and the FeSMnT (2.88 ± 1.44 and 2.06 ± 0.80 mmol Fe/kg wet weight respectively) groups.

Table 9 Metal concentrations measured by GFAAS at the 14th week

a). Mn concentrations (10^{-2} mmol Mn/kg wet weight) measured by GFAAS at the 14th week.

	CN	**MnT**	**FeDMnT**	**FeSMnT**
CB	3.8±0.6[a, b, c]	9.9±1.9[a]	13.8±5.4[c]	13.5±2.8[b]
BS	5.7±1.3[a,b,c]	9.9±2.1[a, e]	17.3±7.1[c]	18.2±1.6[b, e]
MB	13.6±5.4	12.0±4.7	18.3±3.2	18.5±5.3
HP	18.4±2.4[a, c]	27.2±3.9[a,e, f]	11.9±1.4[c,f]	15.4±5.6[e]
ST	7.7±3.9[c]	13.0±4.9	22.3±6.6[c]	28.9±10.7
CX	1.9±0.7[b,c]	2.0±0.8[e, f]	4.9±0.5[c,f]	4.5±0.7[b,e]

b). Fe concentrations (mmol Fe/kg wet weight) measured by AAS at the 14th week.

	CN	MnT	FeDMnT	FeSMnT
CB	3.01±1.33[b,c]	2.65±0.86[e, f]	0.39±0.10[c, f]	0.33±0.05[b, e]
BS	2.25±0.97[c]	2.36±0.90[e, f]	0.87±0.63[c, f]	0.89±0.50[e]
MB	1.70±0.73	1.42±0.51	0.87±0.15	0.79±0.07
HP	2.19±1.40	2.57±1.01	2.22±1.45	2.88±1.44
ST	1.7±0.56	1.77±0.59	1.63±0.63	2.06±0.80
CX	0.64±0.52	0.66±0.36[e, f]	0.06±0.02[f]	0.10±0.05[e]

Note: CB-cerebellum, BS-brain stem, MB-midbrain, HP-hippocampus, ST-striatum, CX-cortex

The data represent mean values ± SD averaged across animals

a-f represents statistical difference at $p<0.05$.

a. CN vs. MnT; b CN vs. FeSMnT; c. CN vs. FeDMnT; d. FeSMnT vs. FeDMnT; e. MnT vs. FeSMnT; f. MnT vs. FeDMnT

One-Way ANOVA and post-hoc range tests were used to compare the Mn and Fe levels in each brain region across groups (see details in methods). Between the CN and the MnT groups, significant increases in Mn accumulation were observed in the MnT group in cerebellum ($p=0.034$), brain stem ($p=0.018$), and hippocampus ($p=0.003$); whereas striatum ($p=0.342$), midbrain ($p=0.935$) and cortical levels ($p=0.999$) did not change relative to control animals.

Mn concentrations were not significantly different between the FeDMnT and FeSMnT groups in any of the brain regions. Compared to the CN group, significant increases of Mn accumulation were observed in the FeDMnT and FeSMnT groups in cerebellum ($p=0.001$ and $p=0.002$ respectively), brainstem ($p=0.045$ and $p<0.0001$ respectively), and cortex ($p<0.0001$ and $p=0.001$ respectively). No significant differences of Mn accumulation were observed in midbrain for the FeDMnT ($p=0.36$) and FeSMnT ($p=0.42$) groups compared to the CN group. In hippocampus and striatum, no significant difference of Mn concentration was observed between the FeSMnT and control groups ($p=0.58$ and $p=0.092$ respectively). However the Mn concentration of the FeDMnT group in the hippocampus was significantly decreased compared to the control group ($p=0.03$), while a significant increase of Mn concentration was found for the FeDMnT group in striatum compared to the control group ($p=0.009$).

Compared to the MnT group, FeDMnT and FeSMnT groups showed significant differences of Mn concentration in hippocampus ($p<0.00001$ and $p<0.001$), and cortex ($p<0.00001$ and $p=0.001$, respectively). Decrease of Mn was observed in hippocampus while increase of Mn was found in other regions. No significant difference of Mn existed in striatum ($p=0.104$ and $p=0.198$), cerebellum ($p=0.218$ and $p=0.384$), and midbrain

(p=0.119 and p=0.168) for both the FeDMnT and FeSMnT groups compared to the MnT group. Significant Mn accumulation was also observed in brainstem of the FeSMnT group compared to the MnT group (p=0.001), but there was no significant difference between the FeDMnT and MnT groups (p=0.218). The results are summarized in Table 9a.

No significant change in Fe concentration was observed between the CN and MnT groups in any of the brain region (Table 9b), nor between the FeDMnT and FeSMnT groups. However, the Fe levels in the FeDMnT and FeSMnT groups were significantly decreased in cerebellum compared to CN (p=0.049 and p=0.045, respectively) and MnT (p=0.006 and p=0.006, respectively). No significant difference was found in cortex comparing FeDMnT and FeSMnT groups with CN group (p=0.245 and p=0.287, respectively), however decrease of Fe concentration was found in these two groups compared with MnT group (p=0.040 and p=0.049, respectively). In brainstem, significant decrease of Fe was found in FeDMnT group compared with both CN (p=0.043) and MnT (p=0.020) groups, and in FeSMnT group compared with MnT (p=0.043) group. The Fe amount in FeSMnT group was not significantly different from the CN (p=0.080) group in this brain region. No significant differences were found in FeDMnT and FeSMnT groups comparing CN and MnT groups in brain regions of midbrain, hippocampus and striatum. The results are summarized in Table 9b.

5.3.1.2 Relaxation Rates Measured by MRI

Typical axial and coronal T_1 weighted images of control and Mn-treated rats at week 14 are presented in Figure 33 (1st and 2nd columns of a and b). Pronounced signal increases are apparent in specific brain regions, such as the pontine nuclei (pons)

(Figure33a, green arrow), dentate gyrus (Figure33b, red arrow and circle) and habenula (Figure33a, black arrow). The contrast of T_1-weighted images was increased in brain regions, such as hippocampus (Figure33a, red arrow), cerebellum (CB) (Figure33b, 3rd row) and olfactory bulb (OB) (Figure33b, 4th row), allowing clear visualization of anatomic details of the brain neuroarchitecture. The CA3 layer of hippocampus, as well as layers of olfactory bulb was also clearly distinguishable in Mn treated rats due to the signal and contrast enhancement. Improved gray-white matter contrast was also apparent in the cerebellum. These increases in T_1 weighted signal and contrast were similar to those previously reported (Lee et al., 2005; Silva et al., 2004; Watanabe et al., 2004).

As seen in the T_1-weighted images (3rd and 4th columns of Figure33a and b), the signal and contrast enhancement effects in the FeDMnT and FeSMnT groups were similar to those shown in the MnT group. The FeDMnT and FeSMnT groups had higher Mn deposition in most brain regions so the MRI signal enhancement was likely due to Mn accumulation in the brain.

One-Way ANOVA and post-hoc range tests (see details above) were used to compare the difference of R_1 and R_2 values among the four groups in different brain regions. Average R_1 and R_2 values for the four groups and the results of the statistical tests are summarized in Table 10.

Compared to the CN group, significant increases of R_1 were observed in the MnT group in most brain regions (cerebellum $p=0.001$, midbrain $p<0.0001$, hippocampus $p<0.001$, striatum $p<0.00001$) except for brainstem ($p=0.153$) and cortex ($p=0.995$).

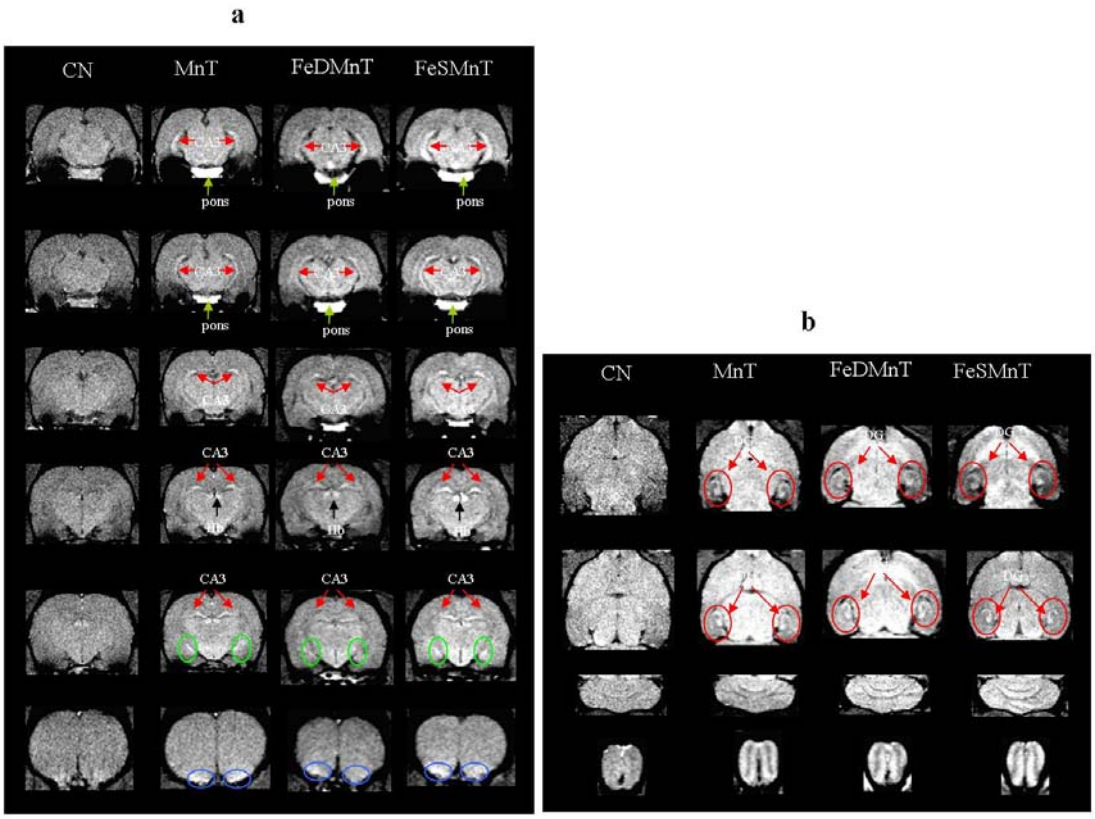

Figure 33 T1 weighted images for rats in CN (1st column in a and b), MnT (1nd column in a and b), FeDMnT (3rd column in a and b) and FeSMnT (4th column in a and b) groups at week 14 (TR=500 ms, flip angle=70). a) Transverse direction. b) Coronal direction. CB-cerebellum, BS-brain stem, MB-midbrain, HP-hippocampus, ST-striatum, CX-cortex.

No significant differences of R_1 values were observed between the FeDMnT and FeSMnT groups in any of the brain. However, R_1 values of the FeDMnT and FeSMnT groups were significantly larger than the values of CN and MnT groups (Table. 10a and 10b).

Significant differences of R_2 between the CN and MnT groups were observed only in striatum ($p=0.01$).

No significant differences of R_2 values were observed between the FeDMnT and FeSMnT groups in any of the brain except for hippocampus (p=0.03), while it approached significance in cerebellum (p=0.07). The FeSMnT group had an increase of R_2 values in these regions compared to the FeDMnT group.

Table 10 Relaxation rates measured by MRI at the 14th week

a) R_1 (10^{-1} s^{-1}) measured by MRI at the 14th week.

	CN	MnT	FeDMnT	FeSMnT
CB	7.06±0.35[a,b,c]	8.12±0.42[a,e,f]	8.96±0.36[c,f]	9.34±0.19[b,e]
BS	8.96±0.41[b,c]	9.57±0.40[e,f]	11.57±0.44[c,f]	11.85±0.55[b,e]
MB	7.48±0.28[a,b,c]	8.78±0.32[a,e,f]	10.49±0.24[c,f]	10.80±0.42[b,e]
HP	6.64±0.31[a,b,c]	7.29±0.11[a,e,f]	8.59±0.15[c,f]	8.77±0.23[b,e]
ST	7.14±0.33[a,b,c]	8.10±0.21[a,e,f]	9.36±0.13[c,f]	9.34±0.08[b,e]
CX	6.19±0.32[b,c]	6.25±0.23[e,f]	7.05±0.53[c,f]	6.99±0.41[b,e]

b). Transverse Relaxation R_2 (s^{-1}) measured by MRI at the 14th week.

	CN	MnT	FeDMnT	FeSMnT
CB	20.35±0.62[b]	20.58±0.29[e]	21.11±0.40	21.94±0.63[b,e]
BS	19.59±0.48[b,c]	20.24±0.62[f]	21.17±0.47[c,f]	20.88±0.46[b]
MB	19.43±0.73	19.51±1.11	19.48±0.96	20.72±0.68
HP	19.93±0.19	20.00±0.59	19.70±0.56[d]	20.69±0.52[d]
ST	19.85±0.07[a,b,c]	20.49±0.29[a,e]	21.19±0.57[c]	21.97±0.39[b,e]
CX	19.77±1.05	19.23±1.21[e]	19.97±0.46	21.35±0.40[e]

Note: CB-cerebellum, BS-brain stem, MB-midbrain, HP-hippocampus, ST-striatum, CX-cortex

The data represent mean values ± SD averaged across animals

a-f represents statistical difference at p<0.05.

a. CN vs. MnT; b CN vs. FeSMnT; c. CN vs. FeDMnT; d. FeSMnT vs. FeDMnT; e. MnT vs. FeSMnT; f. MnT vs. FeDMnT

Compared with the CN group, the FeDMnT group showed a significant increase of R_2 value only in striatum (p=0.009) and brainstem (p=0.001). No significant differences of R_2 values were observed between the FeDMnT group and the MnT group in any of the brain except for brainstem (p=0.037).

Significant increases of R_2 values were observed in the FeSMnT group compared with the CN group in brain regions including brainstem (p=0.008), striatum (p=0.005) and cerebellum (p=0.001). The increases of R_2 values in the FeSMnT group showed significance in cortex (p=0.008), striatum (p=0.006) and cerebellum (p=0.002) compared to the MnT group. Detailed experiment results have been reported by Fitsanakis et al. (Fitsanakis et al., 2006b).

5.3.2 Model Construction

The experimental results revealed that both Mn and Fe concentrations measured by GFAAS, as well as the R_1 and R_2 values, measured by MRI, varied across groups and across regions in a complicated way. Such effects imply that the relationship between relaxation rate and concentration may vary among tissues and complicate the use of relaxometry for estimating metal levels. We therefore evaluated two questions: a) What is the relationship between the Mn (and/or Fe) concentration and R_1 (and/or) R_2? b) Is MRI a reliable methodology to predict the metal concentrations in the brain? We used two different models to answer these questions.

5.3.2.1 Linear Model

In simple aqueous solutions a linear relationship exists between the concentration of a paramagnetic species and the relaxation rate R_1 ($1/T_1$) and R_2 ($1/T_2$):

$$R_{1,2}([Ion]) = R_{1,2}(0) + k_{1,2}[Ion] \quad (2)$$

Where $R_{1,2}([Ion])$ is the MRI measured relaxation rate at a given concentration of paramagnetic ion and $k_{1,2}$ is the so-called relaxivity. Taking Mn^{2+} as an example, $R_{1,2}(0)$ is the water proton relaxation rates without Mn^{2+}, and the constant $k_{1,2}$ can be determined by fitting experimental data to Eq. 2 (Kang et al., 1984; Nordhoy et al., 2004; Silva et al., 2004). Thus, tissues with higher concentrations of Mn should have shorter relaxation times and show higher signal intensity in T_1-weighted images, and lower signal intensity in T_2-weighted images. Note that the absolute quantification of Mn levels is not straightforward because the relaxivity *k* is not an intrinsic property of the metal ion alone. The relaxivity may change with the specific molecular form and environment in which the metal resides. For example, it may increase as a result of binding to intracellular ligands (Gore, 1985; Kang et al., 1984), or it may decrease if the metal's electron structure is altered or if water access to the metal is restricted, as occurs in many molecular configurations. Quantification of the ratio k_2/k_1 may also provide insights into the chemical form of the metal (Kang et al., 1984).

Control and Mn-Treated Groups

As shown in the experimental results, no difference in Fe concentrations existed between control and Mn-treated groups in any of the brain regions (Table 9b). For these two groups, we assumed that changes in Mn concentrations were the main contribution to the changes in the MR relaxation rates. Thus, the above linear model (Eq. 2) was first applied.

As illustrated in Figure 34, the relaxation rates in most tissues in these groups increased linearly with increased Mn levels. However, the slopes (the effective

relaxivities) varied in different regions and were all much smaller than the relaxivities of simple aqueous solutions. Midbrain and cortex showed negative k_1 and k_2 values respectively, which does not have any physical meaning, though the correlations between relaxation rate and concentration were not significant (Table 11a, 11b). In addition, the ratio of R_2 relaxivity (k_2) to R_1 relaxivity (k_1) also varied among tissues and it was less than the ratio of the aqueous solution in all brain regions (Table 11c.).

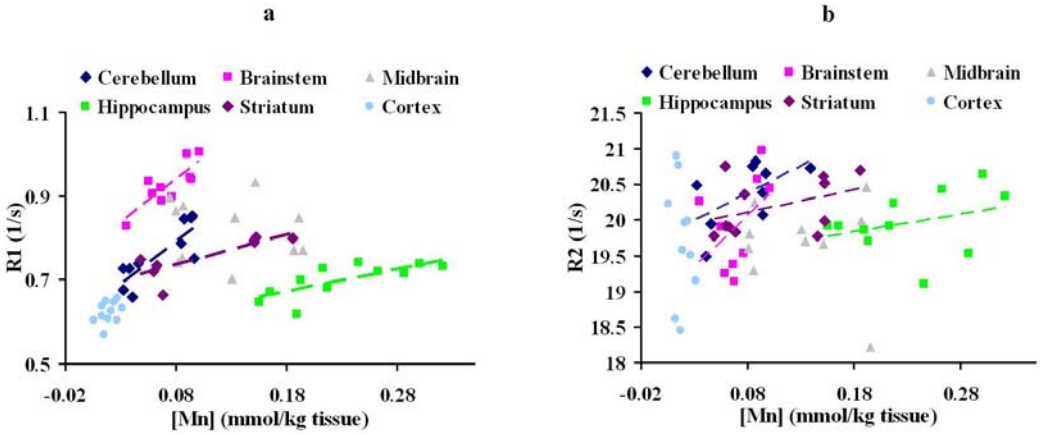

Figure 34 Relaxation rates vs. [Mn] for control and manganese treated groups. a) R1 vs. [Mn] b) R2 vs. [Mn].

The increases in relaxation rates were likely due to the deposition of Mn in the brain, though other contributions might be present, e.g. from associated changes in Fe. The observation that Mn relaxivity varied among regions suggests the metal exists in different forms, or is physically confined to different degrees in different areas. Conversion of Mn^{2+} to another oxidation state of the metal, the presence of different substrates for binding, the effects of competition from other metals, as well as the

variation in micro-viscosity, may all influence the relaxivity (Gore, 1985; Kang et al., 1984). Similarly, the k_2/k_1 ratio suggests there are differences in chemical form and binding effects. In hippocampus, the R_1 and R_2 relaxivity were both small, although the metal levels there were relatively high. This implies that the relaxation effect of the Mn as a paramagnetic ion is largely decreased, as would be expected if the Mn^{2+} metal is converted to a less paramagnetic state or if water access to the ion is restricted. These regional variations may be important for the interpretation of MR methods in use for tracking neural connectivity and for the use of MRI for monitoring metal deposition in tissues.

All Four Groups

When the dietary Fe was varied, the amount of both Mn and Fe in the brain changed, as shown in Table 9. The absolute levels of Fe did not necessarily agree with the expected amounts from dietary intake, but for our purposes we simply wanted to achieve varying levels of the metals. We tried to test the utility of the linear model in two ways. First, relaxation rates were plotted against Mn and Fe concentrations separately using Eq. 2. The results are summarized in Table 12. Second, we assumed that both Mn and Fe independently exist in the brain, so that the relaxation rates measured by MRI are just a linear combination of their contributions, as shown in Eq. 3 and Eq. 4. The least squares fitting method was applied to find the coefficients with the minimum residual. The results are summarized in Table 13.

$$R_1([Mn],[Fe]) = R_1(0) + k_{1,Mn}[Mn] + k_{1,Fe}[Fe] \quad (3)$$

$$R_2([Mn],[Fe]) = R_2(0) + k_{2,Mn}[Mn] + k_{2,Fe}[Fe] \quad (4)$$

Table 11 Relaxivities ($s^{-1}mM^{-1}$) for $MnCl_2$ phantoms and Mn in different brain regions.

a) k_1 value, standard error of k_1, significance of k_1 and r^2

	k_1	p	r^2
Phantom	8.39 ± 0.28	2.47E-10	0.99
CB	1.62 ± 0.39	0.003	0.69
BS	1.65 ± 0.4	0.003	0.68
MB	-0.14 ± 0.41	0.743	0.01
HP	0.42 ± 0.13	0.009	0.55
ST	0.58 ± 0.17	0.016	0.65
CX	1.08 ± 0.84	0.233	0.15

b) k_2 value, standard error of k_2, significance of k_2 and r^2

	k_2	p	r^2
Phantom	145.82 ± 3.88	3.35E-11	0.99
CB	6.11 ± 3.27	0.104	0.33
BS	11.56 ± 8.45	0.214	0.21
MB	2.67 ± 4.95	0.593	0.03
HP	1.98 ± 1.97	0.34	0.1
ST	2.48 ± 1.9	0.224	0.16
CX	-49.11 ± 35.69	0.202	0.17

c) Summarized k_1, k_2 and k_2/k_1

	Phantom	**CB**	**BS**	**MB**	**HP**	**ST**	**CX**
k_1	8.39	1.62	1.65	-0.14	0.42	0.58	1.08
k_2	145.82	6.11	11.56	2.67	1.98	2.48	-49.11
k_2/k_1	17.38	3.77	7.00	-19.07	4.71	4.28	-45.47

Note: CB-cerebellum, BS-brain stem, MB-midbrain, HP-hippocampus, ST-striatum, CX-cortex; The relaxivities of brain tissues are changed to units of ($s^{-1}mM^{-1}$) by assuming 80% water content in brain tissues. The data in a) and b) represent mean values ± standard error.

Table 12 Results of least squares fitting to equation 1.

a) k_1 of Mn (Mean ± Stderr), significance of $k_{1,Mn}$ and square of correlation coefficient

	$k_{1,Mn}$	p	r^2_{Mn}
CB	1.31 ± 0.29	2.15E-04	0.52
BS	1.66 ± 0.27	5.62E-06	0.67
MB	1.16 ± 0.54	4.59E-02	0.19
HP	-0.7 ± 0.25	1.22E-02	0.29
ST	0.65 ± 0.16	5.67E-04	0.47
CX	2.34 ± 0.60	1.12E-03	0.45

b) k_1 of Fe (Mean ± Stderr), significance of $k_{1,Fe}$ and square of correlation coefficient

	$k_{1,Fe}$	p	r^2_{Fe}
CB	-0.04 ± 0.01	3.95E-04	0.49
BS	-0.08 ± 0.02	4.00E-03	0.36
MB	-0.17 ± 0.04	4.45E-04	0.49
HP	-0.00 ± 0.02	9.81E-01	0.00
ST	0.00 ± 0.04	9.34E-01	0.00
CX	-0.06 ± 0.03	5.52E-02	0.19

c) k2 of Mn (Mean ± Stderr), significance of $k_{2,Mn}$ and square of correlation coefficient

	$k_{2,Mn}$	p	r^2_{Mn}
CB	8.10 ± 2.72	7.69E-03	0.32
BS	6.45 ± 2.31	1.17E-02	0.29
MB	7.65 ± 3.97	6.90E-02	0.16
HP	1.75 ± 1.88	3.65E-01	0.04
ST	6.64 ± 1.15	1.45E-05	0.64
CX	20.02 ± 15.62	2.16E-01	0.08

d) k2 of Fe (Mean ± Stderr), significance of $k_{2,Fe}$ and square of correlation coefficient

	$k_{2,Fe}$	p	r^2_{Fe}
CB	-0.29 ± 0.09	5.26E-03	0.34
BS	-0.55 ± 0.12	1.50E-04	0.55
MB	0.14 ± 0.39	7.21E-01	0.007
HP	-0.02 ± 0.12	8.60E-01	0.002
ST	0.28 ± 0.31	3.76E-01	0.042
CX	-1.31 ± 0.54	2.55E-02	0.26

Note: CB-cerebellum, BS-brain stem, MB-midbrain, HP-hippocampus, ST-striatum, CX-cortex, Unit of k_1 and k_2 is $[s*mmol/kg\ tissue]^{-1}$, p-significance of the the relaxivities

Table 13 Results of least squares fitting to equations 2 and 3

a) k_1 (Mean ± Stderr) , significances of k_1 and square of correlation coefficient

	$k_{1,Mn}$	$k_{1,Fe}$	p_{Mn}	p_{Fe}	r^2
CB	0.88 ± 0.30	-0.028 ± 0.010	8.38E-03	1.54E-02	0.66
BS	1.41 ± 0.23	-0.047 ± 0.015	9.82E-06	4.99E-03	0.79
MB	0.80 ± 0.42	-0.15 ± 0.038	7.07E-02	8.34E-04	0.57
HP	-0.71 ± 0.26	0.004 ± 0.015	1.42E-02	7.85E-01	0.29
ST	0.99 ± 0.14	-0.096 ± 0.024	1.86E-06	7.06E-04	0.73
CX	2.36 ± 0.82	0.001 ± 0.031	1.06E-02	9.63E-01	0.45

b) k_2 and square of correlation coefficient

	$k_{2,Mn}$	$k_{2,Fe}$	p_{Mn}	p_{Fe}	r^2
CB	5.02 ± 3.04	-0.20 ± 0.11	1.16E-01	7.75E-02	0.43
BS	3.94 ± 1.81	-0.48 ± 0.11	4.28E-02	6.28E-04	0.65
MB	8.38 ± 4.10	0.31 ± 0.37	5.57E-02	4.20E-01	0.19
HP	1.75 ± 1.94	-0.00 ± 0.11	3.79E-01	9.71E-01	0.04
ST	8.44 ± 1.24	-0.52 ± 0.20	2.23E-06	2.11E-02	0.73
CX	-4.49 ± 19.24	-1.42 ± 0.73	8.18E-01	6.86E-02	0.25

Notes: CB-cerebellum, BS-brain stem, MB-midbrain, HP-hippocampus, ST-striatum, CX-cortex; p-significance of the the relaxivities

As shown in Tables 12 and 13, the estimated apparent longitudinal relaxivities of Fe were negative for most of the brain regions, which had no clear physical interpretation. Most of these negative values are highly significant as the corresponding p (significance) values are much smaller than 0.05 (Table 12 and 13), indicating these negative values are mainly due to inappropriate application of the linear model and its incapacity to deal with simultaneous variations in two paramagnetic ions at the same time. The failure of the linear model and the results of GFAAS both suggested that Mn and Fe interact competitively and their combined influence on relaxation rates are more complicated.

5.3.2.2 Competition Model

We propose a new model (Figure 35 and Eqs. 5 to 13) to explain and interpret the combined influence of Mn and Fe on tissue relaxation rates. As illustrated in Figure 35, we assume Mn and Fe compete for a common specific binding site or a set of sites. We also assume that in a given brain region, Mn or Fe can either be bound to this common binding site (MnB or FeB) or be "else" (called MnE or FeE), as shown in Eqs. 5 and 6. Here, the 'else' ions include free ions and ions that bind to other substrates without competition. When either MnE or FeE successfully binds to a free common binding site (BS_{free}), they become MnB (1 Mn ion plus 1 common binding site) or FeB (1 Fe ion plus 1 common binding site), as shown in Eqs.8 and 9. In a steady state, chemical equilibrium will be achieved between free ions, bound ions and common binding sites (Eqs. 8 and 9). The two equilibrium constants $K_{eq,Mn}$ and $K_{eq,Fe}$ are used to describe the chemical equilibrium for Mn and Fe respectively (Eqs. 10 and 11). The total number of common binding sites (BS_{total}) is the summation of three parts: free binding sites (BS_{free}), sites that bound to Mn (as in MnB) and sites that bound to Fe (as in FeB), as shown in Eq.7. Mn_{total} and Fe_{total} are the total Mn and Fe metals contents measured by GFAAS. The longitudinal and transverse relaxation rates R_1 and R_2 are a linear combination of the effects of MnB, FeB, MnE, FeE as described by Eqs.12 and 13. The parameters in Eqs. 5 to 13 can be estimated by a least-squares method. First, a set of initial values are given, then the nonlinear equations are solved by the Levenberg-Marquardt method (Marquardt, 1963) using the initial values of parameters and the values of measured Mn and Fe concentrations for each individual rat. Next, $R_1(0)$ and relaxivities are fitted using the measured R_1 data according to Eq.12. The algorithm is a subspace trust region method

and is based on the interior-reflective Newton method described in (Coleman and Li, 1994). Once the convergence criteria are met and the eight parameters are updated, the above procedure is repeated until a local minimum of residual error is found. To search for the global minimum, a Monte Carlo simulation scheme is used to set initial values randomly. After the R_1 fitting procedure is finished and Eqs. 5 to 12 are solved, MnB, MnE, FeB and FeE concentrations are derived for each rat. Transverse relaxivities are then calculated using Eq.13. The reason for us to fit only equation 12 first rather than 13 is that the longitudinal relaxation rate correlates with Mn and Fe concentrations better than the transverse relaxation rate (Figure 34, Table 11-13). The fitting results are summarized in Table 14 and 15.

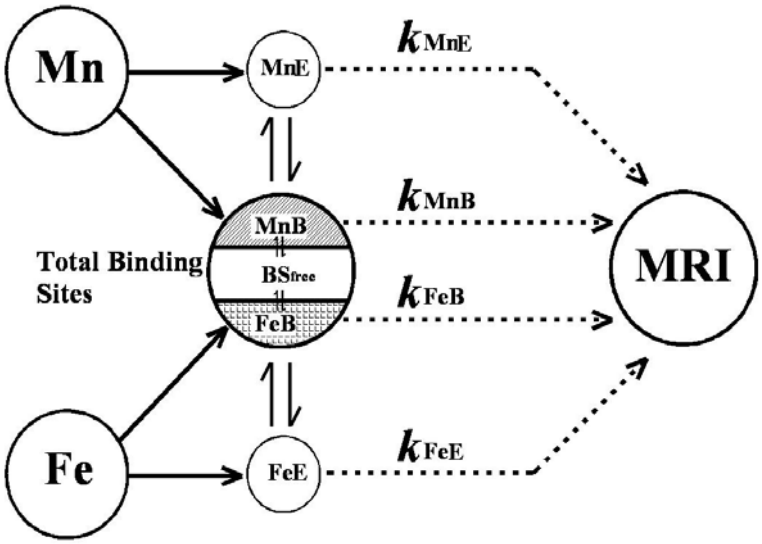

Figure 35 Principles of the competition model.

$$[Mn_{total}] = [MnB] + [MnE] \quad (5)$$

$$[Fe_{total}] = [FeB] + [FeE] \quad (6)$$

$$[BS_{total}] = [MnB] + [FeB] + [BS_{free}] \quad (7)$$

$$MnE + BS_{free} \xrightarrow{K_{eq,Mn}} MnB \quad (8)$$

$$FeE + BS_{free} \xrightarrow{K_{eq,Fe}} FeB \quad (9)$$

$$K_{eq,Mn} = \frac{[MnB]}{[MnE]*[BS_{free}]} \quad (10)$$

$$K_{eq,Fe} = \frac{[FeB]}{[FeE]*[BS_{free}]} \quad (11)$$

$$R_1([Mn]) = R_1(0) + k_{1,MnB}*[MnB] + k_{1,MnE}*[MnE] + k_{1,FeB}*[FeB] + k_{1,FeE}*[FeE] \quad (12)$$

$$R_2([Mn]) = R_2(0) + k_{2,MnB}*[MnB] + k_{2,MnE}*[MnE] + k_{2,FeB}*[FeB] + k_{2,FeE}*[FeE] \quad (13)$$

As shown in Table 14, the concentrations of total binding sites in brainstem and striatum were apparently much higher than the other regions. The common binding sites in hippocampus and cortex had higher binding affinity for Mn as $K_{eq,Mn}$ was much larger than $K_{eq,Fe}$, while the ones in cerebellum, brainstem and midbrain were more likely to bind with Fe. It seems that the increase in relaxation rates was mainly due to the bound Mn and bound Fe since the relaxivities of FeE and MnE were very small suggesting chemical modification or compartmentation. In most of the brain regions, Mn that was bound to the common binding site showed a larger relaxation effect than the bound Fe, as k_1 and k_2 of MnB were much larger than the ones of FeB. In striatum and brainstem, the longitudinal and transverse relaxivites of Fe (both FeB and FeE) were zero, suggesting

that Fe may have existed as a nonparamagnetic state or its paramagnetic character was largely diminished in these brain regions. The relaxivities of bound Fe in hippocampus were much larger than that in the other regions.

The concentrations of MnB, MnE, FeB and FeE were also derived for each rat and the averaged values for CN, MnT, FeSMnT and FeDMnT groups are summarized in Table 15. In cerebellum, most of the common binding sites were occupied by Fe in all four groups (CN, MnT, FeSMnT, FeDMnT). The ratio of [MnB]/[MnE] in control and MnT groups were much smaller than in the FeSMnT and FeDMnT groups, while the situation of [FeB]/[FeE] was reversed.

In brainstem, most of the common binding sites were taken by Fe in CN and MnT groups, while in FeSMnT and FeDMnT groups, FeB concentration was largely decreased and more free binding sites were released. MnB concentration was increased in FeSMnT and FeDMnT groups compared to CN and MnT groups.

In the midbrain, most of the common binding sites were occupied by both Mn and Fe. The amount of FeB and MnB was consistent among the four groups while the FeE concentration decreased more than 85% in FeSMnT and FeDMnT groups compared to CN and MnT groups.

The hippocampus was different from other regions as the ratio of [MnB]/[FeB] was around 1:1, and it was consistent for all groups. In addition, most of the Fe in hippocampus was not bound to the common binding sites.

The binding sites in striatum were mostly occupied by Fe and the amount of [FeB] remained consistent. The ratio of [MnB]/[MnE] in this brain region was around 2:1 and remained consistent among the four groups.

Table 14 Results of competition model.

a) Longitudinal relaxivities

	$k_{1,MnB}$ **	$k_{1,MnE}$ **	$k_{1,FeB}$ **	$k_{1,FeE}$ **
CB	1.74 ± 0.24	0.54 ± 0.3	0.01 ± 0.19	0 ± 0
BS	1.65 ± 0.2	0.34 ± 0.46	0 ± 0	0 ± 0
MB	2.75 ± 0.29	0 ± 0	0.36 ± 0.17	0 ± 0
HP	0.25 ± 0.32	0.01 ± 0.01	1.15 ± 0.33	0 ± 0
ST	1.92 ± 0.25	0 ± 0	0 ± 0	0 ± 0
CX	7.65 ± 1.16	0.01 ± 0.02	0.07 ± 0.03	0.06 ± 0.02

b) Transverse relaxivities

	$k_{2,MnB}$ **	$k_{2,MnE}$ **	$k_{2,FeB}$ **	$k_{2,FeE}$ **
CB	15.49 ± 2.41	0.75 ± 3	2.16 ± 1.92	0.05 ± 0.08
BS	7.01 ± 1.7	0 ± 0	0 ± 0	0 ± 0
MB	21.96 ± 3.57	3.37 ± 3.62	7.13 ± 2.1	0.86 ± 0.38
HP	3.57 ± 2.38	0 ± 0	1.16 ± 2.42	0 ± 0
ST	12.03 ± 2.4	3.83 ± 1.47	0 ± 0	0 ± 0
CX	63.52 ± 31.32	0 ± 0	0.01 ± 0.01	0 ± 0

c) k2/k1 ratio

	$k_{2,MnB}/k_{1,MnB}$	$k_{2,MnE}/k_{1,MnE}$	$k_{2,FeB}/k_{1,FeB}$	$k_{2,FeE}/k_{1,FeE}$
CB	8.92	1.39	215	N/A
BS	4.24	0	0	0
MB	7.98	N/A	19.95	N/A
HP	14.43	0.2	1	0
ST	6.28	N/A	0	0
CX	8.31	0	0.18	0

d) Constants in the models

	BStotal *	**Keq,Mn**	**Keq,Fe**	$R_1(0)$	$R_2(0)$
CB	0.42	259.3	683.2	0.72	19.33
BS	1.81	269.3	855.6	0.87	19.76
MB	0.97	106.2	1157.6	0.43	11.39
HP	0.38	3423.5	40.41	0.48	19.2
ST	1.58	65.12	125.1	0.65	19.29
CX	0.03	307.9	105.7	0.56	19.32

Table 14 Con

Notes: CB-cerebellum, BS-brain stem, MB-midbrain, HP-hippocampus, ST-striatum, CX-cortex; The data represent mean values ± standard error averaged across animals; *. Unit: [mmol/kg tissue]; **. Unit: $[s*mmol/kg\ tissue]^{-1}$; ***. Unit: 1/s

Most of Mn and Fe in cortex were not bound to the common binding sites. The FeE concentration was highly decreased in FeSMnT and FeDMnT groups compared to CN and MnT groups.

Figure 36 shows the fitting results of the interacting model. The measured and predicted relaxation rates in all brain regions were plotted against ion concentrations (Figure 36a-d). In addition, predicted relaxation rates in all brain regions were plotted against measured values (Figure 36e-f). The nonlinear relationships between relaxation rates and [Mn] as well as relaxation rates with [Fe] appear to be well explained by this model. Note that the transverse relaxation rate is less well fitted than the longitudinal relaxation rate (Figure 36e-f).

5.4 Discussion

5.4.1 Comparison of the competition model with the linear models

The fits to the data for the linear and competition models have been compared. The corresponding r^2, correlation coefficient, 95% confidence interval of the correlation coefficient as well as the p values are summarized in Table 16. Also, the regressions for all brain regions for all four models (competition model, linear model with both Mn and Fe considered, linear model with only Mn considered, linear model with only Fe

considered) are plotted in Figure 37. As illustrated in Figure 37a, the competition model and the linear model with Mn and Fe fitted together using Eq. 3 provided the best r^2 in all of the brain regions. In some brain regions the fits derived by these two models are significantly improved over the other two linear models in which only one ion is considered (Eq. 2). For example, for striatum the correlation coefficients derived by the competition and the linear models with both Mn and Fe considered are 0.87 and 0.85 respectively, while the values for the other two linear model with either Mn or Fe considered are 0.69 and 0.02 with 95% confidence interval of [0.36, 0.86] and [-0.42, 0.45] respectively. Other brain regions like brainstem and midbrain also provide evidence that the competition and the linear model taking account of both Mn and Fe provide better fitting results than one or both of the other two linear models. There is no significant difference between the correlation coefficients of the competition model and the linear model with both Mn and Fe counted. However, as shown above, the relaxivities of Fe fitted with the linear model are significantly negative in almost all of the brain regions (Table 13) which does not have any physical meaning. Thus, considering one metal alone at a time or both metals acting independently fails either to provide physically interpretable fits or to fit the data very successfully. Only by considering the competitive model are reasonable fits that have physical meanings obtained.

A diet with Fe overload is known to increase Fe accumulation in the plasma (Klevay, 2001). The increased brain Mn concentration accompanied by decreased brain Fe concentration with Fe supplemented in diet is surprising. This may be due to the fact that the added Mn that is on board in the FeSMnT group is more readily taken into the brain, offsetting the Fe overload in the diet.

Similar studies where rats were overloaded with dietary Fe for extended periods of time have been associated with approximately 10-fold increase in plasma Fe levels (Bacon et al., 1983; Dabbagh et al., 1994). It likely is associated with the inability of the regulatory machinery to accurately reflect the brain's Fe requirements due to transport and storage of Fe in ferritin. Normally, in the presence of exceedingly high levels of Fe, the regulatory pathway perceives the CNS as Fe deficient despite excessive Fe accumulation, and Fe uptake into the brain continues. When Fe regulatory protein-1 (IRP1) and IRP2 bind to the Fe regulatory element (IRE) in the 3′-untranslated region of transferrin receptor (TfR) or DMT1 mRNA, the transcript is stabilized, translation proceeds, and the proteins are synthesized. Thus, a high IRP binding activity reflects low body Fe stores and results in up-regulation of DMT1 and TfR. Vice versa, high intracellular Fe concentrations would have an opposite effect. Nonetheless, it is possible that the down-regulation of DMT1 and TfR is associated with up-regulation of transporters that are Mn-specific. Thus even in the presence of high Fe, the uptake of Mn may unabatedly continue. It has also been reported by Chua and Morgan that iron overload and deficiency led to increased brain Mn (Chua and Morgan, 1996).

Table 15 Averaged predicted MnB, MnE, FeB, FeE concentrations (10^{-1} mmol/kg tissue) for CN, MnT, FeSMnT and FeDMnT groups

a). Control group

	[MnB]	[MnE]	[FeB]	[FeE]	[BS_{free}]
CB	0.025 ± 0.004	0.35 ± 0.03	4.126 ± 0.005	25.94 ± 5.95	0.003 ± 0.001
BS	0.32 ± 0.07	0.25 ± 0.1	15.94 ± 1.25	6.6 ± 3.31	1.79 ± 1.19
MB	0.25 ± 0.12	1.1 ± 0.21	9.37 ± 0.12	7.63 ± 3.19	0.02 ± 0.01
HP	1.62 ± 0.07	0.22 ± 0.04	2.20 ± 0.07	24.33 ± 3.19	0.024 ± 0.004
ST	0.54 ± 0.02	0.23 ± 0.16	13.96 ± 0.53	3.13 ± 2.13	1.32 ± 0.54
CX	0.04 ± 0.01	0.15 ± 0.03	0.25 ± 0.02	6.16 ± 2.29	0.01 ± 0.004

b). MnT group

	[MnB]	[MnE]	[FeB]	[FeE]	[BS_{free}]
CB	0.067 ± 0.005	0.93 ± 0.08	4.083 ± 0.005	22.44 ± 3.52	0.003 ± 0
BS	0.54 ± 0.07	0.45 ± 0.15	16.95 ± 0.56	6.68 ± 3.36	0.56 ± 0.51
MB	0.3 ± 0.09	0.9 ± 0.17	9.3 ± 0.1	4.91 ± 1.98	0.05 ± 0.02
HP	2.3 ± 0.13	0.42 ± 0.06	1.53 ± 0.13	24.15 ± 4.05	0.017 ± 0.002
ST	0.82 ± 0.08	0.48 ± 0.15	13.31 ± 0.92	4.36 ± 1.57	1.69 ± 0.96
CX	0.03 ± 0.01	0.17 ± 0.03	0.26 ± 0.01	6.38 ± 1.44	0.005 ± 0.002

c). FeSMnT group

	[MnB]	[MnE]	[FeB]	[FeE]	[BS_{free}]
CB	1.02 ± 0.02	0.33 ± 0.13	2.92 ± 0.08	0.37 ± 0.15	0.22 ± 0.09
BS	1.8 ± 0.07	0.02 ± 0.01	8.82 ± 2.47	0.03 ± 0.02	7.43 ± 2.51
MB	1.39 ± 0.02	0.45 ± 0.28	7.63 ± 0.2	0.24 ± 0.16	0.62 ± 0.2
HP	1.34 ± 0.19	0.2 ± 0.1	2.47 ± 0.19	26.29 ± 7.3	0.03 ± 0.01
ST	1.45 ± 0.11	1.44 ± 0.55	12.97 ± 1.35	7.6 ± 2.73	1.39 ± 1.27
CX	0.16 ± 0.01	0.29 ± 0.02	0.11 ± 0.01	0.58 ± 0.02	0.018 ± 0.001

d) FeDMnT group

	[MnB]	[MnE]	[FeB]	[FeE]	[BS_{free}]
CB	0.87 ± 0.09	0.51 ± 0.2	3.1 ± 0.15	0.79 ± 0.28	0.18 ± 0.09
BS	1.59 ± 0.25	0.14 ± 0.13	8.23 ± 2.24	0.43 ± 0.42	8.23 ± 2.32
MB	1.11 ± 0.12	0.72 ± 0.25	8.03 ± 0.37	0.66 ± 0.26	0.52 ± 0.26
HP	1.10 ± 0.07	0.09 ± 0.02	2.69 ± 0.08	19.55 ± 5.85	0.05 ± 0.01
ST	1.45 ± 0.08	0.78 ± 0.22	12.38 ± 1.72	3.89 ± 1.04	1.99 ± 1.70
CX	0.18 ± 0.01	0.31 ± 0.02	0.10 ± 0.01	0.50 ± 0.07	0.019 ± 0.002

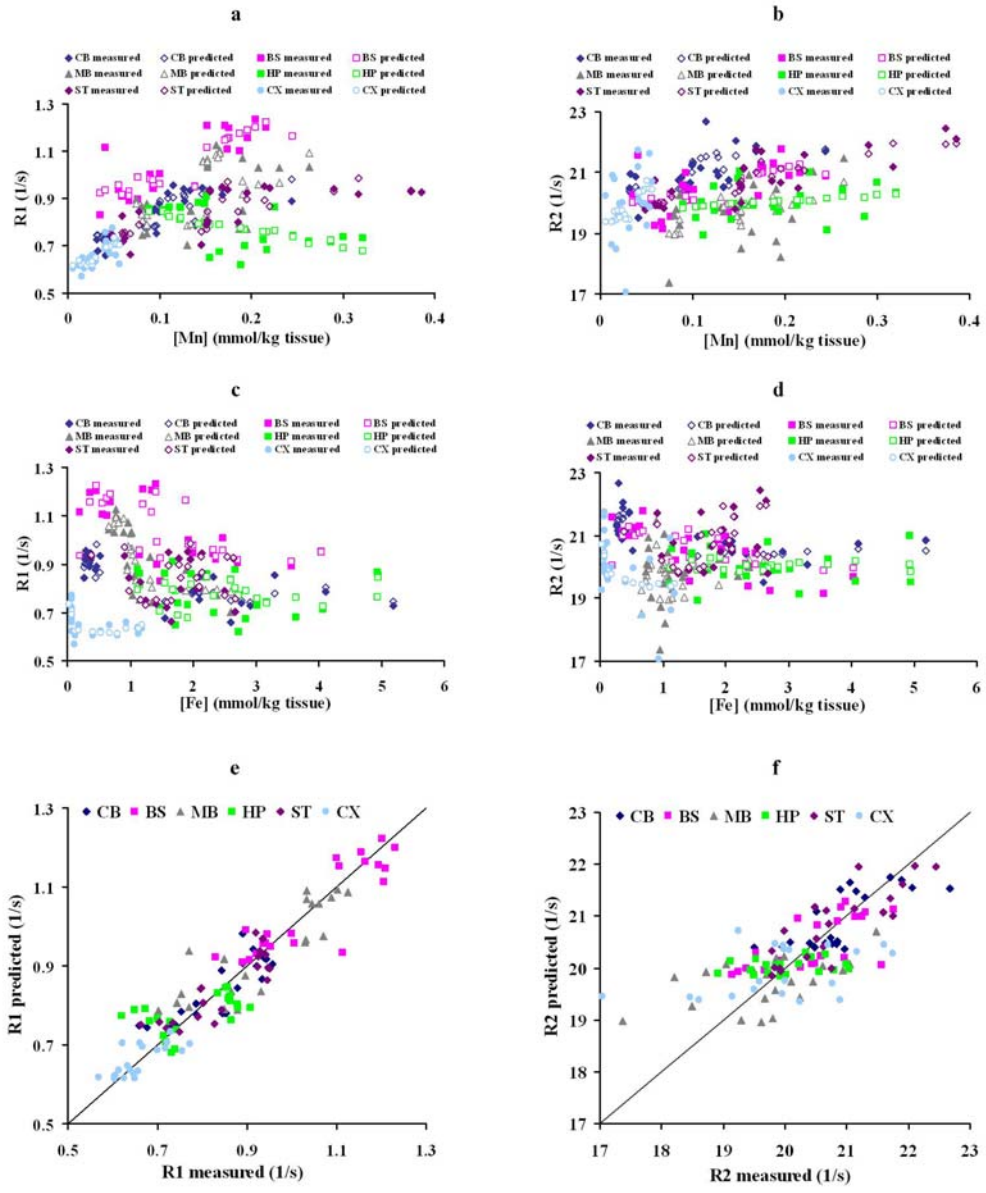

Figure 36 Fitting Results of the competition model. a) Measured and predicted R1 values vs. Mn concentration at six brain regions. Solid symbols for measured values, hollow symbols for predicted values. b) Measured and predicted R2 values vs. Mn concentration at six brain regions. Solid symbols for measured values, hollow symbols for predicted values. c) Measured and predicted R1 values vs. Fe concentration at six brain regions. Solid symbols for measured values, hollow symbols for predicted values. d) Measured and predicted R2 values vs. Fe concentration at six brain regions. Solid symbols for measured values, hollow symbols for predicted values. e) Predicted R1 values vs. measured R1 values at six brain regions. f) Predicted R2 values vs. measured R2 values at six brain regions. CB-cerebellum, BS-brain stem, MB-midbrain, HP-hippocampus, ST-striatum, CX-cortex.

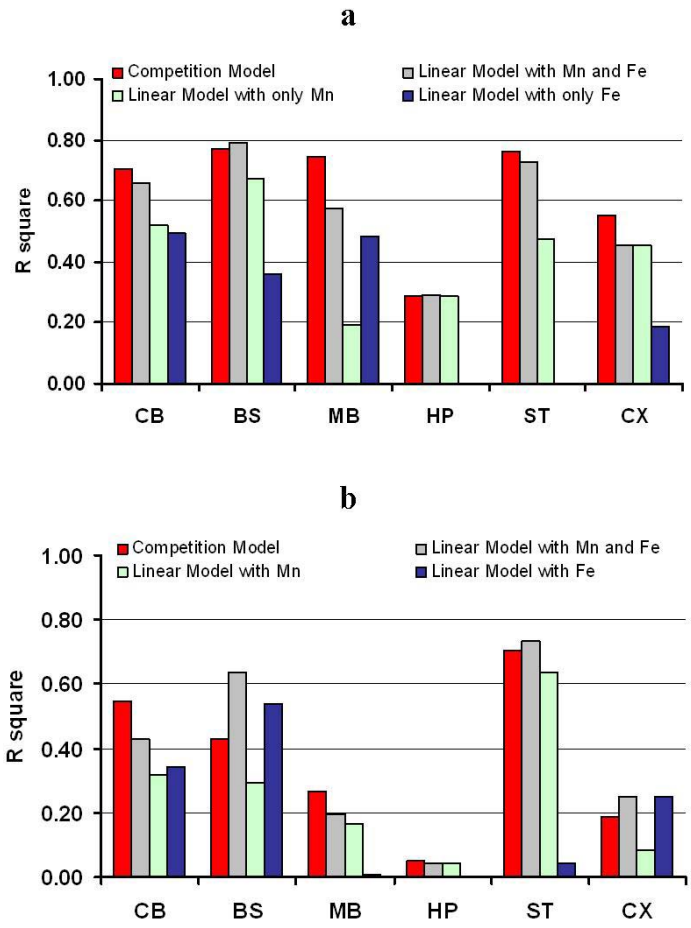

Figure 37 Square of the correlation coefficient between the measured relaxation rate and the predicted relaxation rate derived by competition and linear models. a) r2 of measured R1 vs. fitted R1 as results of using competition and linear models. b) r2 of measured R2 vs. fitted R2 as results of using competition and linear models. CB-cerebellum, BS-brain stem, MB-midbrain, HP-hippocampus, ST-striatum, CX-cortex.

5.4.2 Regional variation of the relaxivities and combined influence of Mn and Fe on MRI signal

The effects of Mn and Fe on MR relaxation rates have been studied before in isolation and without consideration of the potential interaction between the two (Dorman

et al., 2006; Gallez et al., 2001; House et al., 2007; Kim et al., 1999). Thus, when studies are designed to examine the effect of Mn on relaxivities, no other metal ions are usually considered. Conversely, other studies that focus solely on Fe have failed to take into account the interrelationship of this metal with Mn. As a result, most researchers have used a linear model to explain the influence of paramagnetic ions on the MRI signal. Our results show that when only one paramagnetic ion concentration change occurs, the simple linear model may appear to explain the relationship between ion concentration and relaxation rates. Thus the relaxation rate measured by MRI can be used as an indicator of ion concentration for this case. However, even with this simple linear model, the relaxivities vary among regions, implying that different brain regions should be treated separately rather than taking the whole brain as a single homogeneous region. To our knowledge, our study is the first one to examine the regional variation of the relaxivities.

Although Mn and Fe are commonly studied together in the toxicology field, no MRI study has been found in the literature that reports the combined influence of Mn and Fe on MRI signals. Our study is the first one to investigate this effect. Our results reveal that when more than one paramagnetic ion concentration is changing, the linear model does not describe the effects properly. As a result, a more complicated model must be applied. We propose an interacting model based on the fact that Mn and Fe may compete in vivo and both of them will affect MRI signals (Gore, 1985; Kang et al., 1984; Malecki et al., 1999). The regional variation effect is still very apparent in the interacting model.

Table 16 Comparison of the fitting results between the competition or linear models (correlation coefficient, 95% confidence interval of the correlation coefficient as well as the p values).

a) Fitting results of R1

1) Competition model

	CC	95% CI	p
CB	0.84	[0.64, 0.93]	1.96E-06
BS	0.88	[0.72, 0.95]	1.81E-07
MB	0.86	[0.69, 0.94]	5.06E-07
HP	0.54	[0.13, 0.79]	1.24E-02
ST	0.87	[0.71, 0.95]	2.49E-07
CX	0.74	[0.45, 0.89]	1.73E-04

2) Linear model with both Mn and Fe considered

	CC	95% CI	p
CB	0.81	[0.58, 0.92]	8.06E-06
BS	0.89	[0.74, 0.95]	7.29E-08
MB	0.76	[0.48, 0.90]	7.06E-05
HP	0.54	[0.14, 0.79]	1.17E-02
ST	0.85	[0.67, 0.94]	9.48E-07
CX	0.67	[0.33, 0.86]	1.12E-03

3) Linear model with only Mn considered

	CC	95% CI	p
CB	0.72	[0.42, 0.88]	2.15E-04
BS	0.82	[0.60, 0.92]	5.62E-06
MB	0.44	[0.01, 0.73]	4.59E-02
HP	0.54	[0.14, 0.79]	1.22E-02
ST	0.69	[0.36, 0.86]	5.67E-04
CX	0.67	[0.33, 0.86]	1.12E-03

4) Linear model with only Fe considered

	CC	95% CI	p
CB	0.7	[0.39, 0.87]	3.95E-04
BS	0.6	[0.23, 0.82]	4.00E-03
MB	0.7	[0.38, 0.87]	4.45E-04
HP	0.01	[-0.43, 0.44]	9.81E-01
ST	0.02	[-0.42, 0.45]	9.34E-01
CX	0.44	[-0.01, 0.74]	5.52E-02

b) Fitting results of R2

1) Competition model

	CC	95% CI	p
CB	0.74	[0.45, 0.89]	1.28E-04
BS	0.65	[0.31, 0.85]	1.28E-03
MB	0.52	[0.11, 0.78]	1.65E-02
HP	0.23	[-0.23, 0.60]	3.19E-01
ST	0.84	[0.64, 0.93]	2.07E-06
CX	0.43	[-0.01, 0.73]	5.78E-02

2) Linear model with both Mn and Fe considered

	CC	95% CI	p
CB	0.66	[0.31, 0.85]	1.26E-03
BS	0.8	[0.56, 0.91]	1.51E-05
MB	0.44	[0.01, 0.73]	4.56E-02
HP	0.21	[-0.24, 0.59]	3.59E-01
ST	0.86	[0.67, 0.94]	7.61E-07
CX	0.5	[0.07, 0.77]	2.47E-02

Table 16 Cont.

3) Linear model with only Mn considered

	CC	95% CI	p
CB	0.56	[0.18, 0.80]	7.69E-03
BS	0.54	[0.14, 0.79]	1.17E-02
MB	0.4	[-0.03, 0.71]	6.90E-02
HP	0.21	[-0.25, 0.59]	3.65E-01
ST	0.8	[0.56, 0.91]	1.45E-05
CX	0.29	[-0.18, 0.65]	2.16E-01

4) Linear model with only Fe considered

	CC	95% CI	p
CB	0.59	[0.21, 0.81]	5.26E-03
BS	0.73	[0.44, 0.89]	1.50E-04
MB	0.08	[-0.36, 0.50]	7.21E-01
HP	0.04	[-0.40, 0.46]	8.60E-01
ST	0.2	[-0.25, 0.58]	3.76E-01
CX	0.5	[0.07, 0.77]	2.55E-02

Notes: CB-cerebellum, BS-brain stem, MB-midbrain, HP-hippocampus, ST-striatum, CX-cortex

5.4.3 Application of Manganese as a contrast agent and paramagnetic tracer in neural imaging

Although this study focused on investigation of manganese and iron at the same time, the fact that, due to the deposition of manganese, pronounced signal increase and improved gray-white matter contrast are apparently observed in multiple brain regions in the T_1 weighted images of the three manganese treated groups (MnT, FeDMnT, FeSMnT) compared to the control group clearly indicate the application of manganese as contrast agent for our further neuroimaging studies.

In fact, numerous reports exist in the literature utilizing the paramagnetic quality of Mn as a contrast agent for neuronal mapping. Among them, Mn-enhanced MRI (MEMRI) has attracted growing attention both in MRI and neuroscience research. Extensive reviews of the most prominent applications of MEMRI in biological systems have been written by Silva and Koretsky (Koretsky and Silva, 2004; Silva et al., 2004). As they mention, there are three major applications of MEMRI in current research:

The first one uses Mn as a contrast agent to provide detailed visualization of the neural-architecture of the brain. Thus, researchers are now able to image intricate subtleties of cytoarchitecture of regions such as the neuronal cell layers in olfactory bulb, hippocampus, cerebellum, pituitary and cortex (Aoki et al., 2004; Lee et al., 2005; Watanabe et al., 2002).

The second class of MEMRI application involves tracing neuronal connections, as Mn^{2+} can be transported along neuronal pathways in an anterograde direction. This technique has been used with great success in mapping neuronal connection in the olfactory (Pautler and Koretsky, 2002; Pautler et al., 1998), somatosensory (Allegrini and Wiessner, 2003) and visual (Lin et al., 2001; Ryu et al., 2002; Watanabe et al., 2001) pathways of rodent brain, as well as the song centers of birds (Van der Linden et al., 2002), and neural connections in monkeys (Saleem et al., 2002).

The third application of MEMRI involves activity-induced Mn-enhanced MRI (AIM-MRI), a functional MRI technique to map tissue activation. It has been successfully used in both the brain (Aoki et al., 2002; Duong et al., 2000b; Lin and Koretsky, 1997) and heart (Brurok et al., 1999; Hu et al., 2001; Krombach et al., 2004; Wendland et al., 1999). Mn^{2+} can accumulate in cells via voltage-gated calcium transporters (Drapeau and Nachshen, 1984; Hunter et al., 1981; Narita et al., 1990), largely found in excitable cells. Thus, when the brain or heart is stimulated, local tissue activity is increased, leading to calcium influx and increased local concentration of Mn^{2+}, which will show enhanced MRI signal intensity at the activation areas. With the ability to separate the stimulation-specific signals from the non-stimulation-specific signals, this

technique will be very useful for functional MRI and pharmaceutical MRI studies (Aoki et al., 2002).

We hope, with our better understanding of the manganese transport and distribution mechanisms as well as our understanding of the effect of manganese on the MR signals, we can utilize this paramagnetic ion to facilitate our future fMRI studies to better understand brain activities and neuronal connections between brain regions.

5.5 Summary

It has been shown above, when Mn and Fe concentrations are both altered in a biological system, that their combined influence on MRI signals is complicated. In such a case, the simple linear model for explaining the relationship between MRI signal and a single changed paramagnetic ion will not be suitable to explain the change in MRI relaxation rates. Regional variations are apparent in both the experimental data and the model. Although some limitations and uncertainty exist in our model such as the presence of several free parameters in the fit, this represents a first attempt to explain the interacting relationship of two paramagnetic ions and their influence on the MRI signals. Our model correctly predicts the nonlinear relationship between relaxation rates and ion contents. This model may be useful for interpreting MR results when more than one paramagnetic species is involved.

CHAPTER VI

CONCLUSIONS AND FUTURE WORK

6.1 Conclusions

Since its discovery, BOLD fMRI has become one of the most powerful mapping techniques to study brain functional anatomy. However, the questions about the ultimate functional spatial specificity of the positive BOLD signal as a mapping tool, and the extent to which these activation maps correlate with underlying neuronal activities, as well as their equivalence to maps obtained by other high spatial resolution mapping techniques, such as optical imaging of intrinsic (OIS) and single unit electrophysiology, are still unsolved.

In chapter 2, we demonstrated that the positive BOLD signal at 9.4T can reveal the fine topography of individual fingerpads in single condition activation maps in non-human primates. These digit maps are similar to maps obtained from the same animal using intrinsic optical imaging. The finger topography obtained with BOLD fMRI proved to be highly reproducible across runs within a single session, across sessions, and across subjects. Furthermore, BOLD fMRI reliably resolved sub-millimeter spatial shifts in activation in area 3b previously identified with OIS (Chen et al., 2007) as neural correlates of the "funneling illusion". These data demonstrate that at high field, high spatial resolution topographic maps can be achieved using the positive BOLD signal, weakening previous notions regarding the spatial specificity of the positive BOLD signal,

suggesting that fMRI is an effective and appropriate tool for mapping the functional topography of brain areas not easily accessible using other methods.

Using the same technique, we further examined the characteristics of BOLD signal in the primary somatosensory cortex of the squirrel monkey (Chapter 3). We first investigated the dependence of the positive BOLD response on the intensity of single digit vibrotactile stimulation in two subregions of SI, areas 3b and 1. These studies revealed significant differences in BOLD response between these neighboring subregions of SI. In a region of interest (ROI) analysis of area 3b, the BOLD signal amplitude increased linearly with increasing amplitude of an 8Hz vibrotactile stimulus, and the BOLD signal was sustained throughout the stimulation period. In contrast, in area 1 a significant BOLD signal response was observed only with the more intense stimuli, and ROI analysis of the dependence of the BOLD response showed no significant dependence on stimulus intensity. Also, the activation was not sustained throughout the period of stimulation. The differing responses of area 3b and area 1 suggest potentially divergent roles for subregions of SI cortices in vibrotactile intensity encoding, and are consistent with area 3b playing a role in the earliest steps of cortical encoding of vibrotactile sensory stimuli.

Besides the positive BOLD signals in the primary somatosensory cortex, we have found consistent negative BOLD responses in areas adjacent to (about 3mm away from) the positive BOLD signals in area 3b. The negative BOLD signals correspond to two categories: sensory or sensorimotor areas. The negative signals are smaller in amplitude and return to baseline more rapidly than the adjacent positive BOLD signals at area 3b. The dependences of the negative BOLD responses in different areas on the stimulus

intensity were further investigated. In distinction to the positive BOLD signal at area 3b which varied linearly with stimulus intensity, the negative BOLD responses showed only weak or no correlation with the varying stimulus intensities we applied.

The very different BOLD responses found in the subregions of SI, such as positive BOLD in area 3b versus area 1, as well as the positive BOLD in area 3b versus negative BOLD in sensory / sensorimotor areas that are only a few millimeters apart, suggests the importance of high resolution fMRI acquisition, not only for mapping, but also for accurate studies of neurovascular coupling.

While primary somatosensory cortex (SI) has been extensively studied and fine somatotopic organization has been revealed in this area by multi-modalities, little information is known about secondary somatosensory cortex (SII). With the same approach which proved to be able to achieve submillimeter spatial resolution in SI, we investigated the somatotopic organization of digits in the secondary somatosensory cortex in chapter 4. Two distinct SII subregions (anterior and posterior) were revealed separated by 4.32 ± 1.96mm, with evidence of greater organizational fingerpad topography in posterior SII. Within each area, the somatosensory fingerpad topography (D1 to D4) was organized in a medial to lateral pattern. The topography of the fingerpads in SII was the mirror-image of those in areas 3b and 1. Finally, we found preliminary evidence of sensory funneling in SII as well as SI. The fingerpad topography in SII revealed by monkey fMRI can provide a guide for electrophysiological studies, allowing researchers to pick the brain areas with greatest interest, and target recordings to a small area.

Last, but not least, we investigated two paramagnetic ions (manganese and iron) to study the influence of the co-existence of these two ions on the MR signals (Chapter 5).

We found that, when Mn and Fe concentrations are both altered in a biological system, their combined influence on MRI signals is complicated. In such a case, the simple linear model commonly used in MRI history for explaining the relationship between MRI signal and a single paramagnetic ion species will not be suitable to explain the change in MRI relaxation rates. We proposed a complicated model to further explain the interacting relationship of two paramagnetic ions and their influence on the MRI signals. Our model correctly predicts the nonlinear relationship between relaxation rates and ion contents. This model may be useful for interpreting MR results when more than one paramagnetic species is involved. Our study is also the first one to examine the regional variation of the relaxivities.

Although our study mainly focused on studying two paramagnetic ions (manganese and iron) at the same time, it is obviously observed in our study that, due to the deposition of manganese, signal and gray-white matter contrast are apparently improved in multiple brain regions in the T_1 weighted images of the three manganese treated groups (MnT, FeDMnT, FeSMnT) compared to the control group. As manganese has been widely used as a paramagnetic contrast agent for neuronal mapping studies for neural-architecture visualization; neuronal connection tracing; and stimulation-specific activation detection, it clearly supports the application of manganese as contrast agent for our further neuroimaging studies. Detailed discussion for future research directions is shown in the following part (6.2).

In conclusion, our studies underscore the importance of imaging at high resolution. Such high resolution imaging allowed differentiation between the area-specific roles of subregions in somatosensory cortex and identified anatomic targets for detailed

electrophysiological studies of somatosensory neuronal populations with different coding properties. These experiments illustrate the value of the non-human primate for characterizing the nature of the BOLD activity and the dependence of the BOLD signal response on stimulus parameters, and on underlying neural response properties.

6.2 Future work

With the ability to measure neural activities and BOLD signals on the same animals, the future extension of our studies can contribute to solving the following issues:

1) What is the relationship between BOLD signals and the underlying local neuronal activities? Given a specific task / stimulation, how are the local neural activities translated into the measured BOLD activities?

2) What is the interaction between different brain regions and how is this interaction affecting local measured signals?

The goal of fMRI experiments is to study the neuronal activations in the brain while the subject is performing tasks or being stimulated. However, as BOLD signals are the combined effects of CBF, CMRO2 and CBV changes, the linkage between neuronal activity and the hemodynamic response is complex. A basic model of these couplings has been discussed in the literature (Buxton et al., 2004) and is shown in Figure 38. First, a task/stimulation s(t) will elicit local neuronal activity N(t), then the neuronal activity will induce the local CBF f(t) and $CMRO_2$ m(t) changes. The changes of CBF f(t) and $CMRO_2$ m(t) will in turn produce the CBV changes and total deoxyhemoglobin changes q(t). These changes may be related by biophysical models such as the Balloon model (Buxton et al., 1998) or Windkessel model (Mandeville et al., 1999). Finally the

combined CBV and total deoxyhemoglobin changes will induce BOLD signals measured by fMRI.

First, we start from the bottom of the diagram where the BOLD signals can be directly measured by fMRI. The measured BOLD signal is closely related to the normalized cerebral blood volume ($v=V/V_0$) and normalized total deoxyhemoglobin content ($q=Q/Q_0$) (Eq. 14):

$$\frac{\Delta S}{S} = V_0\left[k_1(1-q)+k_2(1-\frac{q}{v})+k_3(1-v)\right] \tag{14}$$

Where V_0 is the resting venous blood volume fraction and k1-k3 are dimensionless parameters which can be estimated based on several experimental and physiological parameters (Obata et al., 2004).

As stated above, the change in cerebral blood volume and total deoxyhemoglobin content are induced by changes in CBF and $CMRO_2$. The mechanism is usually explained by the Balloon model (Eq. 15-18)

$$\frac{dq}{dt} = \frac{1}{\tau_{MTT}}\left[f(t)\frac{E(t)}{E_0} - \frac{q(t)}{v(t)}f_{out}(v,t)\right] \tag{15}$$

$$\frac{dv}{dt} = \frac{1}{\tau_{MTT}}\left[f(t) - f_{out}(v,t)\right] \tag{16}$$

$$f_{out}(v) = v^{\frac{1}{\alpha}} + \tau\frac{dv}{dt} \tag{17}$$

$$v = f^{\alpha} \tag{18}$$

Where $E(t)$ is the net extraction fraction of oxygen with resting value (E_0) typically to be 0.4. $f E/E_0$ is the cerebral metabolic rate of oxygen ($CMRO_2$) normalized to its value at rest (m). τ_{MTT} is a constant representing the mean transit time through the balloon at rest.

τ is a viscoelastic time constant and α is the steady state flow-volume relation constant. With the driving function $f(t)E(t)$ and estimated values of the parameters (τ_{MTT}, τ, α and E_0), Eq 15-18 can be solved to yield dynamic time courses for q(t) and v(t) which can further be used to generate BOLD signal curves (Eq. 14).

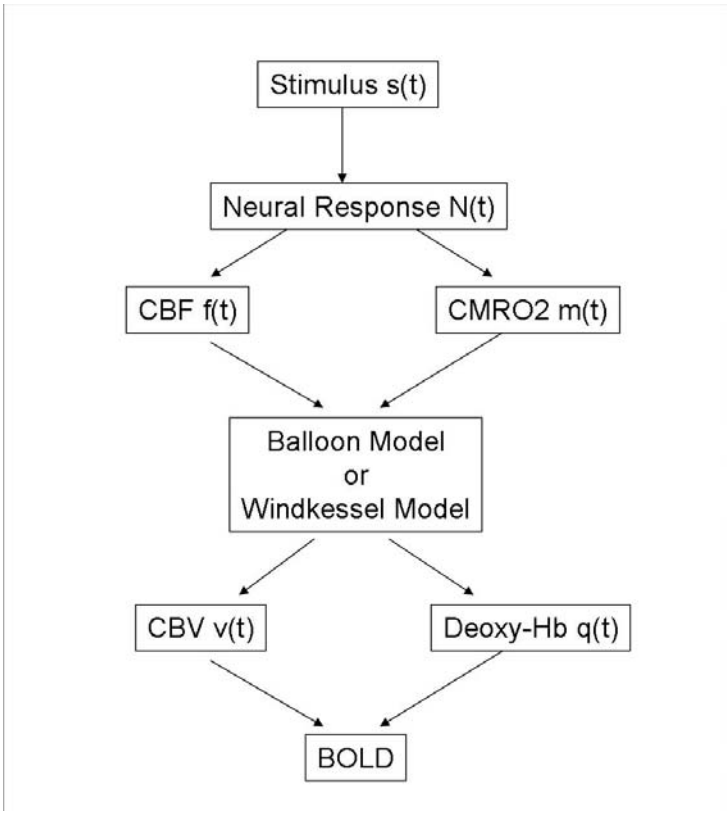

Figure 38 Workflow links the applied stimulus to the resulting physiological responses and the measured BOLD response.

The remaining two relationships in the diagram, the neurovascular coupling mechanism and how the neuronal activity quantitatively changes in response to the applied stimulus, are still open questions. However, with the ability to directly measure

neuronal activity (using electrophysiology) and vascular signals (e.g. using special MRI sequences such as FAIR or laser Doppler Flow techniqueto measure CBF; measuring CBV using monocrystalline iron oxide nanoparticles (MION) as MRI contrast agent; and estimating $CMRO_2$ using PET or MRS) together with smart experimental designs and experimental models, further useful information can be obtained from MRI to address these issues.

Another important issue is the study of brain networks and the cortical/subcortical connections between brain regions. This issue will be helpful to explain some of our current findings (e.g. area 3b and area 1 showed different BOLD characteristics responding to stimulus intensity change). Neuroanatomical cortical and subcortical connections have been examined using electrophysiological techniques as well as anterograde and retrograde tracer techniques (Disbrow et al., 2003; Felleman and Van Essen, 1991; Qi et al., 2002; Saint-Cyr et al., 1990). Figure 39 shows a summary of cortical connections of S2 and PV determined from electrophysiological studies (Disbrow et al., 2003).

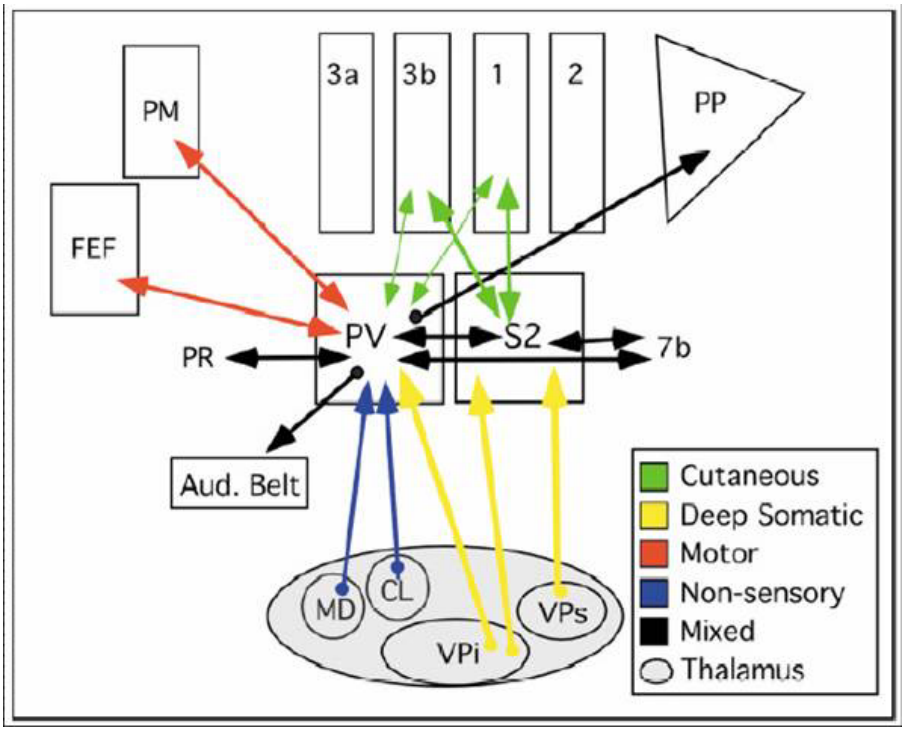

Figure 39 A summary of cortical connections of S2 and PV observed in electrophysiological studies. Adapted from Disbrow (2003). PV receives several different types of inputs from both the cortex and the thalamus. Inputs from deep receptors such as muscle spindles and Golgi tendon organs arise from the inferior and superior division of the ventral posterior nucleus (VPi and VPs, respectively; . PV also receives cutaneous inputs from cortical areas 3b and 1 and is interconnected with motor areas such as the frontal eye field and premotor cortex. Finally, PV has access to nonsensory inputs from the MD and CL of the thalamus. The connections of S2 from the thalamus are restricted to nuclei processing deep inputs and from cortical areas processing cutaneous inputs. Note that, rather than two separate "streams," somatosensory cortex appears to be organized into several overlapping networks.

Although these studies provide useful information about the connections between brain areas, the experimental procedures are invasive, and therefore do not allow longitudinal studies to be performed on a single animal for examination of the entire circuit or brain function through consecutive studies. A recent study using MRI used manganese (Mn^{2+}) to visualize neuronal pathways in the macaque monkey and clearly

demonstrated the potential of using MRI with the help of a contrast agent to study the neuronal connections in a non-invasive way (Saleem et al., 2002). In the study, researchers injected manganese chloride together with wheat germ agglutinin conjugated to horseradish peroxidase (WGA-HRP) into primate brain to evaluate the specificity of the manganese by tracing the neuronal connections of the basal ganglia of the monkey. Remarkably similar projection patterns were found with injection of $MnCl_2$ in the same animal at the same sites, indicating a high specific transport of the manganese as a paramagnetic tracer. It was also observed that manganese is sequentially transported from striatum to palidum-substantia nigra and then to thalamus, demonstrating that MRI can visualize transport across at least one synapse in the CNS of the primate. The characteristics of manganese make this paramagnetic ion highly feasible as a MRI neuronal tract-tracer. Such paramagnetic tracer MRI studies enable us to study the connectivity in the living animal. Also these studies will allow chronic studies of development and plasticity and provide important information for further electrophysiological experiments in the same animal.

Meanwhile, new computational techniques (ex. linear regression, multivariate autoregressive modeling and dynamic causal modeling) have recently been developed, providing tools to investigate brain "functional" and "effective connectivity". The functional connectivity has been defined as "temporal correlations between spatially remote neurophysiologic events" (Friston et al., 1993b), while "effective connectivity" is "the influence one neuronal system exerts over another" (Friston et al., 1993a). Functional activity has been used to characterize functional interactions (or correlations), while effective connectivity provides a direct insight into how these correlations are

mediated or integrated within a distributed system that is defined by functional connectivity. These modeling techniques have been successfully applied to address issues such as modulation of connectivity in the visual systems by object category and attention to motion. We expect these techniques will provide a way for us to more efficiently use BOLD signals to provide quantitative information regarding the functional connectivity between different brain areas (such as connectivity between subcortical areas of somatosensory cortex, ex. SI and SII, area 3b and area 1; and connectivity between different cortical systems, ex. somatosensory cortex and motor cortex). Implementation of these methods in non-human monkeys can now proceed, guided by the work described in this thesis.

REFERENCES

Adrian, E. D., 1941, Afferent discharges to the cerebral cortex from peripheral sense organs: J Physiol, v. 100, p. 159-91.

Allegrini, P. R., and C. Wiessner, 2003, Three-dimensional MRI of cerebral projections in rat brain in vivo after intracortical injection of MnCl2: NMR Biomed, v. 16, p. 252-6.

Allison, J. D., K. J. Meador, D. W. Loring, R. E. Figueroa, and J. C. Wright, 2000, Functional MRI cerebral activation and deactivation during finger movement: Neurology, v. 54, p. 135-42.

Anderson, A. W., R. Marois, E. R. Colson, B. S. Peterson, C. C. Duncan, R. A. Ehrenkranz, K. C. Schneider, J. C. Gore, and L. R. Ment, 2001, Neonatal auditory activation detected by functional magnetic resonance imaging: Magn Reson Imaging, v. 19, p. 1-5.

Aoki, I., C. Tanaka, T. Takegami, T. Ebisu, M. Umeda, M. Fukunaga, K. Fukuda, A. C. Silva, A. P. Koretsky, and S. Naruse, 2002, Dynamic activity-induced manganese-dependent contrast magnetic resonance imaging (DAIM MRI): Magn Reson Med, v. 48, p. 927-33.

Aoki, I., Y. J. Wu, A. C. Silva, R. M. Lynch, and A. P. Koretsky, 2004, In vivo detection of neuroarchitecture in the rodent brain using manganese-enhanced MRI: Neuroimage, v. 22, p. 1046-59.

Arthurs, O. J., and S. Boniface, 2002, How well do we understand the neural origins of the fMRI BOLD signal?: Trends Neurosci, v. 25, p. 27-31.

Arthurs, O. J., and S. J. Boniface, 2003, What aspect of the fMRI BOLD signal best reflects the underlying electrophysiology in human somatosensory cortex?: Clin Neurophysiol, v. 114, p. 1203-9.

Bacon, B. R., A. S. Tavill, G. M. Brittenham, C. H. Park, and R. O. Recknagel, 1983, Hepatic lipid peroxidation in vivo in rats with chronic iron overload: J Clin Invest, v. 71, p. 429-39.

Banks, W. A., A. J. Kastin, M. B. Fasold, C. M. Barrera, and G. Augereau, 1988, Studies of the slow bidirectional transport of iron and transferrin across the blood-brain barrier: Brain Res Bull, v. 21, p. 881-5.

Birn, R. M., and P. A. Bandettini, 2005, The effect of stimulus duty cycle and "off" duration on BOLD response linearity: Neuroimage, v. 27, p. 70-82.

Birn, R. M., Z. S. Saad, and P. A. Bandettini, 2001, Spatial heterogeneity of the nonlinear dynamics in the FMRI BOLD response: Neuroimage, v. 14, p. 817-26.

Bloembergen, N., E. M. Purcell, and R. V. Pound, 1948, Relaxation Effects in Nuclear Magnetic Resonance Absorption: Phys Rev, v. 73, p. 679-712.

Brinker, G., C. Bock, E. Busch, H. Krep, K. A. Hossmann, and M. Hoehn-Berlage, 1999, Simultaneous recording of evoked potentials and T2*-weighted MR images during somatosensory stimulation of rat: Magn Reson Med, v. 41, p. 469-73.

Brurok, H., T. Skoglund, K. Berg, S. Skarra, J. O. Karlsson, and P. Jynge, 1999, Myocardial manganese elevation and proton relaxivity enhancement with manganese dipyridoxyl diphosphate. Ex vivo assessments in normally perfused and ischemic guinea pig hearts: NMR Biomed, v. 12, p. 364-72.

Burton, H., M. Fabri, and K. Alloway, 1995, Cortical areas within the lateral sulcus connected to cutaneous representations in areas 3b and 1: a revised interpretation of the second somatosensory area in macaque monkeys: J Comp Neurol, v. 355, p. 539-62.

Buxton, R. B., K. Uludag, D. J. Dubowitz, and T. T. Liu, 2004, Modeling the hemodynamic response to brain activation: Neuroimage, v. 23 Suppl 1, p. S220-33.

Buxton, R. B., E. C. Wong, and L. R. Frank, 1998, Dynamics of blood flow and oxygenation changes during brain activation: the balloon model: Magn Reson Med, v. 39, p. 855-64.

Cannestra, A. F., N. Pouratian, S. Y. Bookheimer, N. A. Martin, D. P. Beckerand, and A. W. Toga, 2001, Temporal spatial differences observed by functional MRI and human intraoperative optical imaging: Cereb Cortex, v. 11, p. 773-82.

Cannestra, A. F., N. Pouratian, J. Forage, S. Y. Bookheimer, N. A. Martin, and A. W. Toga, 2004, Functional magnetic resonance imaging and optical imaging for dominant-hemisphere perisylvian arteriovenous malformations: Neurosurgery, v. 55, p. 804-12; discussion 812-4.

Carlson, M., M. F. Huerta, C. G. Cusick, and J. H. Kaas, 1986, Studies on the evolution of multiple somatosensory representations in primates: the organization of anterior parietal cortex in the New World Callitrichid, Saguinus: J Comp Neurol, v. 246, p. 409-26.

Chaki, H., S. Furuta, A. Matsuda, K. Yamauchi, K. Yamamoto, Y. Kokuba, and Y. Fujibayashi, 2000, Magnetic resonance image and blood manganese concentration as indices for manganese content in the brain of rats: Biol Trace Elem Res, v. 74, p. 245-57.

Chen, L. M., R. M. Friedman, B. M. Ramsden, R. H. LaMotte, and A. W. Roe, 2001, Fine-scale organization of SI (area 3b) in the squirrel monkey revealed with intrinsic optical imaging: J Neurophysiol, v. 86, p. 3011-29.

Chen, L. M., R. M. Friedman, and A. W. Roe, 2003, Optical imaging of a tactile illusion in area 3b of the primary somatosensory cortex: Science, v. 302, p. 881-5.

Chen, L. M., R. M. Friedman, and A. W. Roe, 2005, Optical imaging of SI topography in anesthetized and awake squirrel monkeys: J Neurosci, v. 25, p. 7648-59.

Chen, L. M., B. Heider, G. V. Williams, F. L. Healy, B. M. Ramsden, and A. W. Roe, 2002, A chamber and artificial dura method for long-term optical imaging in the monkey: J Neurosci Methods, v. 113, p. 41-9.

Chen, L. M., G. H. Turner, R. M. Friedman, N. Zhang, J. C. Gore, A. W. Roe, and M. J. Avison, 2007, High-resolution maps of real and illusory tactile activation in primary somatosensory cortex in individual monkeys with functional magnetic resonance imaging and optical imaging: J Neurosci, v. 27, p. 9181-91.

Cheng, H., G. Nair, T. A. Walker, M. K. Kim, M. T. Pardue, P. M. Thule, D. E. Olson, and T. Q. Duong, 2006, Structural and functional MRI reveals multiple retinal layers: Proc Natl Acad Sci U S A, v. 103, p. 17525-17530.

Cheng, K., R. A. Waggoner, and K. Tanaka, 2001, Human ocular dominance columns as revealed by high-field functional magnetic resonance imaging: Neuron, v. 32, p. 359-74.

Chua, A. C., and E. H. Morgan, 1996, Effects of iron deficiency and iron overload on manganese uptake and deposition in the brain and other organs of the rat: Biol Trace Elem Res, v. 55, p. 39-54.

Cohen, E. R., K. Ugurbil, and S. G. Kim, 2002, Effect of basal conditions on the magnitude and dynamics of the blood oxygenation level-dependent fMRI response: J Cereb Blood Flow Metab, v. 22, p. 1042-53.

Coleman, T. F., and Y. Li, 1994, On the Convergence of Reflective Newton Methods for Large-Scale Nonlinear Minimization Subject to Bounds: Mathematical Programming, v. 67, p. 189-224.

Connor, J. R., and S. L. Menzies, 1996, Relationship of iron to oligodendrocytes and myelination: Glia, v. 17, p. 83-93.

Coq, J. O., H. Qi, C. E. Collins, and J. H. Kaas, 2004, Anatomical and functional organization of somatosensory areas of the lateral fissure of the New World titi monkey (Callicebus moloch): J Comp Neurol, v. 476, p. 363-87.

Crowe, A., and E. H. Morgan, 1992, Iron and transferrin uptake by brain and cerebrospinal fluid in the rat: Brain Res, v. 592, p. 8-16.

Cusick, C. G., J. T. Wall, D. J. Felleman, and J. H. Kaas, 1989, Somatotopic organization of the lateral sulcus of owl monkeys: area 3b, S-II, and a ventral somatosensory area: J Comp Neurol, v. 282, p. 169-90.

Cusick, C. G., J. T. Wall, and J. H. Kaas, 1986, Representations of the face, teeth and oral cavity in areas 3b and 1 of somatosensory cortex in squirrel monkeys: Brain Res, v. 370, p. 359-64.

Dabbagh, A. J., T. Mannion, S. M. Lynch, and B. Frei, 1994, The effect of iron overload on rat plasma and liver oxidant status in vivo: Biochem J, v. 300 (Pt 3), p. 799-803.

Davis, C. D., T. L. Wolf, and J. L. Greger, 1992, Varying levels of manganese and iron affect absorption and gut endogenous losses of manganese by rats: J Nutr, v. 122, p. 1300-8.

Denys, K., W. Vanduffel, D. Fize, K. Nelissen, H. Sawamura, S. Georgieva, R. Vogels, D. Van Essen, and G. A. Orban, 2004, Visual activation in prefrontal cortex is stronger in monkeys than in humans: J Cogn Neurosci, v. 16, p. 1505-16.

Devor, A., A. K. Dunn, M. L. Andermann, I. Ulbert, D. A. Boas, and A. M. Dale, 2003, Coupling of total hemoglobin concentration, oxygenation, and neural activity in rat somatosensory cortex: Neuron, v. 39, p. 353-9.

Dickinson, T. K., A. G. Devenyi, and J. R. Connor, 1996, Distribution of injected iron 59 and manganese 54 in hypotransferrinemic mice: J Lab Clin Med, v. 128, p. 270-8.

Disbrow, E., E. Litinas, G. H. Recanzone, J. Padberg, and L. Krubitzer, 2003, Cortical connections of the second somatosensory area and the parietal ventral area in macaque monkeys: J Comp Neurol, v. 462, p. 382-99.

Disbrow, E. A., D. A. Slutsky, T. P. Roberts, and L. A. Krubitzer, 2000, Functional MRI at 1.5 tesla: a comparison of the blood oxygenation level-dependent signal and electrophysiology: Proc Natl Acad Sci U S A, v. 97, p. 9718-23.

Dorman, D. C., M. F. Struve, B. A. Wong, J. A. Dye, and I. D. Robertson, 2006, Correlation of brain magnetic resonance imaging changes with pallidal manganese concentrations in rhesus monkeys following subchronic manganese inhalation: Toxicol Sci, v. 92, p. 219-27.

Drapeau, P., and D. A. Nachshen, 1984, Manganese fluxes and manganese-dependent neurotransmitter release in presynaptic nerve endings isolated from rat brain: J Physiol, v. 348, p. 493-510.

Duong, T. Q., D. S. Kim, K. Ugurbil, and S. G. Kim, 2000a, Spatiotemporal dynamics of the BOLD fMRI signals: toward mapping submillimeter cortical columns using the early negative response: Magn Reson Med, v. 44, p. 231-42.

Duong, T. Q., D. S. Kim, K. Ugurbil, and S. G. Kim, 2001, Localized cerebral blood flow response at submillimeter columnar resolution: Proc Natl Acad Sci U S A, v. 98, p. 10904-9.

Duong, T. Q., A. C. Silva, S. P. Lee, and S. G. Kim, 2000b, Functional MRI of calcium-dependent synaptic activity: cross correlation with CBF and BOLD measurements: Magn Reson Med, v. 43, p. 383-92.

Erikson, K. M., and M. Aschner, 2003, Manganese neurotoxicity and glutamate-GABA interaction: Neurochem Int, v. 43, p. 475-80.

Erikson, K. M., Z. K. Shihabi, J. L. Aschner, and M. Aschner, 2002, Manganese accumulates in iron-deficient rat brain regions in a heterogeneous fashion and is associated with neurochemical alterations: Biol Trace Elem Res, v. 87, p. 143-56.

Felleman, D. J., and D. C. Van Essen, 1991, Distributed hierarchical processing in the primate cerebral cortex: Cereb Cortex, v. 1, p. 1-47.

Felt, B. T., and B. Lozoff, 1996, Brain iron and behavior of rats are not normalized by treatment of iron deficiency anemia during early development: J Nutr, v. 126, p. 693-701.

Ferretti, A., C. Babiloni, D. Arienzo, C. Del Gratta, P. M. Rossini, A. Tartaro, and G. L. Romani, 2006, Cortical brain responses during passive nonpainful median nerve stimulation at low frequencies (0.5-4 Hz): An fMRI study: Hum Brain Mapp, v. 28, p. 645-653.

Finley, J. W., 1999, Manganese absorption and retention by young women is associated with serum ferritin concentration: Am J Clin Nutr, v. 70, p. 37-43.

Fitsanakis, V. A., and M. Aschner, 2005, The importance of glutamate, glycine, and gamma-aminobutyric acid transport and regulation in manganese, mercury and lead neurotoxicity: Toxicol Appl Pharmacol, v. 204, p. 343-54.

Fitsanakis, V. A., N. Zhang, M. J. Avison, J. C. Gore, J. L. Aschner, and M. Aschner, 2006a, The use of magnetic resonance imaging (MRI) in the study of manganese neurotoxicity: Neurotoxicology, v. 27, p. 798-806.

Fitsanakis, V. A., N. Zhang, A. J. G., K. M. Erikson, J. C. Gore, and J. L. Aschner, 2006b, Determination of brain manganese and iron accumulation using magnetic resonance imaging (MRI) and atomic absorption spectroscopy: 42 nd Annual Society of Toxicology

Fransson, P., G. Kruger, K. D. Merboldt, and J. Frahm, 1999, MRI of functional deactivation: temporal and spatial characteristics of oxygenation-sensitive responses in human visual cortex: Neuroimage, v. 9, p. 611-8.

Friedman, D. P., E. G. Jones, and H. Burton, 1980, Representation pattern in the second somatic sensory area of the monkey cerebral cortex: J Comp Neurol, v. 192, p. 21-41.

Friston, K. J., 1998, Imaging neuroscience: principles or maps?: Proc Natl Acad Sci U S A, v. 95, p. 796-802.

Friston, K. J., C. D. Frith, and R. S. Frackowiak, 1993a, Time-dependent changes in effective connectivity measured with PET: Human Brain Mapping, v. 1, p. 69-79.

Friston, K. J., C. D. Frith, P. F. Liddle, and R. S. Frackowiak, 1993b, Functional connectivity: the principal-component analysis of large (PET) data sets: J Cereb Blood Flow Metab, v. 13, p. 5-14.

Frostig, R. D., E. E. Lieke, D. Y. Ts'o, and A. Grinvald, 1990, Cortical functional architecture and local coupling between neuronal activity and the microcirculation revealed by in vivo high-resolution optical imaging of intrinsic signals: Proc Natl Acad Sci U S A, v. 87, p. 6082-6.

Fukuda, M., C. H. Moon, P. Wang, and S. G. Kim, 2006, Mapping Iso-Orientation Columns by Contrast Agent-Enhanced Functional Magnetic Resonance Imaging: Reproducibility, Specificity, and Evaluation by Optical Imaging of Intrinsic Signal: J Neurosci, v. 26, p. 11821-11832.

Gallez, B., R. Demeure, C. Baudelet, N. Abdelouahab, N. Beghein, B. Jordan, M. Geurts, and H. A. Roels, 2001, Non invasive quantification of manganese deposits in the rat brain by local measurement of NMR proton T1 relaxation times: Neurotoxicology, v. 22, p. 387-92.

Gamlin, P. D., M. K. Ward, M. S. Bolding, J. K. Grossmann, and D. B. Twieg, 2006, Developing functional magnetic resonance imaging techniques for alert macaque monkeys: Methods, v. 38, p. 210-20.

Gardner, E. P., and W. A. Spencer, 1972, Sensory funneling. I. Psychophysical observations of human subjects and responses of cutaneous mechanoreceptive afferents in the cat to patterned skin stimuli: J Neurophysiol, v. 35, p. 925-53.

Gardner, E. P., and J. M. Tast, 1981, Psychophysical measurements of perceived intensity of single-point and multiple-point cutaneous stimuli in humans and subhuman primates: J Neurophysiol, v. 46, p. 479-95.

Garraghty, P. E., S. L. Florence, and J. H. Kaas, 1990, Ablations of areas 3a and 3b of monkey somatosensory cortex abolish cutaneous responsivity in area 1: Brain Res, v. 528, p. 165-9.

Gelnar, P. A., B. R. Krauss, N. M. Szeverenyi, and A. V. Apkarian, 1998, Fingertip representation in the human somatosensory cortex: an fMRI study: Neuroimage, v. 7, p. 261-83.

Glover, G. H., 1999, Deconvolution of impulse response in event-related BOLD fMRI: Neuroimage, v. 9, p. 416-29.

Gore, J. C., 1985, Physical factors in the design of contrast agents for MRI: IEEE Eng. in Med. and Biol., v. 4, p. 39-42.

Gore, J. C., and R. P. Kennan, 1996, Contrast Agents and Relaxation Effects, *in* S. W. Atlas, ed., Magnetic resonance imaging of the brain and spine: Philadelphia, Lippincott-Raven Press, p. 89-107.

Greger, J. L., 1999, Nutrition versus toxicology of manganese in humans: evaluation of potential biomarkers: Neurotoxicology, v. 20, p. 205-12.

Gretton, A., A. Belitski, Y. Murayama, B. Scholkopf, and N. Logothetis, 2006, The effect of artifacts on dependence measurement in fMRI: Magn Reson Imaging, v. 24, p. 401-9.

Grinvald, A., E. Lieke, R. D. Frostig, C. D. Gilbert, and T. N. Wiesel, 1986, Functional architecture of cortex revealed by optical imaging of intrinsic signals: Nature, v. 324, p. 361-4.

Hamzei, F., C. Dettmers, R. Rzanny, J. Liepert, C. Buchel, and C. Weiller, 2002, Reduction of excitability ("inhibition") in the ipsilateral primary motor cortex is mirrored by fMRI signal decreases: Neuroimage, v. 17, p. 490-6.

Harel, N., J. Lin, S. Moeller, K. Ugurbil, and E. Yacoub, 2006a, Combined imaging-histological study of cortical laminar specificity of fMRI signals: Neuroimage, v. 29, p. 879-87.

Harel, N., K. Ugurbil, K. Uludag, and E. Yacoub, 2006b, Frontiers of brain mapping using MRI: J Magn Reson Imaging, v. 23, p. 945-57.

Hashimoto, I., K. Yoshikawa, and T. Kimura, 1999, Sensory funneling of liminal multiple- point air-puff stimulation produces dramatic reduction in reaction time but relatively invariant P300 somatosensory evoked potential: Neuroreport, v. 10, p. 3201-5.

Hill, D. L., D. J. Hawkes, J. E. Crossman, M. J. Gleeson, T. C. Cox, E. E. Bracey, A. J. Strong, and P. Graves, 1991, Registration of MR and CT images for skull base surgery using point-like anatomical features: Br J Radiol, v. 64, p. 1030-5.

House, M. J., T. G. St Pierre, K. V. Kowdley, T. Montine, J. Connor, J. Beard, J. Berger, N. Siddaiah, E. Shankland, and L. W. Jin, 2007, Correlation of proton transverse relaxation rates (R2) with iron concentrations in postmortem brain tissue from alzheimer's disease patients: Magn Reson Med, v. 57, p. 172-80.

Hu, T. C., R. G. Pautler, G. A. MacGowan, and A. P. Koretsky, 2001, Manganese-enhanced MRI of mouse heart during changes in inotropy: Magn Reson Med, v. 46, p. 884-90.

Huang, W., I. Plyka, H. Li, E. M. Eisenstein, N. D. Volkow, and C. S. Springer, Jr., 1996, Magnetic resonance imaging (MRI) detection of the murine brain response to light: temporal differentiation and negative functional MRI changes: Proc Natl Acad Sci U S A, v. 93, p. 6037-42.

Hunter, D. R., R. A. Haworth, and H. A. Berkoff, 1981, Cellular manganese uptake by the isolated perfused rat heart: a probe for the sarcolemma calcium channel: J Mol Cell Cardiol, v. 13, p. 823-32.

Hyder, F., I. Kida, K. L. Behar, R. P. Kennan, P. K. Maciejewski, and D. L. Rothman, 2001, Quantitative functional imaging of the brain: towards mapping neuronal activity by BOLD fMRI: NMR Biomed, v. 14, p. 413-31.

Hyder, F., D. L. Rothman, and R. G. Shulman, 2002, Total neuroenergetics support localized brain activity: implications for the interpretation of fMRI: Proc Natl Acad Sci U S A, v. 99, p. 10771-6.

Inan, S., T. Mitchell, A. Song, J. Bizzell, and A. Belger, 2004, Hemodynamic correlates of stimulus repetition in the visual and auditory cortices: an fMRI study: Neuroimage, v. 21, p. 886-93.

Jones, E. G., and H. Burton, 1976, Areal differences in the laminar distribution of thalamic afferents in cortical fields of the insular, parietal and temporal regions of primates: J Comp Neurol, v. 168, p. 197-247.

Kaas, J. H., 1983, What, if anything, is SI? Organization of first somatosensory area of cortex: Physiol Rev, v. 63, p. 206-31.

Kaas, J. H., R. J. Nelson, M. Sur, C. S. Lin, and M. M. Merzenich, 1979, Multiple representations of the body within the primary somatosensory cortex of primates: Science, v. 204, p. 521-3.

Kalatsky, V. A., and M. P. Stryker, 2003, New paradigm for optical imaging: temporally encoded maps of intrinsic signal: Neuron, v. 38, p. 529-45.

Kang, Y. S., J. C. Gore, and I. M. Armitage, 1984, Studies of factors affecting the design of NMR contrast agents: manganese in blood as a model system: Magn Reson Med, v. 1, p. 396-409.

Kastrup, A., G. Kruger, T. Neumann-Haefelin, G. H. Glover, and M. E. Moseley, 2002, Changes of cerebral blood flow, oxygenation, and oxidative metabolism during graded motor activation: Neuroimage, v. 15, p. 74-82.

Kayser, C., M. Kim, K. Ugurbil, D. S. Kim, and P. Konig, 2004, A comparison of hemodynamic and neural responses in cat visual cortex using complex stimuli: Cereb Cortex, v. 14, p. 881-91.

Kim, D. S., T. Q. Duong, and S. G. Kim, 2000, High-resolution mapping of iso-orientation columns by fMRI: Nat Neurosci, v. 3, p. 164-9.

Kim, S. G., and T. Q. Duong, 2002, Mapping cortical columnar structures using fMRI: Physiol Behav, v. 77, p. 641-4.

Kim, S. G., and K. Ugurbil, 2003, High-resolution functional magnetic resonance imaging of the animal brain: Methods, v. 30, p. 28-41.

Kim, S. H., K. H. Chang, J. G. Chi, H. K. Cheong, J. Y. Kim, Y. M. Kim, and M. H. Han, 1999, Sequential change of MR signal intensity of the brain after manganese administration in rabbits. Correlation with manganese concentration and histopathologic findings: Invest Radiol, v. 34, p. 383-93.

Klevay, L. M., 2001, Iron overload can induce mild copper deficiency: J Trace Elem Med Biol, v. 14, p. 237-40.

Koretsky, A. P., and A. C. Silva, 2004, Manganese-enhanced magnetic resonance imaging (MEMRI): NMR Biomed, v. 17, p. 527-31.

Krause, T., R. Kurth, J. Ruben, J. Schwiemann, K. Villringer, M. Deuchert, M. Moosmann, S. Brandt, K. Wolf, G. Curio, and A. Villringer, 2001, Representational overlap of adjacent fingers in multiple areas of human primary somatosensory cortex depends on electrical stimulus intensity: an fMRI study: Brain Res, v. 899, p. 36-46.

Krombach, G. A., M. Saeed, C. B. Higgins, V. Novikov, and M. F. Wendland, 2004, Contrast-enhanced MR delineation of stunned myocardium with administration of MnCl(2) in rats: Radiology, v. 230, p. 183-90.

Krubitzer, L., J. Clarey, R. Tweedale, G. Elston, and M. Calford, 1995, A redefinition of somatosensory areas in the lateral sulcus of macaque monkeys: J Neurosci, v. 15, p. 3821-39.

Krubitzer, L. A., and J. H. Kaas, 1990, The organization and connections of somatosensory cortex in marmosets: J Neurosci, v. 10, p. 952-74.

Kwik-Uribe, C. L., D. Gietzen, J. B. German, M. S. Golub, and C. L. Keen, 2000, Chronic marginal iron intakes during early development in mice result in persistent changes in dopamine metabolism and myelin composition: J Nutr, v. 130, p. 2821-30.

Kwong, K. K., J. W. Belliveau, D. A. Chesler, I. E. Goldberg, R. M. Weisskoff, B. P. Poncelet, D. N. Kennedy, B. E. Hoppel, M. S. Cohen, R. Turner, and et al., 1992, Dynamic magnetic resonance imaging of human brain activity during primary sensory stimulation: Proc Natl Acad Sci U S A, v. 89, p. 5675-9.

Lee, J. H., A. C. Silva, H. Merkle, and A. P. Koretsky, 2005, Manganese-enhanced magnetic resonance imaging of mouse brain after systemic administration of MnCl2: dose-dependent and temporal evolution of T1 contrast: Magn Reson Med, v. 53, p. 640-8.

Lee, S. P., A. C. Silva, K. Ugurbil, and S. G. Kim, 1999, Diffusion-weighted spin-echo fMRI at 9.4 T: microvascular/tissue contribution to BOLD signal changes: Magn Reson Med, v. 42, p. 919-28.

Leite, F. P., D. Tsao, W. Vanduffel, D. Fize, Y. Sasaki, L. L. Wald, A. M. Dale, K. K. Kwong, G. A. Orban, B. R. Rosen, R. B. Tootell, and J. B. Mandeville, 2002, Repeated fMRI using iron oxide contrast agent in awake, behaving macaques at 3 Tesla: Neuroimage, v. 16, p. 283-94.

Li Hegner, Y., R. Saur, R. Veit, R. Butts, S. Leiberg, W. Grodd, and C. Braun, 2007, BOLD adaptation in vibrotactile stimulation: neuronal networks involved in frequency discrimination: J Neurophysiol, v. 97, p. 264-71.

Lieu, P. T., M. Heiskala, P. A. Peterson, and Y. Yang, 2001, The roles of iron in health and disease: Mol Aspects Med, v. 22, p. 1-87.

Lin, C. P., W. Y. Tseng, H. C. Cheng, and J. H. Chen, 2001, Validation of diffusion tensor magnetic resonance axonal fiber imaging with registered manganese-enhanced optic tracts: Neuroimage, v. 14, p. 1035-47.

Lin, Y. J., and A. P. Koretsky, 1997, Manganese ion enhances T1-weighted MRI during brain activation: an approach to direct imaging of brain function: Magn Reson Med, v. 38, p. 378-88.

Logothetis, N., H. Merkle, M. Augath, T. Trinath, and K. Ugurbil, 2002, Ultra high-resolution fMRI in monkeys with implanted RF coils: Neuron, v. 35, p. 227-42.

Logothetis, N. K., H. Guggenberger, S. Peled, and J. Pauls, 1999, Functional imaging of the monkey brain: Nat Neurosci, v. 2, p. 555-62.

Logothetis, N. K., J. Pauls, M. Augath, T. Trinath, and A. Oeltermann, 2001, Neurophysiological investigation of the basis of the fMRI signal: Nature, v. 412, p. 150-7.

Logothetis, N. K., and B. A. Wandell, 2004, Interpreting the BOLD signal: Annu Rev Physiol, v. 66, p. 735-69.

Lu, H., S. Patel, F. Luo, S. J. Li, C. J. Hillard, B. D. Ward, and J. S. Hyde, 2004, Spatial correlations of laminar BOLD and CBV responses to rat whisker stimulation with neuronal activity localized by Fos expression: Magn Reson Med, v. 52, p. 1060-8.

Malecki, E. A., A. G. Devenyi, J. L. Beard, and J. R. Connor, 1998, Transferrin response in normal and iron-deficient mice heterozygotic for hypotransferrinemia; effects on iron and manganese accumulation: Biometals, v. 11, p. 265-76.

Malecki, E. A., A. G. Devenyi, J. L. Beard, and J. R. Connor, 1999, Existing and emerging mechanisms for transport of iron and manganese to the brain: J Neurosci Res, v. 56, p. 113-22.

Malonek, D., and A. Grinvald, 1997, Vascular regulation at sub millimeter range. Sources of intrinsic signals for high resolution optical imaging: Adv Exp Med Biol, v. 413, p. 215-20.

Mandeville, J. B., J. J. Marota, C. Ayata, G. Zaharchuk, M. A. Moskowitz, B. R. Rosen, and R. M. Weisskoff, 1999, Evidence of a cerebrovascular postarteriole windkessel with delayed compliance: J Cereb Blood Flow Metab, v. 19, p. 679-89.

Manger, P. R., T. M. Woods, and E. G. Jones, 1995, Representation of the face and intraoral structures in area 3b of the squirrel monkey (Saimiri sciureus) somatosensory cortex, with special reference to the ipsilateral representation: J Comp Neurol, v. 362, p. 597-607.

Manger, P. R., T. M. Woods, and E. G. Jones, 1996, Representation of face and intra-oral structures in area 3b of macaque monkey somatosensory cortex: J Comp Neurol, v. 371, p. 513-21.

Marquardt, D., 1963, An Algorithm for Least-squares Estimation of Nonlinear Parameters: SIAM Journal Applied Mathematics, v. 11, p. 431-441.

Marshall, W. H., C. N. Woolsey, and P. Bard, 1937, Cortical Representation of Tactile Sensibility as Indicated by Cortical Potentials: Science, v. 85, p. 388-390.

Masamoto, K., T. Kim, M. Fukuda, P. Wang, and S. G. Kim, 2007, Relationship between Neural, Vascular, and BOLD Signals in Isoflurane-Anesthetized Rat Somatosensory Cortex: Cereb Cortex, v. 17, p. 942-50.

Mathiesen, C., K. Caesar, N. Akgoren, and M. Lauritzen, 1998, Modification of activity-dependent increases of cerebral blood flow by excitatory synaptic activity and spikes in rat cerebellar cortex: J Physiol, v. 512 (Pt 2), p. 555-66.

Mergler, D., M. Baldwin, S. Belanger, F. Larribe, A. Beuter, R. Bowler, M. Panisset, R. Edwards, A. de Geoffroy, M. P. Sassine, and K. Hudnell, 1999, Manganese neurotoxicity, a continuum of dysfunction: results from a community based study: Neurotoxicology, v. 20, p. 327-42.

Merzenich, M. M., J. H. Kaas, M. Sur, and C. S. Lin, 1978, Double representation of the body surface within cytoarchitectonic areas 3b and 1 in "SI" in the owl monkey (Aotus trivirgatus): J Comp Neurol, v. 181, p. 41-73.

Miller, K. L., W. M. Luh, T. T. Liu, A. Martinez, T. Obata, E. C. Wong, L. R. Frank, and R. B. Buxton, 2001, Nonlinear temporal dynamics of the cerebral blood flow response: Hum Brain Mapp, v. 13, p. 1-12.

Mohamed, F. B., A. B. Pinus, S. H. Faro, D. Patel, and J. I. Tracy, 2002, BOLD fMRI of the visual cortex: quantitative responses measured with a graded stimulus at 1.5 Tesla: J Magn Reson Imaging, v. 16, p. 128-36.

Morris, C. M., A. B. Keith, J. A. Edwardson, and R. G. Pullen, 1992, Uptake and distribution of iron and transferrin in the adult rat brain: J Neurochem, v. 59, p. 300-6.

Mukamel, R., H. Gelbard, A. Arieli, U. Hasson, I. Fried, and R. Malach, 2005, Coupling between neuronal firing, field potentials, and FMRI in human auditory cortex: Science, v. 309, p. 951-4.

Nagaoka, T., F. Zhao, P. Wang, N. Harel, R. P. Kennan, S. Ogawa, and S. G. Kim, 2006, Increases in oxygen consumption without cerebral blood volume change during visual stimulation under hypotension condition: J Cereb Blood Flow Metab, v. 26, p. 1043-51.

Narita, K., F. Kawasaki, and H. Kita, 1990, Mn and Mg influxes through Ca channels of motor nerve terminals are prevented by verapamil in frogs: Brain Res, v. 510, p. 289-95.

Nelken, I., J. K. Bizley, F. R. Nodal, B. Ahmed, J. W. Schnupp, and A. J. King, 2004, Large-scale organization of ferret auditory cortex revealed using continuous acquisition of intrinsic optical signals: J Neurophysiol, v. 92, p. 2574-88.

Nelson, R. J., M. Sur, D. J. Felleman, and J. H. Kaas, 1980, Representations of the body surface in postcentral parietal cortex of Macaca fascicularis: J Comp Neurol, v. 192, p. 611-43.

Nemoto, M., S. Sheth, M. Guiou, N. Pouratian, J. W. Chen, and A. W. Toga, 2004, Functional signal- and paradigm-dependent linear relationships between synaptic activity and hemodynamic responses in rat somatosensory cortex: J Neurosci, v. 24, p. 3850-61.

Niessing, J., B. Ebisch, K. E. Schmidt, M. Niessing, W. Singer, and R. A. Galuske, 2005, Hemodynamic signals correlate tightly with synchronized gamma oscillations: Science, v. 309, p. 948-51.

Nordhoy, W., H. W. Anthonsen, M. Bruvold, H. Brurok, S. Skarra, J. Krane, and P. Jynge, 2004, Intracellular manganese ions provide strong T1 relaxation in rat myocardium: Magn Reson Med, v. 52, p. 506-14.

Norris, D. G., 2006, Principles of magnetic resonance assessment of brain function: J Magn Reson Imaging, v. 23, p. 794-807.

Obata, T., T. T. Liu, K. L. Miller, W. M. Luh, E. C. Wong, L. R. Frank, and R. B. Buxton, 2004, Discrepancies between BOLD and flow dynamics in primary and supplementary motor areas: application of the balloon model to the interpretation of BOLD transients: Neuroimage, v. 21, p. 144-53.

Ogawa, S., T. M. Lee, and B. Barrere, 1993a, The sensitivity of magnetic resonance image signals of a rat brain to changes in the cerebral venous blood oxygenation: Magn Reson Med, v. 29, p. 205-10.

Ogawa, S., T. M. Lee, A. R. Kay, and D. W. Tank, 1990, Brain magnetic resonance imaging with contrast dependent on blood oxygenation: Proc Natl Acad Sci U S A, v. 87, p. 9868-72.

Ogawa, S., T. M. Lee, R. Stepnoski, W. Chen, X. H. Zhu, and K. Ugurbil, 2000, An approach to probe some neural systems interaction by functional MRI at neural time scale down to milliseconds: Proc Natl Acad Sci U S A, v. 97, p. 11026-31.

Ogawa, S., R. S. Menon, D. W. Tank, S. G. Kim, H. Merkle, J. M. Ellermann, and K. Ugurbil, 1993b, Functional brain mapping by blood oxygenation level-dependent contrast magnetic resonance imaging. A comparison of signal characteristics with a biophysical model: Biophys J, v. 64, p. 803-12.

Orban, G. A., D. Fize, H. Peuskens, K. Denys, K. Nelissen, S. Sunaert, J. Todd, and W. Vanduffel, 2003, Similarities and differences in motion processing between the human and macaque brain: evidence from fMRI: Neuropsychologia, v. 41, p. 1757-68.

Pauling, L., and C. D. Coryell, 1936, The Magnetic Properties and Structure of Hemoglobin, Oxyhemoglobin and Carbonmonoxyhemoglobin: Proc Natl Acad Sci U S A, v. 22, p. 210-6.

Pautler, R. G., and A. P. Koretsky, 2002, Tracing odor-induced activation in the olfactory bulbs of mice using manganese-enhanced magnetic resonance imaging: Neuroimage, v. 16, p. 441-8.

Pautler, R. G., A. C. Silva, and A. P. Koretsky, 1998, In vivo neuronal tract tracing using manganese-enhanced magnetic resonance imaging: Magn Reson Med, v. 40, p. 740-8.

Pollitt, E., and R. L. Leibel, 1976, Iron deficiency and behavior: J Pediatr, v. 88, p. 372-81.

Pons, T. P., P. E. Garraghty, C. G. Cusick, and J. H. Kaas, 1985, The somatotopic organization of area 2 in macaque monkeys: J Comp Neurol, v. 241, p. 445-66.

Pouratian, N., A. F. Cannestra, N. A. Martin, and A. W. Toga, 2002a, Intraoperative optical intrinsic signal imaging: a clinical tool for functional brain mapping: Neurosurg Focus, v. 13, p. e1.

Pouratian, N., N. Sicotte, D. Rex, N. A. Martin, D. Becker, A. F. Cannestra, and A. W. Toga, 2002b, Spatial/temporal correlation of BOLD and optical intrinsic signals in humans: Magn Reson Med, v. 47, p. 766-76.

Qi, H. X., D. C. Lyon, and J. H. Kaas, 2002, Cortical and thalamic connections of the parietal ventral somatosensory area in marmoset monkeys (Callithrix jacchus): J Comp Neurol, v. 443, p. 168-82.

Rainer, G., M. Augath, T. Trinath, and N. K. Logothetis, 2001, Nonmonotonic noise tuning of BOLD fMRI signal to natural images in the visual cortex of the anesthetized monkey: Curr Biol, v. 11, p. 846-54.

Rauch, S. L., P. J. Whalen, T. Curran, S. McInerney, S. Heckers, and C. R. Savage, 1998, Thalamic deactivation during early implicit sequence learning: a functional MRI study: Neuroreport, v. 9, p. 865-70.

Rees, G., K. Friston, and C. Koch, 2000, A direct quantitative relationship between the functional properties of human and macaque V5: Nat Neurosci, v. 3, p. 716-23.

Robinson, C. J., and H. Burton, 1980a, Organization of somatosensory receptive fields in cortical areas 7b, retroinsula, postauditory and granular insula of M. fascicularis: J Comp Neurol, v. 192, p. 69-92.

Robinson, C. J., and H. Burton, 1980b, Somatic submodality distribution within the second somatosensory (SII), 7b, retroinsular, postauditory, and granular insular cortical areas of M. fascicularis: J Comp Neurol, v. 192, p. 93-108.

Robinson, C. J., and H. Burton, 1980c, Somatotopographic organization in the second somatosensory area of M. fascicularis: J Comp Neurol, v. 192, p. 43-67.

Robson, M. D., J. L. Dorosz, and J. C. Gore, 1998, Measurements of the temporal fMRI response of the human auditory cortex to trains of tones: Neuroimage, v. 7, p. 185-98.

Rouault, T. A., 2001, Systemic iron metabolism: a review and implications for brain iron metabolism: Pediatr Neurol, v. 25, p. 130-7.

Ruben, J., J. Schwiemann, M. Deuchert, R. Meyer, T. Krause, G. Curio, K. Villringer, R. Kurth, and A. Villringer, 2001, Somatotopic organization of human secondary somatosensory cortex: Cereb Cortex, v. 11, p. 463-73.

Ryu, S., S. L. Brown, A. Kolozsvary, J. R. Ewing, and J. H. Kim, 2002, Noninvasive detection of radiation-induced optic neuropathy by manganese-enhanced MRI: Radiat Res, v. 157, p. 500-5.

Saint-Cyr, J. A., L. G. Ungerleider, and R. Desimone, 1990, Organization of visual cortical inputs to the striatum and subsequent outputs to the pallido-nigral complex in the monkey: J Comp Neurol, v. 298, p. 129-56.

Saleem, K. S., J. M. Pauls, M. Augath, T. Trinath, B. A. Prause, T. Hashikawa, and N. K. Logothetis, 2002, Magnetic resonance imaging of neuronal connections in the macaque monkey: Neuron, v. 34, p. 685-700.

Sato, K., T. Nariai, S. Sasaki, I. Yazawa, H. Mochida, N. Miyakawa, Y. Momose-Sato, K. Kamino, Y. Ohta, K. Hirakawa, and K. Ohno, 2002, Intraoperative intrinsic optical imaging of neuronal activity from subdivisions of the human primary somatosensory cortex: Cereb Cortex, v. 12, p. 269-80.

Sawamura, H., G. A. Orban, and R. Vogels, 2006, Selectivity of neuronal adaptation does not match response selectivity: a single-cell study of the FMRI adaptation paradigm: Neuron, v. 49, p. 307-18.

Schwartz, T. H., 2005, The application of optical recording of intrinsic signals to simultaneously acquire functional, pathological and localizing information and its potential role in neurosurgery: Stereotact Funct Neurosurg, v. 83, p. 36-44.

Sheth, S., M. Nemoto, M. Guiou, M. Walker, N. Pouratian, and A. W. Toga, 2003, Evaluation of coupling between optical intrinsic signals and neuronal activity in rat somatosensory cortex: Neuroimage, v. 19, p. 884-94.

Sheth, S. A., M. Nemoto, M. Guiou, M. Walker, N. Pouratian, N. Hageman, and A. W. Toga, 2004, Columnar specificity of microvascular oxygenation and volume responses: implications for functional brain mapping: J Neurosci, v. 24, p. 634-41.

Shmuel, A., M. Augath, A. Oeltermann, and N. K. Logothetis, 2006, Negative functional MRI response correlates with decreases in neuronal activity in monkey visual area V1: Nat Neurosci, v. 9, p. 569-77.

Shmuel, A., E. Yacoub, J. Pfeuffer, P. F. Van de Moortele, G. Adriany, X. Hu, and K. Ugurbil, 2002, Sustained negative BOLD, blood flow and oxygen consumption response and its coupling to the positive response in the human brain: Neuron, v. 36, p. 1195-210.

Silva, A. C., and A. P. Koretsky, 2002, Laminar specificity of functional MRI onset times during somatosensory stimulation in rat: Proc Natl Acad Sci U S A, v. 99, p. 15182-7.

Silva, A. C., J. H. Lee, I. Aoki, and A. P. Koretsky, 2004, Manganese-enhanced magnetic resonance imaging (MEMRI): methodological and practical considerations: NMR Biomed, v. 17, p. 532-43.

Silva, A. C., S. P. Lee, G. Yang, C. Iadecola, and S. G. Kim, 1999, Simultaneous blood oxygenation level-dependent and cerebral blood flow functional magnetic resonance imaging during forepaw stimulation in the rat: J Cereb Blood Flow Metab, v. 19, p. 871-9.

Singh, M., S. Kim, and T. S. Kim, 2003, Correlation between BOLD-fMRI and EEG signal changes in response to visual stimulus frequency in humans: Magn Reson Med, v. 49, p. 108-14.

Sipe, J. C., P. Lee, and E. Beutler, 2002, Brain iron metabolism and neurodegenerative disorders: Dev Neurosci, v. 24, p. 188-96.

Smith, A. J., H. Blumenfeld, K. L. Behar, D. L. Rothman, R. G. Shulman, and F. Hyder, 2002, Cerebral energetics and spiking frequency: the neurophysiological basis of fMRI: Proc Natl Acad Sci U S A, v. 99, p. 10765-70.

Smith, A. T., K. D. Singh, and M. W. Greenlee, 2000, Attentional suppression of activity in the human visual cortex: Neuroreport, v. 11, p. 271-7.

Sripati, A. P., T. Yoshioka, P. Denchev, S. S. Hsiao, and K. O. Johnson, 2006, Spatiotemporal receptive fields of peripheral afferents and cortical area 3b and 1 neurons in the primate somatosensory system: J Neurosci, v. 26, p. 2101-14.

Stippich, C., P. Freitag, J. Kassubek, P. Soros, K. Kamada, H. Kober, K. Scheffler, R. Hopfengartner, D. Bilecen, E. W. Radu, and J. B. Vieth, 1998, Motor,

somatosensory and auditory cortex localization by fMRI and MEG: Neuroreport, v. 9, p. 1953-7.

Suh, M., S. Bahar, A. D. Mehta, and T. H. Schwartz, 2006, Blood volume and hemoglobin oxygenation response following electrical stimulation of human cortex: Neuroimage, v. 31, p. 66-75.

Sur, M., 1980, Receptive fields of neurons in areas 3b and 1 of somatosensory cortex in monkeys: Brain Res, v. 198, p. 465-71.

Sur, M., P. E. Garraghty, and C. J. Bruce, 1985, Somatosensory cortex in macaque monkeys: laminar differences in receptive field size in areas 3b and 1: Brain Res, v. 342, p. 391-5.

Sur, M., M. M. Merzenich, and J. H. Kaas, 1980, Magnification, receptive-field area, and "hypercolumn" size in areas 3b and 1 of somatosensory cortex in owl monkeys: J Neurophysiol, v. 44, p. 295-311.

Sur, M., R. J. Nelson, and J. H. Kaas, 1982, Representations of the body surface in cortical areas 3b and 1 of squirrel monkeys: comparisons with other primates: J Comp Neurol, v. 211, p. 177-92.

Tang, L., M. J. Avison, and C. J. Gore, 2006, Non-Linear BOLD Responses for Transient Deactivations in V1: Proceedings of the 2006 Scientific Sessions of ISMRM (14th).

Thomas, C. G., and R. S. Menon, 1998, Amplitude response and stimulus presentation frequency response of human primary visual cortex using BOLD EPI at 4 T: Magn Reson Med, v. 40, p. 203-9.

Thompson, J. K., M. R. Peterson, and R. D. Freeman, 2003, Single-neuron activity and tissue oxygenation in the cerebral cortex: Science, v. 299, p. 1070-2.

Thulborn, K. R., J. C. Waterton, P. M. Matthews, and G. K. Radda, 1982, Oxygenation dependence of the transverse relaxation time of water protons in whole blood at high field: Biochim Biophys Acta, v. 714, p. 265-70.

Toth, L. J., S. C. Rao, D. S. Kim, D. Somers, and M. Sur, 1996, Subthreshold facilitation and suppression in primary visual cortex revealed by intrinsic signal imaging: Proc Natl Acad Sci U S A, v. 93, p. 9869-74.

Ts'o, D. Y., R. D. Frostig, E. E. Lieke, and A. Grinvald, 1990, Functional organization of primate visual cortex revealed by high resolution optical imaging: Science, v. 249, p. 417-20.

Tsao, D. Y., W. A. Freiwald, R. B. Tootell, and M. S. Livingstone, 2006, A cortical region consisting entirely of face-selective cells: Science, v. 311, p. 670-4.

Van Camp, N., M. Verhoye, and A. Van der Linden, 2006, Stimulation of the rat somatosensory cortex at different frequencies and pulse widths: NMR Biomed, v. 19, p. 10-7.

Van der Linden, A., M. Verhoye, V. Van Meir, I. Tindemans, M. Eens, P. Absil, and J. Balthazart, 2002, In vivo manganese-enhanced magnetic resonance imaging reveals connections and functional properties of the songbird vocal control system: Neuroscience, v. 112, p. 467-74.

Vanduffel, W., D. Fize, J. B. Mandeville, K. Nelissen, P. Van Hecke, B. R. Rosen, R. B. Tootell, and G. A. Orban, 2001, Visual motion processing investigated using contrast agent-enhanced fMRI in awake behaving monkeys: Neuron, v. 32, p. 565-77.

Vanduffel, W., D. Fize, H. Peuskens, K. Denys, S. Sunaert, J. T. Todd, and G. A. Orban, 2002, Extracting 3D from motion: differences in human and monkey intraparietal cortex: Science, v. 298, p. 413-5.

Vanzetta, I., H. Slovin, D. B. Omer, and A. Grinvald, 2004, Columnar resolution of blood volume and oximetry functional maps in the behaving monkey; implications for FMRI: Neuron, v. 42, p. 843-54.

Vazquez, A. L., and D. C. Noll, 1998, Nonlinear aspects of the BOLD response in functional MRI: Neuroimage, v. 7, p. 108-18.

Wandell, B. A., 1999, Computational neuroimaging of human visual cortex: Annu Rev Neurosci, v. 22, p. 145-73.

Watanabe, T., J. Frahm, and T. Michaelis, 2004, Functional mapping of neural pathways in rodent brain in vivo using manganese-enhanced three-dimensional magnetic resonance imaging: NMR Biomed, v. 17, p. 554-68.

Watanabe, T., T. Michaelis, and J. Frahm, 2001, Mapping of retinal projections in the living rat using high-resolution 3D gradient-echo MRI with Mn2+-induced contrast: Magn Reson Med, v. 46, p. 424-9.

Watanabe, T., O. Natt, S. Boretius, J. Frahm, and T. Michaelis, 2002, In vivo 3D MRI staining of mouse brain after subcutaneous application of MnCl2: Magn Reson Med, v. 48, p. 852-9.

Weber, R., P. Ramos-Cabrer, D. Wiedermann, N. van Camp, and M. Hoehn, 2006, A fully noninvasive and robust experimental protocol for longitudinal fMRI studies in the rat: Neuroimage, v. 29, p. 1303-10.

Wendland, M. F., M. Saeed, G. Lund, and C. B. Higgins, 1999, Contrast-enhanced MRI for quantification of myocardial viability: J Magn Reson Imaging, v. 10, p. 694-702.

Woolsey, C. N., and D. Fairman, 1946, Contralateral, ipsilateral and bilateral representation of cutaneous receptors in somatic areas I and II of the cerebral cortex of pig, sheep and other mammals.: Surgery, v. 19, p. 684-702.

Wu, G., F. Luo, Z. Li, X. Zhao, and S. J. Li, 2002, Transient relationships among BOLD, CBV, and CBF changes in rat brain as detected by functional MRI: Magn Reson Med, v. 48, p. 987-93.

Yacoub, E., and X. Hu, 2001, Detection of the early decrease in fMRI signal in the motor area: Magn Reson Med, v. 45, p. 184-90.

Yacoub, E., P. F. Van De Moortele, A. Shmuel, and K. Ugurbil, 2005, Signal and noise characteristics of Hahn SE and GE BOLD fMRI at 7 T in humans: Neuroimage, v. 24, p. 738-50.

Yang, X., F. Hyder, and R. G. Shulman, 1997, Functional MRI BOLD signal coincides with electrical activity in the rat whisker barrels: Magn Reson Med, v. 38, p. 874-7.

Zhang, N., J. C. Gore, L. M. Chen, and M. J. Avison, 2007, Dependence of BOLD signal change on tactile stimulus intensity in SI of primates: Magn Reson Imaging, v. 25, p. 784-94.

Zhao, F., P. Wang, K. Hendrich, and S. G. Kim, 2005, Spatial specificity of cerebral blood volume-weighted fMRI responses at columnar resolution: Neuroimage, v. 27, p. 416-24.

Zheng, W., Q. Zhao, V. Slavkovich, M. Aschner, and J. H. Graziano, 1999, Alteration of iron homeostasis following chronic exposure to manganese in rats: Brain Res, v. 833, p. 125-32.

Zhu, X. H., S. G. Kim, P. Andersen, S. Ogawa, K. Ugurbil, and W. Chen, 1998, Simultaneous oxygenation and perfusion imaging study of functional activity in primary visual cortex at different visual stimulation frequency: quantitative correlation between BOLD and CBF changes: Magn Reson Med, v. 40, p. 703-11.